ALMA MATER STUDIORUM - UNIVERSITÀ DI BOLOGNA

DOTTORATO DI RICERCA IN FISICA

Ciclo XXV
Settore Concorsuale: 02/B1
SSD: FIS/03

PROGRESS IN X-RAY SPECTROSCOPIES FOR THE STUDY OF ADVANCED MATERIALS

Presentata da:
LUCIA AMIDANI

Relatore:
Prof. FEDERICO BOSCHERINI

Coordinatore di Dottorato:
Prof. FABIO ORTOLANI

Esame finale anno 2013

Contents

Introduction

This thesis work is focused on the use of selected core-level x-ray spectroscopies to study semiconductor materials of great technological interest and on the development of a new implementation of appearance potential spectroscopy. The materials studied are very promising for applications in the photovoltaic, the opto-electronic and the telecommunication industries because of the properties shown by their electronic structure. A large part of the research aimed to their optimization, thus, investigates how these properties are affected by modifications at the atomic scale.

Core-level spectroscopies can be exploited to study these materials with a *local* approach since they are sensitive to the electronic structure localized on a chemical species present in the sample examined. This approach, in fact, provides important micro-structural information that is difficult to obtain with techniques sensitive to the average properties of materials.

In this thesis work we present a novel approach to the study of semiconductors with core-level spectroscopies based on an original analysis procedure that leads to an insightful understanding of the correlation between the local micro-structure and the spectral features observed. In particular, we studied the micro-structure of Hydrogen induced defects in nitride semiconductors, since the analysed materials show substantial variations of optical and electronic properties as a consequence of H incorporation.

Finally, we present a novel implementation of soft x-ray appearance potential spectroscopy, a core-level spectroscopy that uses electrons as a source of excitation and has the great advantage of being an in-house technique. The original set-up illustrated was designed to reach a high signal-to-noise ratio for the acquisition of good quality spectra that can then be analysed in the framework of the real space full multiple scattering theory. This technique has never been coupled with this

analysis approach and therefore our work unite a novel implementation with an original data analysis method, enlarging the field of application of this technique.

The present thesis is structured as follows:

In the first chapter the main core-level spectroscopies used throughout this thesis are introduced. There is no claim for completeness, but the aim is to highlight the link between experimental spectra and structural properties of the material under examination.

The second chapter introduces the two classes of materials investigated, the concentrated nitride and the dilute nitride semiconductors. In the chapter, the principal growth methods used are presented together with the difficulties met in obtaining high quality materials. Then an overview of the main properties which render these materials so interesting from the technological point of view is given.

In the third chapter we present a study of GaInN alloy and of the defects induced by the H incorporation in the material. This alloy plays a fundamental role in the future of photovoltaic and opto-electronics and even if it is already in use in many commercially available devices, it is still object of fundamental research since its technology is not yet mature. It has been experimentally proved that H incorporation induces strong modifications in the band structure and in the carrier concentration.

By means of a systematic study based on x-ray absorption techniques on a series of samples with different In content, we studied the effects of H incorporation on the local electronic structure of N and In atoms. Interesting results on the cation sublattice ordering and on the structure of the H-defect have been obtained thanks to a novel analysis method that allows an unprecedented insight into the origin of spectral features.

In the fourth chapter the electronic structure localised on N in dilute GaAsN is studied. In this material the incorporation of a small percentage of N atoms in GaAs induces a strong and unexpected reduction of the band gap; in addition, the electronic properties of GaAs can be fully restored by irradiating the dilute nitride with a low-energy H beam. The interaction of N atoms with the electronic structure of GaAs and H atoms is the cause for the observed effects and

we present for the first time a study of both the occupied and unoccupied density of states localized on N impurities before and after H-irradiation. We did this by combining x-ray emission and absorption spectroscopy at the N K-edge. Our work illustrates therefore a preferential perspective to follow the evolution of the local electronic structure in dilute nitrides.

The fifth chapter, finally, presents a new implementation of soft x-ray appearance potential spectroscopy (SXAPS), a core-level spectroscopy that uses accelerated electrons as a probe. This technique can nowadays count on new and powerful means for the data analysis, like the *ab initio* codes used in the analysis of absorption and emission data in previous chapters. These tools, combined with a new set-up providing spectra with a high signal-to-noise ratio, open the way to a novel use of this technique, that is not expensive, easy to implement and has the local sensitivity and chemical selectivity common to all core-level spectroscopies.

The results obtained in this thesis have been published in:

1 L. Amidani, L. Pasquini and F. Boscherini; Appearance potential spectroscopy with a photon counting detector and multiple scattering spectral interpretation; Review of Scientific Instruments **83**, 083901 (2012).

2 L. Amidani, F. Filippone, A. Amore Bonapasta, G. Ciatto, V. Lebedev, A. Knübel and F. Boscherini; X-ray absorption spectra of $In_xGa_{1-x}N$ alloys with insight from atom-specific simulations; Physical Review B **86**, 155211 (2012).

3 M. De Luca, G. Pettinari, G. Ciatto, L. Amidani, F. Filippone, A. Polimeni, E. Fonda, F. Boscherini, A. Amore Bonapasta, D. Giubertoni, A. Knübel, V. Lebedev and M. Capizzi; Identification of four-hydrogen complexes in In-rich $In_xGa_{1-x}N$ ($x>0.4$) alloys using photoluminescence and X-ray absorption spectroscopies and density functional theory; Physical Review B **86**, R201202 (2012).

4 L. Amidani, A. Polimeni, M. Capizzi, F. Filippone, A. Amore Bonapasta, G. Ciatto, V. Lebedev, A. Knübel and F. Boscherini; The evolution of the electronic structure localized on Nitrogen in dilute nitrides upon H irradiation; submitted to Phys. Rev. B.

Chapter 1

Core-level spectroscopies

One of the most active areas of condensed matter physics is the investigation of how macroscopic properties of a system stems from its characteristics at the atomic level. Two big issues in this field are the atomic structure and the electronic structure atoms give rise to, once bound together. Core-level spectroscopies address this microscopic level of matter. The process at the base of all core-level spectroscopies is the same: an atomic species contained in the sample is selectively excited by ionization of core-electrons and the intensity of a product of the interaction is recorded. The electron binding energies of core-levels cover a large portion of the x-ray region, from some hundreds of eV to tens of KeV; thus excitation sources used in core-level spectroscopies are x-ray beams or accelerated electrons with kinetic energy in the x-ray range. At these energies the probe interacts mainly with the atomic electron densities, while the interaction with the nuclei is negligible, therefore core-level spectroscopies probe the electronic and structural properties of a system. The physical information carried by a certain technique depends on the interaction process that creates the detected particles, good theoretical models for the cross section are thus of fundamental importance to disclose the potentialities as well as the drawbacks of a technique.

Core-level spectroscopies share the peculiarity of being sensitive to the local environment of the specific chemical element excited, in other words they are chemical selective and local sensitive. The first property holds because the electron binding energies are element specific and tuning the incident energy to the selected ionization threshold automatically excludes other atomic species from the main process. On the other hand, the sensitivity to the local environment is connected to the high degree of localization of the core-level wave-function, which has a large superposition integral only with wave-functions highly localized on the

absorber, and to its lifetime, that limits the interaction in the time domain and consequently the volume probed.

In this thesis three different core-level techniques will be used to investigate semiconductors: x-ray absorption spectroscopy (XAS), x-ray emission spectroscopy (XES) and soft x-ray appearance potential spectroscopy (SXAPS). XAS and XES both use x-ray photons to promote core-electrons to the empty density of states (DOS), but while the first detects the amount of photons absorbed by the sample as the incident energy is tuned around an absorption threshold, the second collects and analyzes the photons emitted by the sample during the filling of the core-holes. Both these techniques were largely promoted by the advent of synchrotron radiation (SR) laboratories, able to provide an x-ray beam of over 4 orders of magnitude more intense that the x-ray sources available at the time. When performed at SR laboratories, these techniques can also take advantage of the high degree of linear polarization of synchrotron light, making them sensitive to the anisotropy of the structure around the absorbing atom. In the last fifty years, both the field of applicability of these techniques as well as the ability of extracting information from the data have been highly developed, thanks to improvements of SR instrumentation, computer calculation capabilities and analysis techniques.

SXAPS, unlike XAS and XES, uses an accelerated electron beam, whose kinetic energy is varied around an ionization threshold, to excite core-electrons into unoccupied states. The principle is the same as in XAS, but the use of electrons as the excitation source makes the physical process more complicated. Two electrons are in fact involved both in the initial and final state. In addition, electrons interact strongly with matter, causing sample damage and a variety of products that covers the signal of interest with a large unwanted background. On the other hand, an electron beam is easily produced and controlled, since electrons are produced by a hot cathode and deflected by electromagnetic fields, while high brilliance, tunable and collimated x-ray beams are far more expensive and complicated to obtain and control.

In the following, a detailed introduction to each of these techniques will be given, together with a treatment of the cross section for XAS in the framework of Real Space Multiple Scattering (RSMS) theory, since most of the computational codes used for *ab initio* simulations of XAS are based on this approach.

1.1 X-ray absorption spectroscopy

X-ray absorption spectroscopy measures the absorption coefficient of the investigated sample as a function of incident photons energy. The beam energy is varied around an ionization threshold of an atomic species contained in the sample, so that the experimental spectrum has a characteristic shape given by a smooth background dominated by a sudden increase in correspondence to the selected ionization energy. The sudden increase, called the absorption edge, is due to the opening of a new interaction channel, the absorption of incident x-rays by core-electrons of the selected species. What raised the interest of scientists in XAS measurements was the behaviour of the absorption coefficient immediately after the edge: while in gas phase samples it decreases slowly without presenting other features apart from the edge itself, in condensed matter it shows characteristic oscillations, named x-ray absorption fine structure (XAFS). In Figure 1.1 XAS spectra on vapour and solid phase of Cd are reported as an example. The spectrum from the vapour phase is smooth and structureless, while that from the Cd foil presents the characteristic XAFS modulations. The absence of the fine structure in measurements acquired on gas phase samples, where atoms are isolated, indicates that these modulations are a signature of the atomic structure of the sample and thus can be exploited to extract structural information.

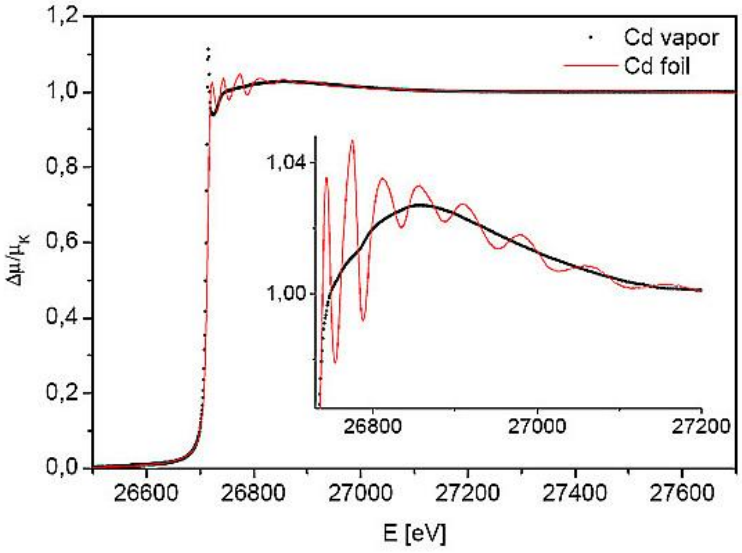

Figure 1.1. XAS spectra on Cd in vapour phase (black dots) and in solid phase (red continuous line) from Ref. 1. Fine structure modulations are absent in the vapour phase, indicating they are a signature of the atomic structure.

The origin of these oscillations was debated for long time until in the '70s the situation was clarified by Stern, Sayers and Lytle[2] who developed a consistent theoretical framework for the interpretation of the XAFS signal and demonstrated its ability of providing structural information. According to their theory, the oscillations are due to an interference effect, as is illustrated in the scheme of Figure 1.2: once excited, the photo-electron propagates throughout the solid as a spherical outgoing wave (the blue wave in Figure 1.2) the energy of which equals the difference between the absorbed photon energy and the binding energy of the excited core-electron. This excess energy determines the wavelength of the propagating photo-electron, so that increasing the incident beam energy corresponds to lowering the photo-electron wavelength. In the isolated atom case, the photo-electron would propagate as a spherical wave without any interference effect, but when it propagates in a solid or a molecule, each time the wave front encounters the surrounding atoms, a scattering event takes place and the original outgoing wave interferes with all the backscattered waves (the red wave in Figure 1.2) at the absorber site. The oscillations observed above the edge are therefore the modulations of the photo-electron wave-function caused by the interference of the primary wave with the scattered waves as a function of photo-electron energy.

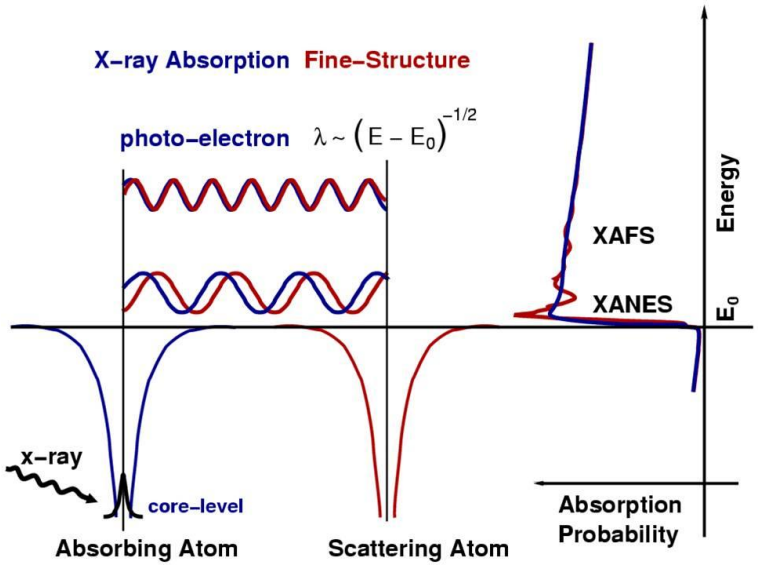

Figure 1.2. Scheme of the physical process behind the fine structure modulations: the photo-electron scatters from the neighbouring atoms and returns to the absorbing atoms modulating the amplitude of the photo-electron wave-function at the absorbing atom. this in turns modulate the absorption coefficient, causing the fine structure oscillations.

The work of Stern, Sayers and Lytle, based on some key approximations, provided an analytical formula where all the single scattering contributions were summed up, showing how the oscillatory behaviour was linked to structural parameters such as the bond distances and the coordination numbers. The approximations behind this formula are not appropriate for the near edge part of the spectrum, where the photo-electron energy is low, so that the XAS spectrum is commonly thought as split into two regions: the x-ray absorption near edge structure (XANES) and the extended x-ray absorption fine structure (EXAFS), that starts approximately 50 eV from the edge and is well described by the formula developed by Sayers et al.

The development of the XAS technique was greatly promoted by the work of Sayers, Stern and Lytle, both on the experimental and theoretical side and with the advent of SR laboratories it became an important technique to investigate structural and electronic properties of matter. EXAFS in particular became greatly successful as a means to unravel the structure of materials and extracting from EXAFS data accurate structural parameters is today a relatively standard procedure. Unfortunately the XANES region is far more complicated to analyze, since the contributions by all orders of scattering are relevant. Therefore only a qualitative information is easily extracted, even if its sensitivity to the details of the electronic structure makes this part of the spectrum rich of information. A great effort has been spent lately to strengthen the analysis of XANES spectra and particularly crucial has been the progress in *ab initio* codes and computer calculation power, that now provide a way of taking into account all the scattering contributions within a large volume around the absorber. Improvements to avoid the most restrictive approximations are proposed. All these progresses are making the information hidden in XANES accessible and quantitative.

1.1.1 XAS detection schemes

From the experimental point of view, performing a XAS measurement requires first of all a high intensity and tuneable x-ray beam. This is why this technique is strictly linked to synchrotron radiation facilities. The typical experimental set-up, sketched in Figure 1.3, is essentially made of an x-ray beam, usually provided by a SR insertion device, a focalizing and mono-chromatizing stage where the beam is reduced in size and tuned to the desired energy and finally

a detection system where the absorbed intensity is measured directly or through a product of the absorption process.

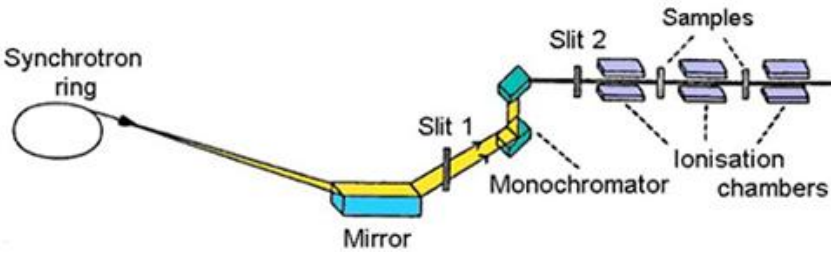

Figure 1.3. Scheme of a typical XAS experimental set-up. X-rays produced by a SR are focalized by mirrors, collimated by slits and reduced to a single energy beam by a monochromator. The detection scheme sketched is the typical set-up of the transmission mode.

Among the various detection schemes available, the most common is the transmission mode. Here the beam hits a thin and homogeneous sample and the intensity of the beam is measured upstream and downstream. The absorption coefficient, following the Lamber-Beer law, can be obtained by the logarithm of the ratio between the incident and the transmitted beam intensity

$$\mu d = \ln \frac{I_0}{I} \tag{1.1}$$

where d is the thickness of the sample. This detection scheme measures the total cross section, that includes also the elastic and inelastic scattering, but since these second order phenomena are 2 – 3 orders of magnitude less probable, it is commonly taken as a measure of the absorption cross section. To perform XAS measurements in the transmission mode, a very homogeneous sample is needed and, depending on the energy involved and the material investigated, it has to be thin enough to guarantee a normalized edge jump of about 1. These requirements can't be fulfilled in the soft x-ray regime, where photons have a very short mean free path and are heavily absorbed also by air.

In these cases the direct measurement of the absorbed intensity is not feasible, so the amount of core-holes created by the absorption process is measured in some way, since it is proportional to the absorption coefficient. The way to do that is to detect a product of the decay of the core-hole. Two main decay channels are available as shown in Figure 1.4: the fluorescence decay and the Auger decay. In both of them the core-hole is filled by an upper-level electron, but in the fluorescence decay the electron releases its excess energy by emitting an x-ray

photon, while in the Auger decay it gives the excess energy to another electron that is then ejected.

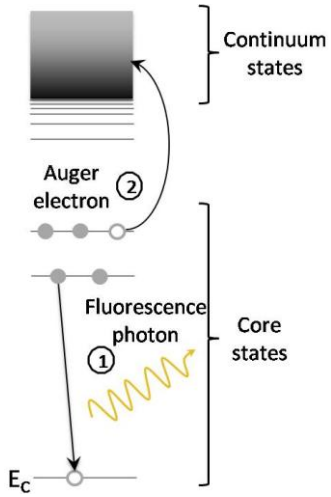

Figure 1.4. Sketch of core-hole decay channels. An upper-level electron fills the core-hole and loses the excess energy with the emission of a characteristic fluorescence photon (1) or ejection of an Auger electron (2).

The Fluorescence Yield (FLY) detection mode counts the characteristic photons emitted and the Total Electron Yield (TEY) counts the Auger electrons relative to a certain decay path escaping the surface. Since electrons interact more strongly with matter than x-ray photons, only electrons from a thin surface layer can escape the sample and be detected, while x-rays escape depth is larger. As a consequence, TEY measurements are surface sensitivity while FLY probe the bulk of the sample.

Experimental XAS measurements discussed in this thesis were all obtained in the FLY mode implemented with a pulse-counting detector; we will, therefore, introduce this specific detection scheme together with the problems connected with its use.

1.1.2 FLY detection mode[3]

In the Fluorescence Yield (FLY) mode one measures the intensity of the incident beam, I_0, and the fluorescence x-rays I_f emitted by the sample. A sketch of the typical set-up is drawn in Figure 1.5. The detector used to measure the emitted fluorescence is usually placed at 90° degrees from the incident beam direction because at this angle the elastic scattering of incident photons is minimized.

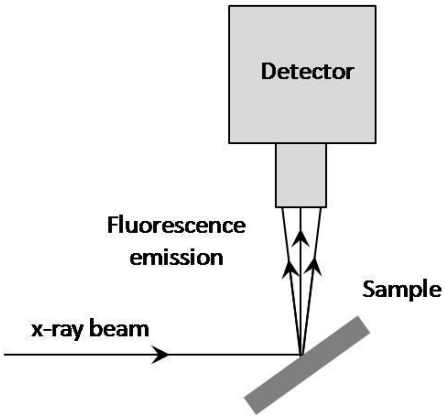

Figure 1.5. Scheme of the typical FLY set-up. The detector is placed at 90° from the incident beam direction.

Detectors used to record the fluorescence intensity can be current mode detectors, which give a current signal proportional to the total emitted photons, or pulse-counting detectors, that produce a pulse proportional to the detected photon energy for each photon impinging on the detector active area. Pulse-counting detectors have large conversion efficiency and a certain degree of energy resolution that can be exploited to select the fluorescence line relative to a specific decay transition. The most commonly used pulse-counting detectors are solid state detectors like Si and Ge photodiodes, the resolution of which is around 130 eV.

The FLY detection mode is a straightforward way of measuring XAS spectra only if the intensity of emitted fluorescence photons is linearly proportional to the absorption coefficient of the species investigated. When the FLY detection scheme with a pulse-counting detector is used, however, self-absorption effects and a non-linear response of the detector can break the linearity and induce unwanted distortions in the recorded spectra.

The self-absorption effect is negligible unless the sample is thick and concentrated; if these conditions are met in a XAS experiment, data correction may be needed before starting the analysis. The self-absorption effect in thick samples is summarized by the formula

$$\frac{I_f}{I_0} = \frac{\epsilon d\Omega}{4\pi}\left(\frac{\mu_i(E)}{\mu_T(E) + \mu_T(E_f)\tan\alpha}\right) = \frac{\epsilon\Delta\Omega}{4\pi}\mu_i(E)g(E) \qquad (1.2)$$

where the ratio of the fluorescence intensity I_f to the incident beam intensity I_0 is given by the product of the fluorescence yield coefficient ε, the solid angle covered

by the detector $\Delta\Omega/4\pi$, the absorption coefficient of the excited species $\mu_i(E)$ and an energy dependent coefficient $g(E)$ that is in turn proportional to $\mu_i(E)$. It is the dependence of $g(E)$ on $\mu_i(E)$ that brings about the non-linear proportionality between FLY and $\mu_i(E)$. A detailed derivation of this formula is given in Appendix 1 at the end of this chapter; however, the cause of the effect can be understood without many calculations and following the scheme depicted in Figure 1.6: the incident beam impinges the sample at an angle α, while the detector is placed along the direction indicated by the escaping arrow, which in turn forms an angle β with the sample surface. Incoming photons penetrate the sample and, when absorbed, cause the emission of fluorescence photons, that in order to be detected have to travel towards the detector and escape the surface of the sample. Since the attenuation of the incident photon flux inside the sample depends on the total absorption coefficient $\mu_T(E)$, the number of x-ray photons reaching a certain depth as well as the volume probed by the beam is a function of the incident energy. The dependence of the volume probed on the incident energy has to be negligible in order to have linear proportionality between the FLY and the absorption coefficient, so that the number of atoms involved in the excitation is almost a constant and the modulations of the FLY can be ascribed only to the absorption coefficient.

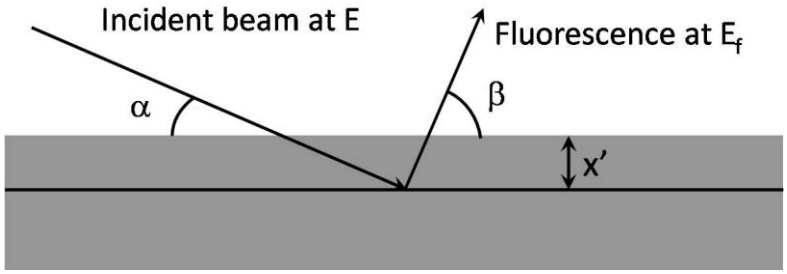

Figure 1.6. Scheme of the mutual orientation of incident beam, sample surface and escaping fluorescence photons for the calculation of self-absorption effects. The incident beam forms an angle α with the sample surface and penetrates till a depth x'. Here fluorescence photons are emitted and escape the sample surface at an angle β before being detected.

Many factors contribute to the relevance of the self-absorption effect. First of all the thickness of the sample: if the sample is thin, the attenuation of the incident beam with depth is negligible and linearity holds. On the contrary, if the sample is thick, the attenuation of the incident beam is remarkable and the dependence of the volume probed on the incident energy can affect seriously experimental data. The question then is how is the shape of the total absorption coefficient in the range on energy scanned. If it is almost flat, self-absorption is

negligible, on the contrary if it varies a lot, distortions of the spectral line shape are relevant. The shape of the total absorption coefficient across an absorption edge depends on the concentration of the relative species: if the sample is dilute, the total absorption coefficient is dominated by the contribution of the other constituents and it is almost flat since far from edges it has a smooth energy dependence. On the other hand, if the sample is concentrated, the energy dependence of the total absorption coefficient can't be neglected and the volume probed varies remarkably with the incident beam energy. Even in this latter case, when the sample is concentrated and thick, there is still a chance to minimize self-absorption distortions with an accurate choice of the set-up geometry. From equation (1.2) the dependence of $g(E)$ on $\mu_T(E)$ can be minimized playing on the incidence angle α; with $\alpha \cong 90°$ the leading term in the denominator is $\mu_i(E_f)$ and the dependence on $\mu_i(E)$ is then negligible. According to the line of reasoning based on the variable volume probed, at normal incidence only fluorescence photons emitted at the sample surface can reach the detector before being re-absorbed, therefore the variation in the penetration depth has minimal influence on the FLY and the self-absorption effect doesn't affect much the spectrum. At grazing incidence, instead, photons emitted deeply in the sample have to cross a short path to escape and are thus detected, making spectra acquired at grazing incidence seriously distorted by self-absorption. In this latter case it is necessary to correct spectra if a quantitative analysis has to be carried out.

This last argument partially contradicts our previous statement that the FLY detection is bulk sensitive. Actually, the geometry of the experiment can give surface sensitivity to FLY recorded XAS spectra. From the work by Troger et al.[4], the information depth of FLY recorded spectra, named λ_f, is given by the equation

$$\lambda_f = \frac{\sin\alpha}{\mu_T(E) + \mu_T(E_f)\frac{\sin\alpha}{\sin\beta}} \tag{1.3}$$

where α and β are the incoming and escaping angles as indicated in the scheme of Figure 1.6. λ_f is defined as the expectation value of the distance perpendicular to the sample surface at which the fluorescence photons detected were generated, therefore 68% of the fluorescence photons detected were generated in the surface layer of thickness λ_f. The derivation of this formula can be found in Appendix 1.

Together with self-absorption effect, also the use of a pulse-counting detector can introduce a non-linear dependence of FLY from the absorption coefficient of the selected species. This happens when the number of fluorescence photons detected, m, is less than the number of fluorescence photons impinging on the detector, n, and it is caused by the amplifier dead-time that is the time the amplifier needs to integrate the charge pulses coming from the detector. The electronic processing the signal from a solid state detector can't resolve two events separated by a time-delay less than the amplifier dead-time. If the relation between the real events n and the detected events m is known, spectra can be corrected for dead-time effects. Details on dead-time effects relative to the use of solid state detectors are given in Appendix 1.

1.1.3 XAS cross section

So far we discussed the experimental implementation of XAS, now we go into the details of the theoretical framework on which it is grounded in order to understand which information this technique can provide. The absorption process involves the transition of an atomic core-electron into an empty state caused by the interaction of the electromagnetic field with matter. The problem is thus in the domain of the time-dependent perturbation theory; the Hamiltonian of the system is written as the unperturbed term plus the interaction term

$$H = H_0 + H_{int}. \tag{1.4}$$

The interaction Hamiltonian is obtained substituting $\vec{p} \rightarrow \vec{p} + e\vec{A}$ in the unperturbed Hamiltonian of the system. The result is

$$H = \frac{\vec{p}^{\,2}}{2m} + \frac{e}{m}\vec{A}(\vec{r},t)\cdot\vec{p} + \frac{e^2}{2m}\vec{A}^{\,2}(\vec{r},t) - \frac{Ze^2}{4\pi\varepsilon_0 r} = H_0 + H_{int} \tag{1.5}$$

and isolating the interaction terms we have

$$H_{int} = \frac{e}{m}\vec{A}(\vec{r},t)\cdot\vec{p} + \frac{e^2}{2m}\vec{A}^{\,2}(\vec{r},t) \tag{1.6}$$

where the Coulomb gauge has been used to replace $\vec{p}\cdot\vec{A}$ with $\vec{A}\cdot\vec{p}$ and $\vec{A}(\vec{r},t)$ is the vector potential of the electromagnetic field. The interaction Hamiltonian is made by two terms, one linear and one quadratic in the vector potential $\vec{A}(\vec{r},t)$.

The absorption process is a one-photon process, since the initial state differs from the final state only for a single photon. One-photon processes are described by linear terms in the vector potential, while quadratic terms in the vector potential give rise to two-photons processes. This can be understood considering that the second quantization formalism expresses the vector potential as a sum of single-photon creation and annihilation operators. Linear terms in $\vec{A}(\vec{r},t)$ then describe events where the number of photons in the system is changed by one, while the action of a quadratic term on a quantum state acts on two photons of the system. To calculate the absorption cross section is thus sufficient to take the perturbation at the first order of the linear term in $\vec{A}(\vec{r},t)$. According to the time-dependent perturbation theory, the probability to have a transition from an initial state $|i\rangle$ to a final state $|f\rangle$ is given by the Fermi's golden rule, that for the absorption of a photon is given by:

$$\Gamma_{i,f} = \frac{2\pi}{\hbar}|\langle f|H_{int}(\vec{r})|i\rangle|^2\delta(E_f - E_i - \hbar\omega) \tag{1.7}$$

where ω is the frequency of the harmonic perturbation.

$H_{int}(\vec{r})$ is the time-independent part of the perturbation causing the absorption, therefore we need the expression of the linear term in the vector potential to proceed. The vector potential associated to an electromagnetic wave is written classically as

$$\vec{A}(\vec{r},t) = \vec{A}_0(\omega)\hat{\varepsilon}\left[e^{i(\omega t-\vec{k}\cdot\vec{r})} + e^{-i(\omega t-\vec{k}\cdot\vec{r})}\right] = \vec{A}_0(\omega)\hat{\varepsilon}\cos\left(\omega t - \vec{k}\cdot\vec{r}\right) \tag{1.8}$$

Substituting the time-independent part in the Fermi's golden rule we obtain

$$\Gamma_{i,f} = \frac{2\pi}{\hbar}\frac{e^2}{m^2}A_0^2(\omega)\left|\left\langle f\left|e^{-i\vec{k}\cdot\vec{r}}\hat{\varepsilon}\cdot\vec{p}_i\right|i\right\rangle\right|^2\delta(E_f - E_c - \hbar\omega). \tag{1.9}$$

Since in core-level excitations the extension in space of the wave-function of the core-electron is much smaller than the wavelength of the incoming radiation, the spatial variation of the electromagnetic field is irrelevant on the length scale of the core-state and therefore the exponential can be set equal to 1. This is called the dipole approximation and its validity in the case of x-rays and inner electrons can

be verified rapidly: the radius of inner atomic orbitals is almost $\frac{a_0}{Z} \approx \frac{0.53}{Z}$ Å and the x-ray wavelength is around 1 Å, therefore $\vec{k} \cdot \vec{r} \ll 1$.

The Heisenberg equation of motion for the position operator $\vec{r}$ can be used to switch from $\vec{p}$ to $\vec{r}$

$$\frac{i\hbar}{m}\hat{p} = [\vec{r}, H_0] = \vec{r}H_0 - H_0\vec{r} \tag{1.10}$$

$$\langle f|\hat{\varepsilon} \cdot \vec{p}|i\rangle = \frac{m}{i\hbar}\langle f|\hat{\varepsilon} \cdot (\vec{r}H_0 - H_0\vec{r})|i\rangle = \frac{m}{i\hbar}\big(E_i - E_f\big)\langle f|\hat{\varepsilon} \cdot \vec{r}|i\rangle \tag{1.11}$$

where in the final result we used the property of the initial and final states to be stationary states of the unperturbed Hamiltonian.

Substituting the matrix element into the transition probability and dividing for the incident photon flux, the cross section for the absorption process is obtained

$$\sigma = 4\pi^2\hbar\omega\alpha|\langle f|\hat{\varepsilon} \cdot \vec{r}|i\rangle|^2\delta\big(E_f - E_i - \hbar\omega\big). \tag{1.12}$$

This equation was derived starting from a single, localized final state. When many degenerate states are available, like for final state lying in the continuum, the sum over all final states must be performed and as a consequence the cross section is proportional to the density of unoccupied states.

XAS is therefore proportional to the empty density of states of a material, but because of the matrix element, the initial and final states wave-functions have to fulfil some selection rules to prevent the matrix element from being zero. These rules are easily derived by approximating the initial state with an atomic-like state of well-defined angular momentum (l, m). This is appropriate as we are dealing with a core-state wave-function. The final state is more complicated since contributions from the surrounding atoms are relevant. Concerning its angular dependence, however, it can be expanded into a linear combination of spherical harmonics centred on the absorbing atom. Writing the scalar product between the polarization and the position operator in terms of spherical harmonics

$$\hat{\varepsilon} \cdot \vec{r} = \sqrt{\frac{4\pi}{3}}\left[\varepsilon_z Y_{1,0} - \frac{\varepsilon_x - i\varepsilon_y}{\sqrt{2}}Y_{1,1} + \frac{\varepsilon_x + i\varepsilon_y}{\sqrt{2}}Y_{1,-1}\right], \tag{1.13}$$

the angular part of the matrix element is given by a scalar product of three spherical harmonics:

$$\int d\Omega Y^*_{l_f,m_{l_f}} Y_{l,m_l} Y_{l_i,m_{l_i}}. \tag{1.14}$$

From integration on the azimuthal angle, the first selection rule is found:

$$\int_0^{2\pi} d\varphi e^{-im_{l_f}\varphi} e^{im_l\varphi} e^{-im_{l_i}\varphi} = 2\pi\delta_{m_{l_f}-m_l,0}. \tag{1.15}$$

The integral is not null only if the difference between the magnetic quantum numbers of the final and initial states is equal to the momentum carried by the photon. The selection rule for the magnetic quantum number is then

$\Delta m = 0$	*linear polarized light*
$\Delta m = +1$	*circularly polarized light (right)*
$\Delta m = -1$	*circularly polarized light (left)*

The angular momentum quantum number selection rule, instead, can be obtained considering the parity of spherical harmonics. These functions are even if l is even and odd if l is odd. Since the photon angular momentum is 1, its spherical harmonic is odd and to have a non-zero integral the product of the final and initial state spherical harmonics has to be odd too. This is always true if the difference of their angular momenta is odd. In addition, the overall angular momentum has to be conserved, therefore the final selection rule is

$$\Delta l = \pm 1.$$

This selection rule allows only final states of a certain symmetry to be reached by the photo-electron depending on that of the excited electron wave-function. For example, when an *s* electron is excited, only final states with *p*-symmetry can be reached, while if a *p* core-electron is removed, the transition is allowed both to *s*- and *d*-symmetry states.

The dipole matrix element, therefore, filters the allowed final states according to their angular momentum, making the XAS spectrum sensitive to the partial projected unoccupied density of states.

1.1.4 XAS angular dependence

It is well known that XAS spectra show angular dependence, that means the relative intensity of line shape features varies upon rotation of the sample with respect to the beam direction. This effect is caused by the variation in the relative orientations of the x-ray electric field and the crystal-symmetry axis of the sample measured. This dependence can be intuitively understood considering that final states electron charge densities depends on the symmetry of the structure and the strength of the matrix element depends on the direction of the electric field takes with respect to the electron charge densities. A full explanation of XAS angular dependence can be derived using tensor algebra and applying the expansion of spherical tensors to the XAS cross section. Details on this procedure can be found elsewhere[5]; we only report the form assumed by the absorption coefficient in the dichroism case, valid for many point groups and in particular for hexagonal structures, the crystalline form of samples investigated in Chapter 3. The equation is

$$\sigma^D(\hat{\varepsilon}) = \sigma^D(0,0) - \frac{1}{\sqrt{2}}(3\cos^2\theta - 1)\sigma^D(2,0), \tag{1.16}$$

where D stands for *dichroism* and θ is the angle between the electric field and the z-axis of the point-group orthonormal system. $\sigma^D(l,m)$ are the terms of the tensor expansion, with l and m indicate the quantum numbers of spherical harmonics involved. $\sigma^D(0,0)$ is the isotropic term while $\sigma^D(2,0)$ is the only non-zero term for samples with a rotation axis of order greater than two. The angular dependence of the cross section vanishes for $\cos\theta = \frac{1}{\sqrt{3}}$, which implies $\theta = 54{,}73°$, known as the magic-angle.

Apart from the special case of the magic-angle, the line shape of the spectrum depends on θ; the general form of $\sigma^D(2,0)$ can be obtained using the multiple scattering approach[5,6], but a molecular orbital point of view is more intuitive, therefore in the following we derive the angular dependence of K-edge spectra in the molecular orbital approach[7].

According to the $\Delta l = \pm 1$ selection rule, when a *1s* electron is excited, the final state has to be of *p*-symmetry around the absorbing atom and because of the localisation of the *1s* initial state, the atomic valence component of the excited atom dominates in the evaluation of the matrix element, under the assumption

that the final state wave-function is well approximated by a linear combination of atomic orbitals. The angular dependence is contained in the matrix element

$$|\langle f|\hat{\varepsilon}\cdot\vec{r}|i\rangle|^2 = |\hat{\varepsilon}\cdot\langle f|\vec{r}|i\rangle|^2. \tag{1.17}$$

Because of the spherical symmetry of the initial state and of the preponderance in the final state wave-function of *p*-symmetry states centred on the excited atom, the vector matrix element $\langle f|\vec{r}|i\rangle$ points in the same direction of the *p*-component of the final state orbital on the excited atom, thus the polarization dependence of the total matrix element can be expressed as a function of the angle δ between the polarization direction $\hat{\varepsilon}$ and the direction $\hat{O}$ of the largest amplitude of the final state orbital[7]

$$|\hat{\varepsilon}\cdot\langle f|\vec{r}|i\rangle|^2 \propto \left|\hat{\varepsilon}\cdot\hat{O}\right|^2 \propto \cos^2\delta. \tag{1.18}$$

Assuming $\hat{O}$ to be a vector (electron charge densities distributions of molecular orbitals can also be planar) and following the notation shown in Figure 1.7, where θ is the angle between the normal to the sample surface $\hat{n}$ and the electric field vector $\vec{E}$, α is the angle between $\hat{n}$ and $\hat{O}$, we can express δ as a function of θ, α and the azimuthal angle ϕ

$$\cos^2\delta = \cos^2\theta\cos^2\alpha + \frac{1}{2}\sin^2\theta\sin^2\alpha\cos^2\phi + 2\cos\theta\cos\alpha\sin\theta\sin\alpha\cos\phi. \tag{1.19}$$

The angle ϕ in a bulk sample can take any value and considering an hexagonal structure with the normal to the surface is parallel to the sixth-order rotational symmetry axis[8], we can integrate on the azimuthal angle and obtain, with some algebra

$$\cos^2\delta = \cos^2\theta\cos^2\alpha + \frac{1}{2}\sin^2\theta\sin^2\alpha = \frac{1}{3}\left[1 + \frac{1}{2}(3\cos^2\theta - 1)(3\cos^2\alpha - 1)\right]. \tag{1.20}$$

The θ-dependence in the final result obtained by the molecular orbital approach is identical to that in the more general equation (1.16). In addition, the dependence on the relative directions of the electric field $\vec{E}$ and the direction of the largest electron density $\hat{O}$ is expressed by the dependence on the angle α. With

an analogous derivation, the angular dependence for planar molecular orbitals can be carried out[7].

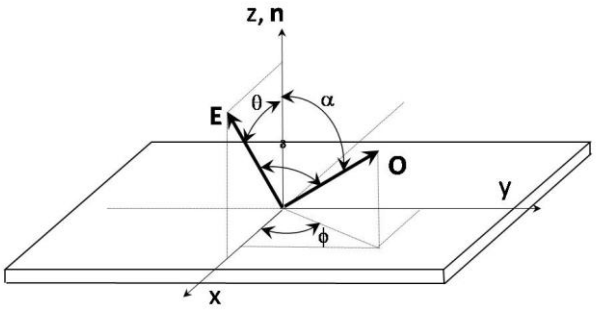

Figure 1.7. The incident beam lies on the xz-plane and the electric field E forms an angle θ with the z-axis. The vector O represents the electron density distribution of a specific molecular orbital state. Its orientation is determined by the angle α with the z-axis and the azimuthal angle ϕ. δ is the angle between the electric field E and the vector orbital O.

1.2 X-ray emission spectroscopy

X-ray emission spectroscopy (XES) is a core-level spectroscopy complementary to XAS; it is chemical selective and local sensitive, like XAS, but it probes the occupied density of states instead of the unoccupied DOS. In XES a core-level electron is excited in an empty state and the signal recorded is the energy dependence of the fluorescence emitted by the sample during the core-hole decay process. Unlike in XAS, during a scan the incident beam is held at fixed energy, at or above the ionization threshold, and the emitted photons intensity is recorded as a function of their energy. The energy of incident photons can then be changed to study the line shape dependence on the excitation energy.

To perform a XES experiment it is necessary an energy-dispersive x-ray detector with a suitable energy resolution. Depending on the energy range of the emitted photons, the dispersive element of the detector can be a grating (soft x-rays) or a system of crystals matching the Bragg law for the energies and geometry involved (hard x-rays). Once the photons have been dispersed or mono-chromatized, a position-sensitive detector or a device to convert photons into an electric signal are used to record the intensity of the emitted photons at different energies. XES measurements are performed also with electron beams and conventional x-ray sources, but since the physical phenomenon giving rise to the emission is a second-order process, its intensity is very low and a high brilliance source is the best option to record good quality spectra. This is why XES experimental stations are usually hosted on SR undulator beam lines. Their

number is growing in later years, not only for the sophisticated detector systems developed recently, but also for the richness of information about the electronic structure that this technique can provide.

XES is usually divided into two classes depending on the excitation induced: it is called resonant x-ray emission spectroscopy (RXES) when the incident photons are close to a core-electron threshold and normal x-ray emission spectroscopy (NXES) when the electron is excited in a continuum state far above the ionization threshold. In RXES the spectral line shape can strongly depend on the excitation energy while in NXES these effects are negligible. As a consequence, NXES has been interpreted for a long time as the product of an absorption followed by an emission process. Also if this picture, under certain approximations, turns out to be true, XES is a photon-in and photon-out coherent process and for a correct interpretation of spectral features an exact treatment has to be carried out[9]. When coherence and multi-electrons effects can be neglected, the picture of the NXES as an absorption followed by emission process is correct and NXES turns out to be proportional to the partial occupied symmetry-selected density of valence states. In the following we will derive the dependence of the NXES cross section from the occupied DOS treating the process as a photon-in and photon-out phenomenon.

1.2.1 XES cross section

Let us consider the x-ray scattering process in which an x-ray photon with energy $\hbar\omega_1$ is incident on a material and then an x-ray photon with energy $\hbar\omega_2$ is emitted as a result of the interaction. The cross section of this photon-in and photon-out process is given by the time-dependent perturbation theory, as for the XAS cross section, but this time the interaction Hamiltonian terms to be considered are the first-order of the quadratic term in the vector potential and the second-order perturbation of the linear term. The result is the famous Kramers-Heisenberg equation[10]

$$\frac{d\sigma}{d\Omega} \propto \sum_f \left| \left\langle f \left| \frac{e^2}{2mc^2} \vec{A}_2 \cdot \vec{A}_1 \right| i \right\rangle + \right.$$
$$\left. + \frac{e}{mc} \sum_m \left[\frac{\langle f|\vec{p}\cdot\vec{A}_2|m\rangle\langle m|\vec{p}\cdot\vec{A}_1|i\rangle}{E_m - E_i - \hbar\omega_1} + \frac{\langle f|\vec{p}\cdot\vec{A}_1|m\rangle\langle m|\vec{p}\cdot\vec{A}_2|i\rangle}{E_i - E_f - \hbar\omega_2} \right] \right|^2 \times \quad (1.21)$$
$$\delta(\hbar\omega_1 - \hbar\omega_2 - E_f + E_i)$$

where Ω is the solid angle, f, i and m are the final, initial and intermediate states, respectively, and E_f, E_i and E_m are their energies; $\vec{A}_1$ and $\vec{A}_2$ are the vector potentials of the incoming and outgoing radiation and the sums are over all the final and intermediate states available.

Each term in (1.21) represents a different scattering process, that is pictured in Figure 1.8 with Feynman diagrams: the first one comes from the first-order of the $\vec{A}^2$-type interaction and is the Thompson scattering (picture (a)), where the incoming photon $\hbar\omega_1$ is scattered by the system into the outgoing photon $\hbar\omega_2$; the second and third terms come from the second-order perturbation of the linear term in $\vec{A}$ and describe the absorption of a photon of energy $\hbar\omega_1$ followed by the emission of a photon of energy $\hbar\omega_2$ (second term, picture (b)) or the emission of a photon of energy $\hbar\omega_2$ followed by the absorption of a photon of energy $\hbar\omega_1$ (third term, picture (c)).

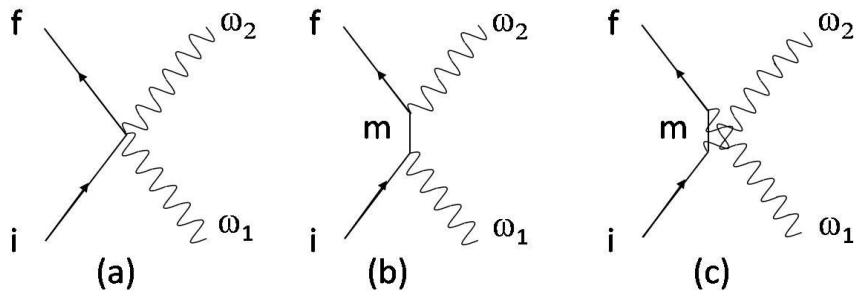

Figure 1.8. Feynman diagrams for the three photon-in and photon-out processes corresponding to the three terms in the Kramers-Heisenberg equation. (a) an incident photon ω_1 is scattered by the interaction with the system in the state i into a photon ω_2; the system is left in the state f. (b) the incident photon ω_1 is absorbed by the system that from the initial state i goes into the virtual state m. Then the photon ω_2 is emitted and the system is left in the final state f. When the incident photon energy is close to or above an absorption threshold the m state is a real unoccupied state and the this term dominates; (c) the emission of a photon ω_2 takes place before the absorption of a photon ω_1.

Far from absorption edges, terms from the second-order perturbation are negligible compared to the first one, but when the incident photon energy is close to or above the core-electron excitation threshold, the contribution of the second term dominates. As can be seen from (1.21), the denominator of the second term vanishes when the incident energy is resonant with an empty state energy and the second-order perturbation calculation breaks down. However, taking into account that the intermediate state has a finite lifetime, $\tau_m = \frac{\hbar}{\Gamma_m}$, because of the lifetime of the core-hole, then the energy E_m is replaced by $E_m + i\Gamma_m$ and the divergence is

removed. Since we are interested in the calculation of NXES cross section, that is performed with incident photons energies above an absorption threshold, the second term that describes the absorption followed by emission process is the dominant one and we can neglect the other minor contributions in the Kramers-Heisenberg equation. The result is

$$\frac{d\sigma}{d\Omega} \propto \sum_f \left| \sum_m \frac{\langle f|\hat{\varepsilon}_2 \cdot \vec{r}|m\rangle\langle m|\hat{\varepsilon}_1 \cdot \vec{r}|i\rangle}{E_m - E_i - \hbar\omega_1 - \frac{i\Gamma_m}{2}} \right|^2 \times \delta(\hbar\omega_1 - \hbar\omega_2 - E_f + E_i) \quad (1.22)$$

where the dipole approximation has been used and $\hat{\varepsilon}_1$ and $\hat{\varepsilon}_2$ are the vector polarizations of the incoming and outgoing photons; f, i and m are the final, initial and intermediate states, respectively; sums are on all the final and intermediate states available and Γ_m is the lifetime of the intermediate state.

Both RXES and NXES are described by this term, the main difference between the two is the nature of the wave-functions involved: in RXES both the intermediate and final states are usually localized, which makes electron-electron interactions and charge transfer effects important and, as a consequence, the one-electron picture can't be used. In NXES the final state is a continuum state, less influenced by the other inner electrons, so the one-electron picture is appropriate.

Details on the RXES cross section derivation and the validity of electron momentum conservation[11] as well as experimental examples regarding both weakly and strongly correlated systems can be found elsewhere[9]. In the following we will consider only the process where the core-electron is excited in a continuum state above the edge and the core-hole is filled by a valence band electron in a system where electron-electron correlations can be neglected. Under these assumptions, the single-particle picture can be applied and the final state is regarded as made by a conduction electron in a previously unoccupied continuum state with momentum $\vec{k}_e$ and a valence hole with momentum $\vec{k}_h$, while the intermediate state has a core-hole at energy ε_c and the photo-electron at $\vec{k}_e$. Neglecting the core-hole effect, all wave-functions can be written as Bloch functions and in addition, since the core-hole wave-function is localised, it can be approximated by the tight binding form as a sum of atomic core-orbitals over the lattice sites. The cross section is then given by[11]

$$\frac{d\sigma}{d\Omega} \propto \sum_{\vec{k}_h} \left| \sum_{\vec{k}_e} M_{c,h} \frac{M_{e,c}}{\varepsilon_e(\vec{k}_e) - \varepsilon_c - \hbar\omega_1 - \frac{i\Gamma}{2}} \sum_{\vec{R}} e^{i\vec{R}\cdot(\vec{q}_1 - \vec{q}_2 + \vec{k}_h - \vec{k}_e)} \right|^2 \times \delta(\hbar\omega_1 - \hbar\omega_2 - \varepsilon_h + \varepsilon_e) \tag{1.23}$$

where the sum over final states has been replaced by the sum over the valence-hole momentum $\vec{k}_h$ and that on intermediate states by the sum over the photo-electron momentum $\vec{k}_e$. $M_{e,c} = \langle e^* | \hat{\varepsilon}_1 \cdot \vec{r} | c \rangle$ is the matrix element of the transition of a core-electron into a continuum state and $M_{c,h} = \langle c | \hat{\varepsilon}_2 \cdot \vec{r} | h^* \rangle$ that for the transition of a valence electron h into the core-hole (the star denotes excited states). The sum over lattice sites, that stems from the Bloch function form of wave-functions, brings about the electron momentum conservation. When the wave-functions of the photo-electron and of the valence electron that fills the hole are better described by more localized states or by a linear combination of Bloch functions (for example due to the core-hole potential effect), the electron momentum conservation is lost and the emission spectrum samples all the Brillouin zone. Neglecting the momentum conservation and considering that from energy conservation we have

$$\begin{aligned} \varepsilon_e(\vec{k}_e) - \varepsilon_c &= \hbar\omega_1 \\ \varepsilon_e(\vec{k}_e) - \varepsilon_h(\vec{k}_h) &= \hbar\omega_1 - \hbar\omega_2 \end{aligned} \tag{1.24}$$

the sum over all final and intermediate states can be performed and the result for the cross section is

$$\frac{d\sigma}{d\Omega} \propto \frac{{M_{c,h}}^2 {M_{e,c}}^2}{(\varepsilon_e - \varepsilon_c - \hbar\omega_1)^2 + \Gamma^2/4} \times \rho_{occ}(-\varepsilon_h)\rho_{unocc}(\varepsilon_e) \tag{1.25}$$

When the exciting energy is far above the threshold, the density of unoccupied states is well approximated by a constant and the line shape of the emission spectrum is essentially proportional to the density of valence states. Like in XAS, the proportionality to the transition matrix element brings about selection rules that project the sampled DOS on a specific momentum component of the final state. NXES thus probes the momentum-projected occupied DOS of the material investigated.

In summary, NXES is a very powerful technique to investigate the electronic structure of materials; it is proportional to the unoccupied momentum-projected DOS and it can also provide momentum-resolved spectra, but many factors, like

core-hole potential effects or electron-phonon interactions can break the coherence needed for the electron momentum conservation to hold. RXES, in particular for system with strong electron-electron correlation, is even richer of information about the electronic structure of samples, but the analysis is not straightforward and the theoretical background needed for the interpretation is different from that presented here.

1.3 Real space multiple scattering approach to XAS

As was pointed out in previous paragraphs, core-level spectroscopies are powerful techniques for the investigation of materials; their spectra in fact depend on the detailed atomic structure and electronic properties of samples probed. However, extracting the information is not straightforward and most of the times the analysis has to be supported by *ab initio* simulations. This fact makes the progress in high brilliance SR sources and in experimental instrumentation necessary but still not enough to guarantee the success of core-level techniques in material science. Solid tools to handle the analysis are necessary and on them depends how quantitative these techniques can be. In the last years great progresses have been made on this side and a substantial number of *ab initio* codes are now available, based on different approaches.

A first big distinction splits these theoretical methods into two classes: the mono-electronic but multi-atomic approach and the multi-electronic but mono-atomic approach[12]. In the mono-electronic approach the final and initial states are approximated by single-electron wave-functions and the multi-atomic nature of the material is taken into account. The multi-electronic approach, instead, retains the multi-electron nature of the quantum states involved, but at the expense of a simplified picture of the solid around the central atom, that is usually treated as a perturbation on the central atom potential. The reason for this distinction is in the nature of the states involved in the transition. The core-state is always localised, but the final state can be a localised empty state or it can be in the continuum. In the latter case the one-electron picture is a valid approximation, while in the first case electron-electron interactions and core-hole potential effects are relevant and a multiplet approach, that considers several possible electronic states, is more appropriate.

A method in particular will be treated in details in this thesis: it is the real space multiple scattering (RSMS) approach applied to XAS spectroscopy[13,14,15,16]. It belongs to the first class and it combines the Green's function formalism with the

multiple scattering theory to compute the absorption coefficient. Many codes are based on the MS and Green's function formalism, they are very efficient and versatile as no explicit calculation of final states is needed and no long-range order of the system is required, contrary to all band structure methods. This formalism has also the merit of accounting for both XANES and EXAFS regions within a unique framework where the limit between the two is marked by the applicability of the path-by-path expansion of the scattering propagator.

The starting point is the expression of the absorption coefficient

$$\sigma = 4\pi^2 \hbar\omega\alpha |\langle f|\hat{\varepsilon}\cdot\vec{r}|i\rangle|^2 \delta\left(E_f - E_i - \hbar\omega\right) \tag{1.26}$$

with the one-electron Green's function propagator given by

$$G(\vec{r},\vec{r}',E) = \sum_f \frac{\psi_f^*(\vec{r})\psi_f(\vec{r}')}{E - E_f - i\Gamma}. \tag{1.27}$$

It accounts for the propagation of a quasi-particle of energy E_f from $\vec{r}$ to $\vec{r}'$. A quasi-particle is a nearly-free particle moving in an optical potential whose wave-function is a solution of the Dyson equation. In the XAS case, the quasi-particle is the photo-electron and the optical potential accounts for the core-hole and the exchange-correlation between the photo-electron and the valence electrons. The exchange-correlation term is described by an energy dependent function since the electron-electron interaction gets weaker with increasing kinetic energy of the photo-electron. With the appropriate potential, the Dyson equation describing final states in the absorption process is written

$$\left(\frac{p^2}{2m} + V'_{coul} + \Sigma(E)\right)\psi_f = E\psi_f. \tag{1.28}$$

It resembles the time-independent Schrödinger equation with a potential made by the sum of a Coulomb term and a self-energy factor $\Sigma(E)$ that plays the role of the exchange-correlation dynamically-screened potential[15,16]. The Coulomb term includes an appropriately screened core-hole and the self-energy is usually complex valued, making the Hamiltonian for the excited states non-hermitian. As a consequence, the final states are multiplied by a damping factor and characterized by a finite lifetime. The influence of the self-energy on the calculated spectra is therefore double: the real part determines an energy shift of the spectral features compared to ground state calculations, while the imaginary part

introduces a broadening of the spectral features due to the core-hole lifetime; however, in most *ab initio* codes it can be adjusted to account also for the experimental resolution in a self-consistent way.

The Green's function related to the solution of the Dyson equation can be substituted in the absorption coefficient formula taking advantage of the spectral representation

$$G(\vec{r},\vec{r}',E) = \sum_f |f\rangle\delta(E-E_f)\langle f| = -\frac{1}{\pi}\mathrm{Im}G(E). \tag{1.29}$$

to substitute the delta function in the absorption coefficient

$$\begin{aligned}\mu(E) &\propto \sum_f |\langle f|\hat{\varepsilon}\cdot\vec{r}|i\rangle|^2\delta(E-E_f) = \\ &= \sum_f \langle i|\hat{\varepsilon}\cdot\vec{r}'|f\rangle\delta(E-E_f)\langle f|\hat{\varepsilon}\cdot\vec{r}|i\rangle\end{aligned} \tag{1.30}$$

The result is

$$\mu(E) \propto -\frac{2}{\pi}\mathrm{Im}\langle i|\hat{\varepsilon}\cdot\vec{r}'G(\vec{r},\vec{r}',E)\hat{\varepsilon}\cdot\vec{r}|i\rangle. \tag{1.31}$$

The next step is to write the Green's function propagator. Without any assumption on the potential, solving the Dyson equation is really computationally demanding. A strong step forward would be provided by the use of a spherically symmetric potential: in this case the multiple scattering theory provides convenient results and the Green's function propagator can be re-expressed as a sum of a central atom contribution and a scattering term, recalling the experimental spectra where an oscillatory contribution is superimposed on an atomic smooth background.

To gain spherical symmetry, the potential is first expanded into contributions from each atomic site

$$V'_{coul} + \Sigma(E) = \sum_{\vec{R}} v_{\vec{R}}(\vec{r}-\vec{R}); \tag{1.32}$$

then the muffin-tin approximation is applied: each atomic site is the centre of a sphere, inside which the electron density is spherically averaged, while in the outside region the potential is fixed to a constant value, given by the average of the electron densities exceeding the muffin-tin spheres. The next task is writing the total propagator within a muffin-tin potential. The spherical symmetry allows the

expansion of the photo-electron wave-function into partial waves of definite angular momentum $L = (l, m)$. To account for the scattering process each partial wave has to be propagated in a muffin-tin potential. This process can be reduced to the repetition of two steps: the propagation of the photo-electron wave-function in the constant potential region and the scattering from each atomic site, represented by a spherical potential, it undergoes. The propagation in the constant potential between site i and j is described by the free electron propagator $G^0_{L_i,L_j}$ while the scattering of an incoming partial wave of definite momentum L into an outgoing partial wave of momentum L' by a spherical potential at a site i is described by the scattering matrix $G^i_{L,L'}$ that is diagonal in the momentum indices.

The Green's function total propagator can be always written as the sum of a free term and an interaction term[17]

$$G = G^0 + G^0 T G^0 \tag{1.33}$$

where T is the scattering matrix accounting for all possible scattering events. A general form for the matrix T is given by[17]

$$T = \sum_{i,j} \tau^{ij} = \sum_{i,j} \left(t^i \delta_{ij} + \sum_{i \neq k} \tau^{ik} G^0 t^j \right) \tag{1.34}$$

where the scattering at a site i is given by t^i.
Writing (1.33) in a spherically symmetric potential for the case of the absorption process gives

$$G(\vec{r}, \vec{r}', E) = \sum_L R_L(\vec{r}) S_L(\vec{r}') + \sum_{L,L'} R_L(\vec{r}) T^{00}_{L,L'}(E) R_{L'}(\vec{r}') = G^C + G^{SC} \tag{1.35}$$

where the free propagator has been expanded into spherical harmonics: $L = l, m$, R_L and S_L are the regular and irregular solutions of the Schrödinger equation for the radial part (the angular dependence is omitted and is given by the spherical harmonics) with $\vec{r}$ and $\vec{r}'$ inside the muffin-tin sphere. The total propagator written in this way is naturally divided into a central atom contribution G^C and a contribution from the surrounding G^{SC}, where the key ingredient carrying the structural information is T^{00}, that is simply the more general scattering path operator $T^{ij}_{L,L'}$ calculated on the central atom. $T^{ij}_{L,L'}$ physically represents the sum of all contributions corresponding to scattering paths starting from a spherical wave

L at site i and ending as a spherical wave L' at site j[5]. Since in the absorption process the fine structure is due to interference between the original wave with the backscattered waves at the central atom position, for the absorption cross section $T^{ij}_{L,L'}$ is calculated at $i = j = 0$. Its more general form is given by the inverted-matrix element[13]

$$T^{ij}_{L,L'} = [\mathbb{I} - G^0 t]^{-1} G^0 |^{ij}_{L,L'} \tag{1.36}$$

where G^0 contains the scattered amplitude intensities of an incoming wave of momentum L into a scattered wave of momentum L' and $t^{ij}_{L,L'}$ describes the expansion of a spherical wave of momentum L at site i in spherical harmonics on site j. G^0 is diagonal as the scattering by a spherically symmetric potential induces on a partial wave only a phase shift:

$$G^0_{L_i,L'_j} = e^{i\delta_i} \sin(i\delta_l)\delta_{ij}\delta_{L,L'} \tag{1.37}$$

while $t^{ij}_{L,L'}$ couples only distinct atomic sites. In the end the scattering contribution to the absorption cross section is given by

$$G^{SC} \propto e^{i\delta_l}[\mathbb{I} - G^0 t]^{-1} G^0 e^{i\delta_{l'}} \tag{1.38}$$

Calculating the effect of all possible scattering paths is then equivalent to the inversion of the matrix $[\mathbb{I} - G^0 t]$. The matrix $T^{00}_{L,L'}$ can be expressed as a sum over all the multiple scattering paths (the so called path-by-path expansion). In the EXAFS region the convergence of the path-by-path expansion is rapid as at high photo-electron energy the scattered amplitudes are small and thus contributions of multiple scattering paths are often negligible. The path-by-path expansion is very useful since it distinguishes contributions to the spectrum due to specific scattering paths. The convergence however fails in the XANES region, where the inversion of the matrix is often needed to take all the scattering paths into account, the so called full multiple scattering calculation.

Substituting in (1.31) the Green's function propagator, we obtain for the absorption coefficient the separation into a central atom contribution and a scattering part

$$\mu(E) = \mu_0(E)[\mathbb{I} - \chi(E)] \tag{1.39}$$

where $\chi(E)$ is given by

$$\chi(E) \propto -\frac{2}{\pi}\mathrm{Im}\sum_{L,L'} M_L(E)T^{00}_{L,L'}(E)M_{L'}(E), \tag{1.40}$$

so that the absorption coefficient is reduced to the calculation of atomic dipole-matrix elements $M_L = \langle i|\hat{\varepsilon}\cdot\vec{r}|R_L\rangle$ and the scattering path operator$T^{00}_{L,L'}$.

The Green's function formalism can be adopted also to express physical quantities like the electron density distribution. The general relation is given by

$$\rho(E) \propto -\frac{1}{\pi}\mathrm{Im}\int d^3rG(\vec{r},\vec{r},E) = -\frac{1}{\pi}\mathrm{Im}G(E), \tag{1.41}$$

so that applying the muffin-tin approximation, we can substitute the formula just derived for the Green's function propagator and obtain also for the electron density a formulation where a scattering contribution is summed to the central atom term

$$\rho(E) = \rho_0(E)[\mathbb{I} + \chi(E)] \tag{1.42}$$

where $\chi(E)$ depends on the same scattering path operator of the absorption coefficient case. Because of the similarity between $\mu(E)$ and $\rho(E)$, it is widely thought that the XAS measures the local projected DOS. This interpretation can be misleading because of the importance of the core-hole potential that affects the electron distribution, therefore the *L*-DOS measured by the XAS spectrum is affected by the presence of a core-hole and can differ substantially from the ground state *L*-DOS[14].

Within the RSMS approach the calculation of the absorption cross section avoids explicit calculation of final states and doesn't require any structural order of the scatterers. Moreover, in a single calculation the simulated spectrum and the local projected DOS are obtained as both are based on the same matrix inversion.

The starting point of RSMS codes is the construction of the appropriate muffin-tin potential describing the material under study to solve the radial Schrödinger equation. Once this is done, the calculation of the absorption coefficient and of the electron densities is accomplished by calculating dipole-matrix elements between a core-state and the partial waves, and performing the matrix inversion or the path-by-path MS expansion.

The RSMS approach is really powerful and versatile, but one has to be aware of approximations that led us to the final formulation. The strongest one is surely

the muffin-tin approximation: it gives a reliable potential for the core-shell electrons, as they really have spherical symmetry, but it cancels out the details of the outermost electron densities, that are distorted by the bonds with the surrounding atoms. In addition, the approximation of a constant potential outside the spheres can be too strong if the structure is not close-packed, so that the interstitial region occupies a relevant volume of space. The muffin-tin approximation is therefore suitable for close-packed structures and for high kinetic energies of the photo-electron, when the effective scattering potential is due to the core-electrons densities and the details of the potential are unimportant. The error induced by the muffin-tin approximation is therefore small in the EXAFS region, while in the XANES it can be relevant. Within the RSMS formalism, therefore, the crucial point is the construction of a potential that best reproduces the material under examination. Two things that can be done before dropping the muffin-tin approximation are: allow a slight superposition of the muffin-tin spheres, in order to minimize the interstitial region, and calculate the potential in a self consistent way. Both are implemented in the FEFF code used to analyze data along this thesis. FEFF allows also the tuning of variables like the form of the self-energy, the core-hole treatment and so on. To summarize, the advantages of using a RSMS based code are:

1. no explicit calculation of the final states is needed, but the Green's function propagator is calculated and the physical quantities are obtained by integration in the complex-plane.
2. no long-range order is required, allowing the study of amorphous solids or alloys.
3. the calculations for a volume around the absorber including 100 atoms can be carried out with reasonable computational resources as the spherical harmonics in a limited range potential converge rapidly.

1.4 Soft x-ray appearance potential spectroscopy

The core-level spectroscopies discussed previously both use x-ray photons to probe matter and are strictly related to high brilliance SR sources. Easily available alternative probes for core-level excitation are accelerated electrons: they are easily produced by a hot cathode and their kinetic energy is increased simply by applying a high voltage to values in the range of soft x-rays. Moreover, electrons are easily deflected by electromagnetic fields, therefore acting on their trajectory is far more

easy than it is on x-rays. Optical systems are in fact made by electromagnetic lenses, very handy in comparison with x-ray optics. Electrons therefore are good and cheap candidates to substitute x-rays as a source of core-level excitation if one wants a core-level spectroscopy close at hand. The main advantage of using electrons is that they are easily produced and controlled. However, due to their strong interaction with matter, a variety of products is emitted during the probe-sample interaction, so that the signal of interest is often buried into a large background.

We present in this paragraph a technique developed in the '70s that is called soft x-ray appearance potential spectroscopy (SXAPS) and it is basically the analogue of XAS coupled with a fluorescence detection scheme but with accelerated electrons as the probe.

The possibility of exciting core-states by means of accelerated electrons was known since 1911, when Frank and Hertz[18] performed their experiment on Hg vapours where the current signal from the anode was characterized by negative peaks in correspondence of determined potentials, that they called appearance potentials. The peaks were at the threshold potentials for the excitation of core electrons in Hg. The current was lowered due to the opening of a new interaction channel that left the electrons without sufficient energy to reach the anode. Techniques based on the same principle were developed to measure bindings energies, then in 1970 Park and Houston[19] developed the first SXAPS apparatus for the analysis of solid surfaces: an electron beam was used to excite a core-state and the cross section of the process was monitored through the characteristic fluorescence emission. Actually, the total emission was detected by means of a photocathode and sometimes a lower threshold energy was imposed with filters. The key point of their apparatus was the introduction of a real-time differentiation of the signal through the use of a lock-in amplifier and an oscillating voltage on the sample. In this way the sudden increase in the signal was clearly visible as the background is almost a linear function of the incident energy. A number of alternative detection schemes were tried in the following years[20,21], but after a discrete success, this technique was almost abandoned. The reasons are various, one is the advent of SR laboratories, but also the lack of a solid theoretical background for the electron-matter interaction at play.

A SXAPS apparatus consists of a source of electrons, usually a hot cathode, that are accelerated to the desired energy by a high potential applied to the sample. The detection stage depends on the product of the decay that one wants

to measure. It can be the Auger electrons yield or the amount of characteristic photons emitted during the fluorescence decay of the core-hole. Depending on the detected product, the technique is called Auger APS or soft x-ray APS.
The first SXAPS set-ups were using photocathodes to detect the photons emitted by the sample and the signal was differentiated to enlighten the threshold energies. The need to differentiate the signal was imposed by the high background covering the low fluorescence yield. At soft x-rays energies the fluorescence yield is very low compared to the Auger electron yield as can be seen in Figure 1.9; in addition, the interaction of incident electrons with matter causes the emission of a large bremsstrahlung radiation that forms a continuous background of emitted photons covering a range of energy from that of the incident beam down to zero. The bremsstrahlung radiation is the dominant contribution to the total emission and the fluorescence signal is almost 10^{-4} of the total emitted radiation. The signal to noise ratio is therefore very low in the basic detection scheme.

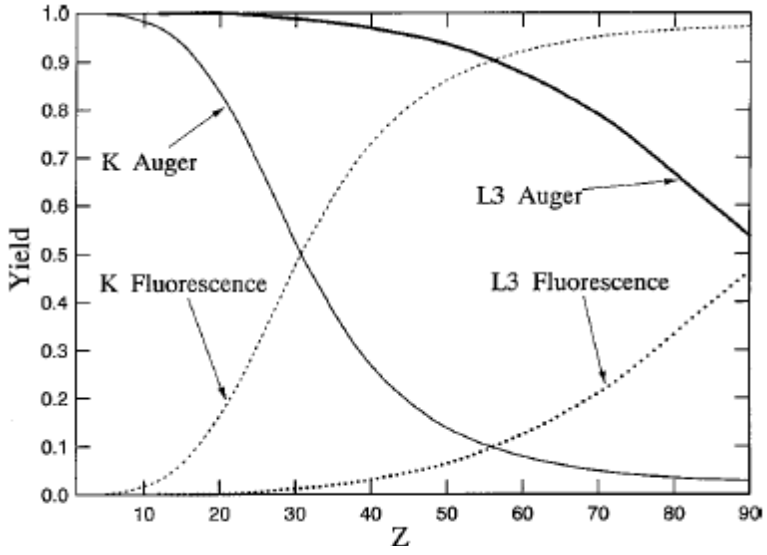

Figure 1.9. Fluorescence and Auger electron yield dependence on the atomic number for K- and L-edges

1.4.1 SXAPS cross section

The derivation of the cross section for core-electron excitation by means of accelerated electrons is related to that of XAS. The physical process is shown in Figure 1.10 where the Fermi level of the sample and of the electron source have been aligned: an incident electron at energy E_0 hits the sample and gives part of its energy to a core-level electron, which is promoted to an empty state E_{f_2} above the

Fermi level[20]. The incident electron goes down to an empty level E_{f_1}, exactly as the excited electron. The core-hole decay can take place with the same two processes as in the XAS case: emission of a characteristic photon or Auger decay.

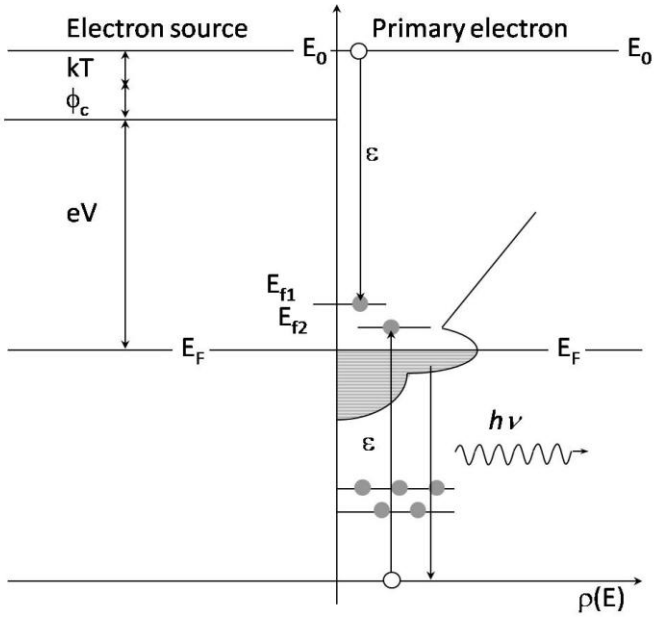

Figure 1.10. Energy diagram of the physical process: incident electrons are produced at the source and accelerated by the applied potential at E_0. In the interaction with the atoms of the solid the primary electron loses an amount of energy equal to ε and higher than the threshold energy and excites a core-electron in E_{f_2} above the Fermi level. After the interaction the primary electron occupies a state at E_{f_1}. The core-hole is filled by electrons from the occupied density of states with the consequent emission of fluorescence photons.

As we already pointed out, the detected signal originates partly from the bremsstrahlung radiation, Y_B, and partly from core-hole fluorescence decay, D_C. The total yield can be written as[22]

$$Y_{tot}(E_0) = Y_B(E_0) + D_C\Gamma_{if} \tag{1.43}$$

where Γ_{if} is the transition rate from the initial to the final state caused by the Coulomb interaction between the core-electron and the incoming electron. Since Y_B is almost linearly dependent on the incident energy, modulations in the total emitted radiation are due to the Γ_{if} term. In principle the transition takes place with both the conservation of the total energy and the total momentum, but due to the strong interaction between electrons and the solid and because of the highly

localized core-hole, the momentum conservation is relaxed and the transition rate is derived within the energy conservation alone.

The probability Γ_{if}, in a one-electron picture, is obtained from Fermi's golden rule where the initial state is a core-electron level and the final state is in the continuum, therefore it is proportional to the density of final states available. In the SXAPS process, the final states of the incident and the excited electrons are empty valence state wave-functions; therefore at a given incident energy the density of available final state is proportional to the product of the empty DOS calculated at E_{f_1} and E_{f_2}. In addition, since in the transition the incident electron can lose any amount of energy higher than the ionization threshold, the available final states at a given incident energy are given by integration on both E_{f_1} and E_{f_2}. Γ_{if} is then given by

$$\Gamma_{if}(E_0) \propto \frac{2\pi}{\hbar}\left|M_{if}\right|^2 \int dE_c dE_{f_1} dE_{f_2} \rho(E_c)\rho\left(E_{f_1}\right)\rho\left(E_{f_2}\right) \times \\ \times \delta\left(E_0 + E_c - E_{f_1} - E_{f_2}\right) \tag{1.44}$$

where the delta function accounts for the conservation of total energy and the integration is also on the energy of the core-state. Since the core-level is highly localized, the density of final states probed is highly localized on the absorber. Approximating $\rho(E_c)$ with a delta function, we end up with a single integration variable

$$\Gamma_{if}(E_0) \propto \frac{2\pi}{\hbar}\left|M_{if}\right|^2 \int \rho\left(E_0 + E_c - E_{f_2}\right)\rho\left(E_{f_2}\right) dE_{f_2} \tag{1.45}$$

and rewriting the equation as a function of the exchanged energy $\varepsilon = E_{f_2} - E_0$, the cross section is given by

$$\Gamma_{if}(E_0) \propto \frac{2\pi}{\hbar}\left|M_{if}\right|^2 \int_{E_c+E_F}^{E_0-E_F} \rho(E_0 - \varepsilon)\rho(E_c + \varepsilon)\, d\varepsilon \tag{1.46}$$

Inserting the result in (1.43) gives

$$Y_{tot}(E_0) = Y_B(E_0) + C(E) \int_{E_c+E_F}^{E_0-E_F} \rho(E_0 - \varepsilon)\rho(E_c + \varepsilon)\, d\varepsilon \tag{1.47}$$

Taking the derivative of this formula and approximating $C(E)$ as a constant gives

$$\frac{dY_{tot}(E_0)}{dE_0} = C\rho(E_c + E_F)\rho(E_0 - E_F) + \\ +C\int_{E_c+E_F}^{E_0-E_F} \rho(E_c + \varepsilon)\frac{d\rho(E_0 - \varepsilon)}{dE_0}d\varepsilon + \frac{dY_B(E_0)}{dE_0}. \quad (1.48)$$

The dependence of the SXAPS cross section on the self-convolution of the unoccupied DOS, as shown by (1.46), carries structural and electronic information about the sample measured. The physical information is less immediate with respect to XAS measurements, where the proportionality to the unoccupied DOS is direct. The analysis of SXAPS spectra is therefore not straightforward and at the time of its major diffusion the physical information extracted was very basic (electron binding energies, chemical shifts) since no advanced analysis tools, like *ab initio* modelling of the DOS, were used. In chapter 5 we will present a new implementation of a SXAPS apparatus which presents a good signal-to-noise ratio and we will couple the spectral analysis with efficient *ab initio* codes.

In (1.48) the dominant contribution is given by the first term, that if the Fermi energy is set at zero and the incident energy equals the ionization threshold E_c is proportional to the square of the DOS at the Fermi level. For samples whose electronic structure is dominated by the discontinuity at the Fermi level, (1.48) represents a good approximation and the derivative of the SXAPS spectrum resembles the unoccupied DOS.

In the previous derivation, the matrix element has been treated as a constant, but indeed it has a strong dependence on the incident energy. The exact derivation of the dependence of the ionization cross section from the incident energy is quite complicated and can be found elsewhere[23]. We limit to show in Figure 1.11 its universal dependence on the ratio between the primary electron energy E_p and the ionization threshold E_i. Across the ionization threshold the cross-section has a steep increase; this add an additional energy dependence of the SXAPS spectral line shape that has to be taken into account if quantitative information wants to be extracted.

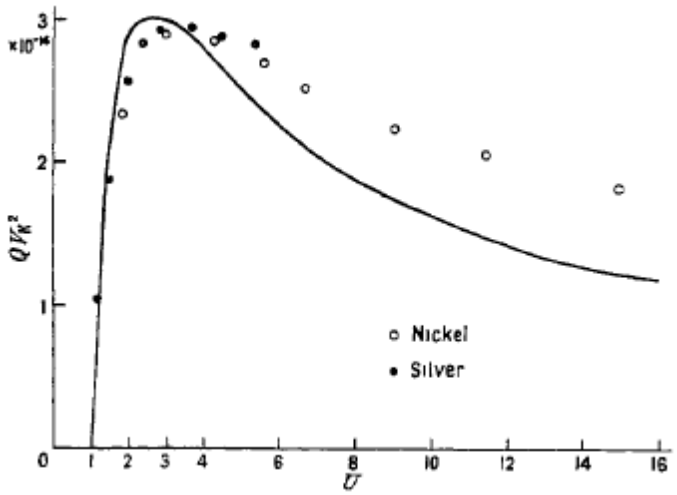

Figure 1.11. K-edge ionization cross-section by electron impact as a function of $U = E_p/E_i$ *the ratio between the primary electron energy* E_p *and the ionization threshold energy* E_i*. The function has its maximum between 2 and 3 and it increase rapidly around the threshold.*

As a concluding remark, we recall that in the XAS cross section the selection rules for the angular momentum were given by the dipole matrix element. In SXAPS the transition is mediated by the coulomb interaction

$$M_{if} = \left\langle \psi_{E_0}\psi_{core} \left| \frac{e^2}{4\pi\varepsilon_0 r} \right| \psi_{f_1}\psi_{f_2} \right\rangle. \tag{1.49}$$

Also in this case the wave-functions and the operator involved can be expanded in Legendre polynomials functions to separate the angular dependence and derive eventual selection rules. Even if from calculations no strict selection rule is found, an "approximated dipole-selection rule" has been reported from experimental experience.

Appendix 1

1.1 Self-absorption

Referring to the scheme given in Figure 1.6, to calculate the dependence of the FLY from the absorption coefficient we must follow step by step the process leading to the detection of a fluorescence photon. The basic steps are the absorption of an incoming x-ray photon of energy E at a certain depth, followed by the emission of a fluorescence photon that to be detected has to travel a certain path, escape the sample surface and be detected.

The incident photon enters the sample with an angle α respect to the sample surface. The probability it has to reach a depth x', from the Lamber-Beer law, is equal to $e^{-\frac{\mu_T(E)x'}{\sin\alpha}}$, where $\mu_T(E)$ is the total absorption coefficient of the sample and it is multiplied by the distance the photon has to travel to penetrate till x'. The probability that the photon will be absorbed by the volume element between x' and $x' + dx'$ is $\mu_i(E)\frac{dx'}{\sin\alpha}$, where $\mu_i(E)$ is the absorption coefficient of the element of interest. The probability that a fluorescence photon will be emitted in the solid angle $\Delta\Omega$ covered by the active area of the detector is the fluorescence yield ε times $\Delta\Omega/4\pi$. Once the photon is emitted, the probability it escapes from the surface at angle β is equal to $e^{-\frac{\mu_T(E_F)x'}{\sin\beta}}$.

Multiplying all these probabilities and integrating over the depth, from the surface to a certain distance d, the ratio of the fluorescence yield to the incident beam intensity is given by:

$$\frac{I_f}{I_0} = \frac{\epsilon\Delta\Omega}{4\pi}\frac{\mu_i(E)}{\sin\alpha}\int_0^d e^{-\left(\frac{\mu_T(E)}{\sin\alpha}+\frac{\mu_T(E_f)}{\sin\beta}\right)x'}dx' \tag{1.50}$$

$$\frac{I_f}{I_0} = \frac{\epsilon\Delta\Omega}{4\pi}\frac{\mu_i(E)}{\mu_T(E) + \mu_T(E_f)\dfrac{\sin\alpha}{\sin\beta}}\left[1 - e^{-\left(\frac{\mu_T(E)}{\sin\alpha}+\frac{\mu_T(E_f)}{\sin\beta}\right)d}\right] \tag{1.51}$$

If the sample is thick and $\beta = 90° - \alpha$, like in most FLY detection schemes, the exponential term can be neglected and the final formula is:

$$\frac{I_f}{I_0} = \frac{\epsilon d\Omega}{4\pi}\left(\frac{\mu_i(E)}{\mu_T(E) + \mu_T(E_f)\tan\alpha}\right) = \frac{\epsilon d\Omega}{4\pi}\mu_i(E)g(E) \tag{1.52}$$

The energy dependent function $g(E)$ has at the denominator $\mu_T(E)$, the total absorption coefficient that contains $\mu_i(E)$, therefore the fluorescence yield isn't linearly proportional to the absorption coefficient of the element of interest. The consequence on the spectral line shape is a suppression of the fine structure above the edge, in fact when $\mu_i(E)$ increases, it also increases the denominator of $g(E)$ so that the effect is partially cancelled out and the oscillations of the spectrum are not as pronounced as they should be if we were measuring $\mu_i(E)$. Physically what happens is that an increase in the absorption coefficient corresponds to a reduced penetration depth of the beam in the sample. This decrease of the active volume lessens the amount of atoms of the selected element involved in the process, counteracting the behaviour of the absorption coefficient. To measure the effective absorption coefficient, the volume involved in the absorption process should be the same instead of varying with the energy.

As discussed previously in the chapter, the geometry of the set-up has a great influence on the depth sensitivity of XAS measurements. Following a line of reasoning similar to that used in the calculation of the self-absorption effect, the information depth λ_f can be obtained. λ_f is defined as the expectation value of the depth, perpendicular to the sample surface, at which the fluorescence photon is generated. Assuming the probability of detecting a photon emitted at the surface as 1, the probability that a photon emitted at depth x reaches the detector is lowered by a factor

$$e^{-\left(\frac{\mu_T(E)}{\sin\alpha}+\frac{\mu_T(E_f)}{\sin\beta}\right)x} \tag{1.53}$$

The expectation value of x is then

$$\lambda_f = \frac{\int_0^\infty x e^{-\left(\frac{\mu_T(E)}{\sin\alpha}+\frac{\mu_T(E_f)}{\sin\beta}\right)x} dx}{\int_0^\infty e^{-\left(\frac{\mu_T(E)}{\sin\alpha}+\frac{\mu_T(E_f)}{\sin\beta}\right)x} dx} = \frac{\sin\alpha}{\mu_T(E) + \mu_T(E_f)\frac{\sin\alpha}{\sin\beta}} \tag{1.54}$$

This expression means that 68% of the fluorescence photons detected are generated in the layer between the surface and λ_f.

1.2 Dead-time effect

A detection stage that uses a pulse-counting detector to discriminate and count photons can exhibit non-linearity effects, that is the number of photons detected m is less than the number of photons impinging on the detector n. The cause for this effect is the dead-time of the amplifier used in the signal elaboration sequence. Each photon striking the active area of the detector generates a charge pulse proportional to its energy. The electric field of the detector collects the charge pulse and send the signal to a pulse-forming amplifier. The amplifier integrates the pulse and produces as output a Gaussian-shaped voltage signal with a height proportional to the charge collected, hence to the photon energy. The integration is obviously not instantaneous and each pulse-counting detector is characterized by a dead-time τ, defined as the interval of time the amplifier is left blind during the elaboration of the signal of a single photon. Two photons arrived to close in time are therefore processed as a single event, giving rise to the pile-up effect. The number of photons detected at the end of the signal processing m and the number of photons arrived on the detector n are thus different because of the dead-time effect. Data can be corrected if the relation between m and n is known.

Solid state detectors belong to the class of paralyzable detectors, that reacts to the arrival of a second photon before a dead-time is passed from the first one by extending further the dead-time. Paralyzable detectors, therefore are unable to distinguish two events separated by a time-delay less than τ. From statistical considerations, the relation between the real number of photons n and the detected photons m for a paralyzable systems turns out to be

$$m = ne^{-n\tau} \tag{1.55}$$

that can be inverted numerically[24] if one knows the dead-time τ of the detection system used[3].

[1] A. Kodre, J. P. Gomilsek, A. Mihekic and I. Arcon, *Rad. Phys Chem.* ***75***, 188 (2005).

[2] D. E. Sayers, E. A. Stern, F. W. Lytle, *Phys. Rev. Lett.* ***27***, 1204 (1971).

[3] G. Bunker, *Introduction to XAFS*, (Cambridge University Press, 2010).

[4] L. Tröger, D. Arvanitis, K. Baberschke, H. Michaelis, U. Grimm, E. Zschech, *Phys. Rev. B* ***46***, 3283 (1992).

[5] C. Brouder, *J. Phys. Condens. Matter* ***2***, 701 (1990).

[6] C. Brouder, M. F. Ruiz Lopez, R. F. Pettifer, M. Benfatto, C. R. Natoli, *Phys. Rev. B* ***39***, 1488 (1989).

[7] J. Stohr, *NEXAFS Spectroscopy*, (Springer, Berlin, 1992).

[8] M. Katsikini, E. C. Paloura, T. D. Mooustakas, *J. Appl. Phys.* ***83***, 1437 (1998).

[9] A. Kotani, S. Shin, *Rev. Mod. Phys.* ***73***, 203 (2001).

[10] J. J. Sakurai, *Advanced Quantum Mechanics*, (Addison-Wesley, 1967), Chap. 2.

[11] Y. Ma, *Phys. Rev B* ***49***, 5799 (1994).

[12] Y. Joly, *X-ray absorption spectroscopy: the monoelectronic approach*, HERCULES lecture, (2012).

[13] A. Di Cicco, *La spettroscopia di raggi X: sviluppo di un nuovo metodo d'analisi e applicazioni*, PhD Thesis, (1991).

[14] A. L. Ankudinov, B. Ravel, J. J. Rehr, S. D. Conradson, *Phys. Rev. B* ***58***, 7565 (1998)

[15] J. J. Rehr, R. C. Albers, *Rev. Mod. Phys.* ***72***, 621 (2000).

[16] J. J. Rehr, A. L. Ankudinov, *Coord. Chem. Rev.* ***249***, 131 (2005).

[17] J. S. Faulkner, G. M. Stocks, *Phys. Rev. B* ***21***, 3222 (1980).

[18] J. Franck, G. Hertz, *Verh. D. Deutsch. Phys. Ges.* ***16***, 12 (1911).

[19] R. L. Park, J. E. Houston, D. G. Schreiner, *Rev. Sci. Instr.* ***41***, 1810 (1970).

[20] Y. Fukuda, *Analytical Sciences* ***26***, 187 (2010).

[21] G. Ertl, J. Küppers, *Low Energy Electrons and Surface Chemistry*, (VCH, 1985).

[22] P. O. Nilsson, J. Kanski, *Surf. Sci.* ***37***, 700 (1973).

[23] C. R. Worthington, S. G. Tomlin, *Proc. Phys. Soc. A* ***69***, 401 (1956).

[24] G. Ciatto, F. d'Acapito, F. Boscherini and S. Mobilio, *J. Synchrotron Rad.* ***11***, 278 (2004).

Chapter 2

Nitride semiconductors

This chapter is dedicated to the introduction of two classes of materials: the nitride semiconductors, with particular attention on GaN, InN and their alloy system, and dilute nitride semiconductors. Both these classes of materials are of fundamental importance in optoelectronic, photovoltaic and telecommunication technologies and some of them are already used in commercially available devices. Even if already in use, the research on these materials is still very active. In fact, nitrides with low concentrations of defects are still difficult to obtain and research is trying to improve their quality and performances. Dilute nitrides, on the other hand, have a more mature technology but show striking deviations from the expected behaviour of the electronic structure that are still under study. Chapters 3 and 4 of this thesis will present characterization of samples belonging to these classes of materials by means of core-level spectroscopies, but formerly we introduce their most important characteristics.

III-nitrides are nowadays one of the most important classes of semiconducting materials after Silicon and Gallium Arsenide. They are divided into two categories: stoichiometric nitrides, where 50% of constituent atoms are nitrogen atoms, and dilute nitrides, synthesized by substituting a small amount of anions in a III-V semiconductor with nitrogen atoms. Both those classes of materials have been actively studied in last decades.

Dilute nitrides raised the interest of researchers since the discovery that a small amount of N atoms induces a huge reduction of the band gap of GaAs, while it was expected to increase to go towards the higher value of GaN. This unexpected effect, surely interesting from the point of view of basic physics, matched perfectly with the technological interest of having the GaAs direct-gap

tuned to 1.3-1.5 μm wavelength, opening the way to telecommunication devices integrated on GaAs.

Stoichiometric nitrides, on the other hand, have direct band gaps with values going from 6.4 eV for AlN to 0.64 eV for InN. This alloy system, therefore, can cover continuously all the energy range from the UV to the IR, if a proper control on the growth procedure is reached. Although they have lots of other interesting properties that make them worth studying materials, the great scientific interest raised by nitrides in last decades is mostly due to their promising future as the leading alloy system for optoelectronic and photovoltaic devices. Nitride technology has been developed only in the last decades but the production of GaN and AlN is today obtained with various growth methods even in bulk form. This advance is in strong contrast with the level of InN deposition technology that, even if in rapid development, is still not fully mature. Realization of high quality film and heterostructures of InN and of its alloys with GaN and AlN is still a field of basic research.

2.1 GaN, InN and their alloy system

In last decades the interest in nitrides has seen a steep increase and a large amount of resources have been devoted to the understanding of their fundamental physics. The most studied nitride is GaN. Its fame is related to the blue LED, whose first implementation dates back to the early '90[1]. This new device was a great breakthrough in optoelectronics and had an enormous technological impact since it permitted the realisation of full-colour LED displays and increased the capability of disk data-storage thanks to blue laser-diodes. Its principle of operation is a GaN *p-n* junction with Ga-rich InGaN quantum wells (QWs) sandwiched in the active region. Before the advent of GaN, the UV-blue wavelength range was not covered by semiconductors because of the lack of materials with wide enough direct band gap. GaN instead has a 3.4 eV energy gap at room temperature, ideal to cover the UV-far visible region of the electromagnetic spectrum.

Recently also InN has drawn the attention of researchers because of its small band gap and its surprisingly good electrical transport properties. Since 30 years ago not much attention was paid on this material. Then, the success of GaN pushed forward the research on nitrides to lower down the wavelength covered by its alloy systems and interest on InN rapidly increased. Particularly relevant was the debate around the value of its band gap. InN, in fact, is very hard to grow and in its early stage of research it was produced in polycrystalline form by sputtering

methods. Characterisation of those poor-quality films led to a wrong evaluation of the fundamental gap, estimated around 1.9 eV through absorption edge determination. Only when better quality single-crystal layers became available the actual room temperature value was found to be at 0.64 eV[2].

InN was also predicted to have remarkable electrical transport properties due to an extremely small electron effective mass at the CB bottom. But observation of them in real samples has to face the big issue of good InN sample growth. In fact transport properties are much more affected by defects than optical properties.

Maybe the most relevant consequence of the smaller value of the InN band gap is that its alloy system with GaN can cover the whole solar spectrum energy range, including the visible wavelengths and the IR region, as shown in Figure 2.1.

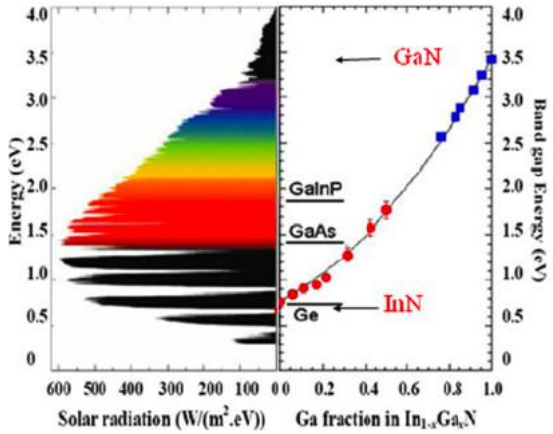

Figure 2.1. Band gap dependence of the InN-GaN alloy system as a function of Ga concentration, compared to the solar spectrum, the visible range and with the energy gap values of Ge, GaAs and GaInP.

Photovoltaic technology can profit from both the optical and transport properties of this alloy system to implement solar cells exceeding 50% efficiency. Several solutions can be explored taking advantage of its properties: multi-junction cells with 4 layers are predicted to exceed 50% efficiency, but a semiconductor having a gap around 2.4 eV is needed. InGaN can provide the right match. As an alternative, double-junction solar cells made by Si and InGaN with 45% of In may have power conversion efficiency higher than 31%, overcoming the homo-junction Si cells value. A recent review describes in detail all these opportunities[3].

The implementation of devices based on the alloy system of GaN and InN is very promising, but their reliability depends strongly on good quality samples

growth on the whole compositional range and on the control of extrinsic doping. These two steps are still a matter of fundamental research for InN and In-rich materials, while GaN technology is already mature and commercially available optoelectronic devices working from the UV to the green light wavelength are all based on GaN and Ga-rich heterostructures.

The following paragraphs give a brief introduction to the structure and growing techniques used in nitride research, focusing on the key parameters that make In-rich samples so hard to be grown. A survey of optical and electrical properties is also given.

2.1.1 Crystal structure[4]

Nitrides can crystallize in three different forms: the wurtzite (WZ), the zinc-blende (ZB) and the rock-salt (RS) structure, but at atmospheric pressure and room temperature their equilibrium form is the wurtzite. Wurtzite has a hexagonal unit cell defined by two lattice constants: *a*, for the basal plane, and *c*. The unit cell for GaN is shown in Figure 2.2 on the left. It is made by two cations (Ga) and two anions (N) and when replicated along the lattice directions it forms a crystal made by hexagonal mono-atomic planes stacked along the (0001) direction.

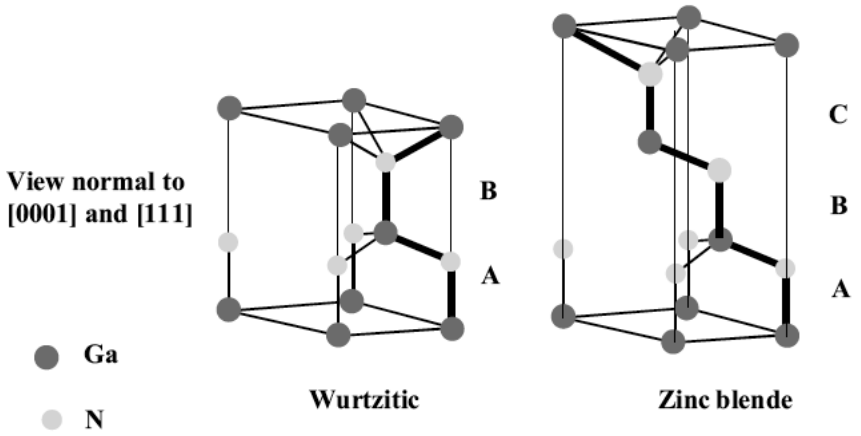

Figure 2.2. Wurtzite structure of GaN with the c axis directed along the z-axis and zinc-blende structure oriented with the (111) direction along z. The different stacking sequence is underlined by capitol letters on the right side of the cells.

In Figure 2.2 on the right it is also shown the ZB structure when observed with the (111) direction along the *z*-axis. It forms mono-atomic hexagonal planes stacked along (111) direction like in the WZ case, but the stacking is different, as can be seen by looking at Figure 2.2: in ZB it is AaBbCc, while in WZ AaBbAaBb, where capital letter stands for cation and lowercase letter for anion. The result is

that in both structures cation and anions have the same tetragonal nearest neighbours environment, but due to the different second nearest neighbours disposition, the ZB is cubic and isotropic, while the WZ is hexagonal and is anisotropic.

The WZ structure is defined by three parameters: the lattice constants *a* and *c*, usually reported as *a* and *c/a*, and the parameter *u* that defines the relative displacement along the *c* direction of anion and cation in unit cell. The inter-atomic distance along *c* is therefore obtained by *c* times *u*. In an ideal WZ, represented by touching hard spheres, the value of *c/a* is 1.633 and for *u* it is 0.375. Nitrides are obviously not ideal WZ, their parameters are listed in Table 2.1 where experimental values are compared with the ideal ones.

	GaN		AlN		InN	
	Ideal	**Exp**	**Ideal**	**Exp**	**Ideal**	**Exp**
u	0.375	0.377	0.375	0.382	0.375	0.379
a (Å)	3.199	3.199	3.110	3.110	3.585	3.585
c/a	1.633	1.634	1.633	1.606	1.633	1.618
b (u*c)	1.959	1.971	1.904	1.907	2.195	2.200
b_1	1.959	1.955	1.904	1.890	2.195	2.185

Table 2.1. Ideal and experimental crystal structure values for nitrides[5]. The parameter b and b1 are the cation-anion distances along the c axis and off the c axis respectively.

Of particular importance is the comparison between ideal and experimental *c/a*: GaN it is almost perfect, while InN and AlN unit cells are compressed. The result is a different cation-anion distance along the *c*-axis and in a slightly distorted tetrahedral environment.

In Table 2.1 the ideal and experimental inter-atomic distances for the nearest neighbours are also listed. The cation-anion distance along the *c* axis is called *b*, while the three other bond lengths are given by b_1. Clearly nitrides have very different inter-atomic distances and this has a remarkable relevance for alloy deposition, since it causes strong lattice strain that leads to phase separation. It is in fact known that due to the difference in inter-atomic distances, nitride alloys present a solid phase miscibility gap.

2.1.2 Deposition methods

The growth of nitrides poses a real challenge. Two are the main issues that make this task so hard: the lack of lattice- and thermal-matched substrates and the high equilibrium N_2 pressure needed to incorporate stoichiometric amounts of N into epilayers.

Nitrides can be grown only by epitaxial methods, because temperatures required for bulk-crystal growth prevent N incorporation. Substrates are therefore necessary and lattice and thermal mismatch with the epitaxial material affect strongly films quality. Lattice mismatch induces dislocations that spread along the growth direction, usually the c axis, while thermal mismatch can result in cracking during the cooling procedure. Such defects are detrimental for device performances: they can act as non-radiative recombination centres (NRCs), degrading the optical properties, and scattering centres for free carriers, limiting their lifetime and therefore degrading electrical properties. One of the parameter used to indicate the maturity of a specific semiconductor technology is exactly the dislocation density: for Si and GaAs it has reached values around 10^2-10^3 cm^{-3}, while for nitrides it still ranges between 10^8-10^{10} cm^{-3}.

Nitrides are usually grown on sapphire because it is easy to clean, it has hexagonal structure and can resist to the high temperatures required in growth processes. Also SiC and AlN are used, the first for its high thermal conductivity and the latter because of better lattice match.

It has been proved that defects due to lattice mismatch can be strongly decreased by nitridation of the substrate or by the deposition of a buffer layer prior to epitaxy. Both solutions release part of the lattice mismatch and create centres of nucleation that favour the lateral growth of epitaxial film. Nitridation consists on irradiating the substrate with N_2 to form a surface layer of AlN. The deposition of a buffer layer, instead, is accomplished at low temperature to form amorphous films, usually of AlN or GaN. With the foregoing deposition of a buffer layer, the growth becomes a two-stage process that brings to better quality top-most layers in terms of mobility, intrinsic carrier concentration and defect density.

The problem of stoichiometric incorporation of N is caused by the high N_2 partial pressure needed to maintain nitride in thermodynamic equilibrium. Figure 2.3 shows the curve that separates the space of parameters where the molecular constituents are stable over the solid phase from the region where the solid nitride is stable. The parameter is the N_2 partial pressure as a function of temperature.

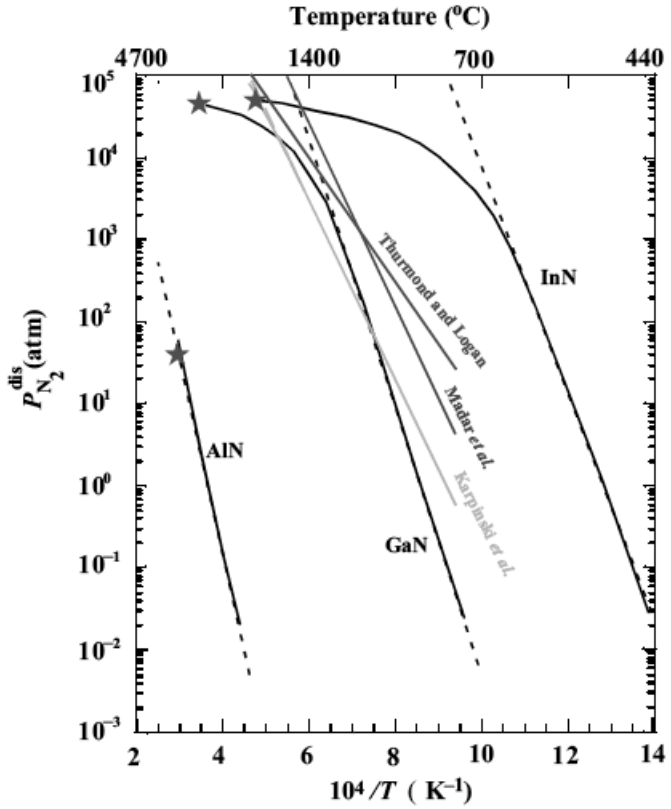

Figure 2.3. Graph of the equilibrium N_2 pressure as a function of temperature. In the region over of the curves, the solid phase of the nitride is stable over the molecular constituents. Under the curve, instead, nitrides dissociate[4].

The solid phase is stable in the upper side of the curve, therefore for higher temperatures, N_2 partial pressure must be increased to maintain stability of the nitride. This means also that N is more easily desorbed than the metal species and if parameters are not optimized, high concentration of N vacancies can be incorporated into the film. This is especially true for GaN and InN, whose partial pressure is a steeply increasing function of temperature. These materials both suffer from high *n* background carrier concentration in as grown samples and N vacancies are claimed to be the main cause for it. High N_2 partial pressure is the main obstacle in nitride deposition and the success of a specific growth method stands in its ability to settle this issue. InN is the test material because it's the hardest to grow. Today GaN technology is mature while growth of good quality InN films and In-rich materials is still a matter of fundamental research.

The most used techniques in nitride deposition are Metal-Organic Chemical Vapour Deposition (MOCVD) and Molecular Beam Epitaxy (MBE). Even if the

dynamics governing those methods is different, the key parameters are the same. The most relevant is the temperature of the substrate, followed by the ratio of N precursor over metal precursors, called the V/III ratio, and the flow rate at which the precursors are injected into the chamber. The region of the parameter-space where growth is feasible can be really narrow, as in the case of InN, and research has struggled in last decades to explore it and find the optimal conditions.

In MOCVD the nitride growth is the result of a chemical reaction that takes place on the surface of the substrate among the organic precursors. The reactants are injected into the growth chamber where they undergo thermal dissociation at the substrate surface, held at high temperature. Then the radicals sticked on the surface react, forming the nitride as a product together with side gaseous species. Commonly used precursors for the metal species are trimethylgallium, TMG ($(CH_3)_3Ga$), trimethylindium, TMI ($(CH_3)_3In$), and trimethylalluminium, TMA ($(CH_3)_3Al$), while the typical Nitrogen source is NH_3. Ammonia is chemically very stable, therefore its cracking needs high temperatures. When possible, growth is performed above 1000 °C since it means efficient Ammonia cracking and higher mobility of radicals on the surface, that contribute to a better crystal quality. For InN this implies prohibitive partial pressure of N_2 to stay on the right side of the equilibrium curve of the phase diagram and, furthermore, InN decomposition starts at temperatures as low as 650 °C. Lower substrate temperatures are therefore compulsory, meaning a low efficient cracking of NH_3 and the risk of having high concentration of N vacancies. To circumvent this obstacle, two ways are available: changing NH_3 with a less stable precursor so to have an efficient cracking at lower temperature or keeping the ratio of NH_3 over the metal precursor high to compensate for the inefficient cracking. The latter has proved to be the best choice, as no N precursor is available with the same level of purity of NH_3.

When growth is performed at low temperature, a high V/III ratio compensates for the scarcity of active N, but the crystal quality becomes worst because the mobility on the surface is reduced and the migration of species to step edges is too slow to permit an ordered process. To improve the crystal quality at low temperature, growth rate has to be drastically decreased in order to give time to the deposited species to migrate along the surface.

To summarise, in MOCVD growth performed at lower temperatures has to use high V/III ratios to supply more active N. At the same time the growth rate has to be drastically reduced to increase the migration of the nitride formed on

the surface to step edges, providing an ordered growth process and therefore a better crystal quality.

Nitrides can also be grown at higher temperatures and InN is not an exception. Obviously under those unfavourable conditions, parameters have to be carefully tuned to prevent decomposition. The experimental evidence is that with higher temperature In droplets form on the surface as a consequence of N desorption. High V/III ratio has been tried to supply more N to the film, but it results in a degradation of the growth process due to the increasing pressure of side gases like H_2. Higher growth rates instead are useful to trap N before desorption occurs, therefore the flow of precursors can be increased maintaining a low V/III ratio.

In MOCVD the range of temperature compatible with good quality InN films is around 500° - 650°C[6], going further down with temperature leads to bad quality crystals or to unacceptable growth rates. Nitrides MBE instead can be performed also at 400 °C and at first it was the possibility to stay lower in temperature that let this technique stand out in the field of nitrides.

Molecular Beam Epitaxy (MBE) has for long time been considered a least efficient method for epitaxial growth than MOCVD. This is because of the smaller growth rate and because MOCVD can be easily industrialised. But in the field of nitrides, MBE played a pivotal role in pushing forward the quality of InN films and today is largely used in the research for the improvement of growth methods of In-rich alloys. What makes this technique so suitable for nitride growth is the efficient N sources that can replace the classical NH_3 flow. Classical MBE uses N_2 or NH_3 flows for supplying N and evaporation of metals from Knudsen cells for the cation species. Among the alternative N sources, the radio frequency (RF) plasma source is one of the more efficient. In Plasma Assisted MBE (PAMBE), a large amount of active atomic Nitrogen is injected into the chamber and is ready to be incorporated into the epilayer without the need of molecule dissociation. As a consequence PAMBE can be performed at lower temperatures than MOCVD and for InN the optimal range is around 450° - 550°C[6].

MBE has the great merit of having provided good quality films of InN in the early 2000s with much reduced free electron concentrations ($<10^{18}$ cm^{-3}) and high electron mobilities (>2000 cm^2/Vs). Those high quality samples have been essential for progress in understanding the properties of the material and in particular for the determination of its actual band gap[7].

The mechanism leading to epitaxial growth in MBE is different from MOCVD. It isn't ruled by thermodynamic equilibrium, but by kinematic processes[4]: the atomic species released by the sources undergo various processes once they have reached the substrate surface. They can be adsorbed and subsequently desorbed, they can diffuse along the surface and be incorporated or be released after decomposition, as shown in Figure 2.4. Absorption means that an impinging atom from the molecular stream sticks to the surface. It then can be incorporated, that means it occupies a lattice site position and forms bonds with the surrounding atoms, or it can be desorbed and leave the substrate because of thermal vibration.

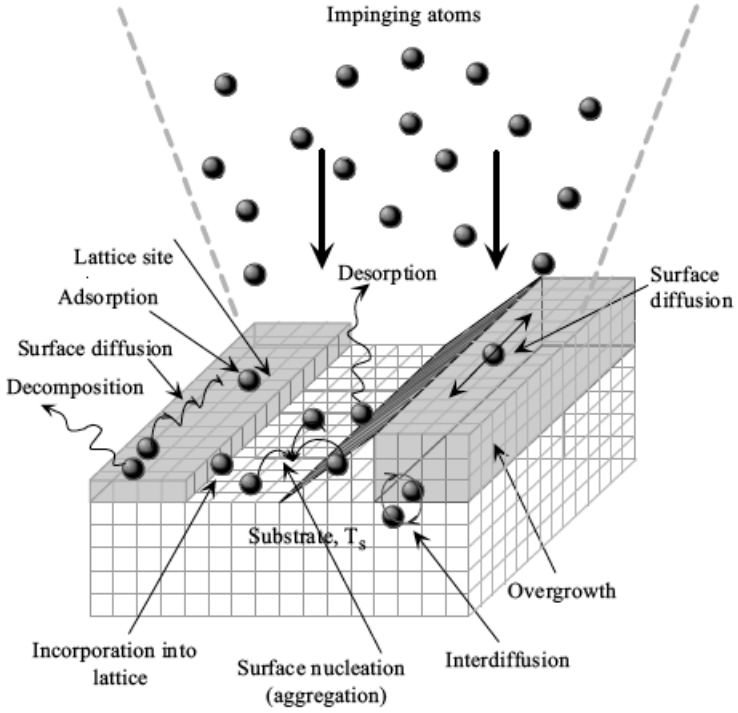

Figure 2.4. Scheme of dynamic processes that take place during MBE growth[4].

The substrate is held at high temperature to favour surface diffusion that helps the adsorbed atoms to move on the substrate and find a minimum energy position. But the high temperature can also induce decomposition through the breaking of bonds between the edge atoms and their neighbours. The substrate temperature is again the most relevant parameter, like in MOCVD. It determines the growth rate, the surface diffusion and the decomposition rate too. MBE performed at low temperature doesn't affect the amount of active N available, but since desorption of N occurs before desorption of In, also in MBE large V/III

ratios are used to prevent the formation of In droplets and as surface diffusion is less efficient at low temperature, the growth has to be slowed down to give the adsorbed species more time to be incorporated. In conclusion, the trend of parameters tuning is the same for MBE and MOCVD, but the values and the ranges are very different.

Today the recipe to grow good quality InN films both with MOCVD and MBE is quite established and samples with concentration carrier of some units of 10^{17} cm^{-3} and mobilities over 2000 cm^2/Vs have been grown. GaN on the other hand has a mature technology, where *p*- and *n*-doping and heterostructure epitaxy for device production are easily accomplished.

What is still challenging is the alloying of nitrides with large amount of In. The capability of alloying nitrides in the full compositional range is of fundamental importance to develop devices matched with the solar spectrum or emitters in the visible light. Figure 2.5 shows the energy gap of nitride alloys as a function of lattice constant that according to Vegard's law is a linear function of cation concentrations.

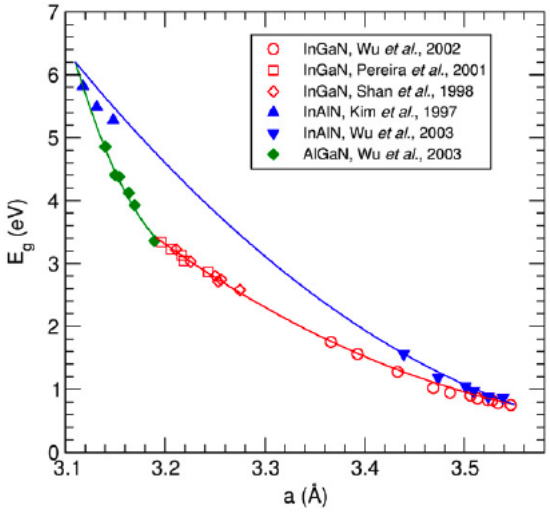

Figure 2.5. Measured band gap values for the III-nitride alloy system. Lines are fit to the standard equation for the band gap dependence on cation concentrations[8].

Growth of InGaN with low In content is easily performed and already implemented in optoelectronic industry, since most of UV-blue emitting devices are based on active layers with Ga-rich heterostructures.

The side of In-rich materials on the contrary is particularly challenging. Optimized temperatures for GaN growth are usually over 1000 °C and fall beyond the

decomposition temperature of InN. Growing at low temperature, even if prevents InN decomposition, will always favour Ga incorporation over In, as can be seen by the phase diagram, and in general degrade crystal quality. Furthermore, InN and GaN have different equilibrium inter-atomic distances, leading to considerable internal strain in the epitaxial film. This results in a solid-phase miscibility gap that favours phase separation and the formation of In micro grains that act as non-radiative recombination centres, degrading the emission properties of material[3,4,6].

Homogeneity and low defect density are of capital importance for good emission and transport properties. Out-of-equilibrium conditions have to be used to obtain In-rich materials and avoid phase separation. Usually low temperature favours high In incorporation, but results also in high resistivity. V/III ratio exceeding 20.000 are necessary and low growth rates. Despite all those obstacles, today samples of InGaN in the full compositional range have been obtained both with MOCVD and MBE[9,10]. They show good optical properties, while transport properties are still poor, especially for samples grown at low temperature. Optoelectronic devices can be based on thin active layers where the confinement of carriers enhances the band-to-band radiative recombination and therefore the transport properties are less important. Emission in the three fundamental colours has in fact demonstrated in LED with InGaN based active region, as shown in Figure 2.6[11].

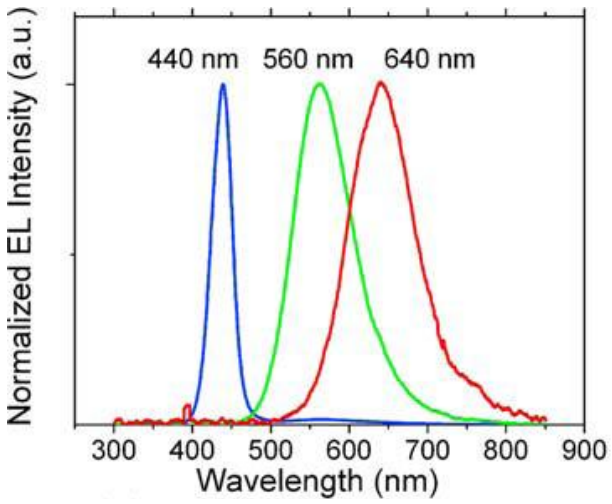

Figure 2.6. Electroluminescence spectra of InGaN/GaN MQW LEDs with In concentrations of 0.18, 0.41 and 0.46 for blue, green and red light respectively[11].

For photovoltaic application, instead, it is fundamental to have good electrical properties to collect photogenerated carriers and thicker layers are

needed to maximise the absorption. This is why InGaN implementation in PV is just at its first step[3].

2.1.3 *p*-doping

Being able to intentionally dope a semiconductor is a necessary step for the development of technology based on it. Almost every device, in fact, needs a *p-n* junction to be realised. Nitrides are particularly difficult to be intentionally *p*-doped, because they tend to grow with high unintentional *n*-doping. The origin of the background electron concentration has been investigated in depth, in particular for the GaN case, whose technology is older. O, H and Si impurities has been proposed as potential donors, but their concentrations has been measured and found too low to account for the effect[7].

N vacancies (V_N), instead, can be incorporated in large amounts in GaN and InN, due to the high equilibrium N_2 partial pressure. V_N is claimed to act as a double donor; in fact a missing N leaves behind 3 unbound Ga electrons that can be promoted in the conduction band, giving rise to intrinsic *n*-doping[6].

Independently from the strict cause of the unintentional doping, one thing is sure: high quality films with low defect densities are the first step towards intentional doping control. In the GaN case only after its growing technology was quite mature, good results on *p*-type doping started to appear. The major breakthrough occurred between the '80s and '90s, when Amano[12] obtained *p*-type conduction from Mg-doped films. They found that irradiation of the sample with a low energy electron beam activates the Mg impurities otherwise passivated. Nakamura then obtained *p*-type conduction and low resistivity in Mg-doped GaN irradiated and post-annealed in N_2 atmosphere[13]. Those discoveries led quickly to the development of efficient devices based on GaN that soon reached the market.

InN technology is not yet sufficiently mature and efficient *p*-doping is not yet available. However, Mg is the best candidate and *p*-type conduction has been measured for the first time in 2006[14]. It has been calculated that Mg activation energy in InN should be lower than in GaN, but incorporation of Mg tends to form compensated and high resistive materials. Quality of samples is surely the strongest limiting issue, since the source of unintentional *n*-doping is the high densities of native defects. A further complication is the presence of a degenerate *n*-doped surface layer that affect the reliability of Hall effect measurements, sensitive only to the surface electrical properties. This means that thicker samples

are needed to make measurements less sensitive to the surface and probe the bulk for eventual *p*-type conduction.

2.1.4 Optical and electrical properties

Interest in nitrides was at first motivated by their promising optical properties. They have in fact direct band gaps, ranging from 6.4 eV for AlN to 0.64 eV for InN, allowing the realization of optoelectronic devices in a wide energy range with their alloys.

The early stage of research on nitrides focused on the emission properties of GaN to realise light emitters in the blue range, that was the last missing fundamental colour to be implemented in LED devices. Blue emission was first observed in 1971 by Pankove[15] in a diode with a GaN-based active area. Much effort since then was spent to produce better quality samples and to obtain *p*-type doping, till in 1993 the first efficient blue LED was realised, based on a GaN diode with Ga-rich InGaN QWs in the active area. The great success of the blue LED induced a steep increase in research on InN and InGaN to push down the wavelength of emitted light. Research faced then the extreme difficulty task of depositing samples of InN and In-rich InGaN with good structural, optical and electrical properties.

When interest in InN growth and characterisation started, samples available were polycrystalline and grown by sputtering methods. Absorption measurements the edge was found around 1.9 eV, but surprisingly no PL was detected, an unusual behaviour for nitrides. The band gap was assumed to be 1.9 eV, until improvements in MOCVD allowed the deposition of InGaN samples on the Ga-rich side of the alloy system. The characterization showed an exceptional lowering of the gap, that fell down below 2 eV for 0.5 In content[16]. To explain the effect within the 1.9 eV band gap hypothesis, a giant and concentration dependent band gap bowing would be needed, a quite unusual behaviour for semiconductors. This was the first hint of a lower band gap value for InN. A major breakthrough came around 2000, when improved quality single crystal InN films grown by MBE started to be available thanks to alternative active N sources, like RF plasma sources. In those samples intrinsic carrier concentration was very small and measured absorption edges starts to decrease towards 1 eV[8]. More important, for the first time PL was observed, giving the proof that the fundamental gap was being investigated this time. Previously grown samples were affected by high background carrier concentration that caused conduction band filling and blue-

shift of the absorption edge, the so called Burstein-Moss effect, schematically shown in Figure 2.7. Emission is still possible even when the Fermi level falls in the CB, but is intrinsically broadened.

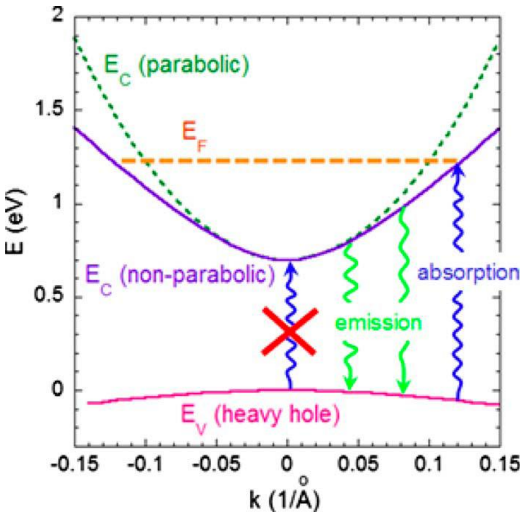

Figure 2.7. Sketch of the Burstein-Moss effect[7]. Band filling due to intrinsic carriers forbids absorption at the fundamental gap energy and causes absorption edge blue-shift. The effect of non-parabolicity of CB is also shown and the Fermi level corresponds to a concentration of free carriers of 10^{20} cm^{-3}.

The InN band gap is today known to be 0.64 eV[2], even if the debate is not over yet, as some old data on sputtering grown samples remains unexplained[17]. Absorption and PL by a state-of-the-art InN film is shown in Figure 2.8.

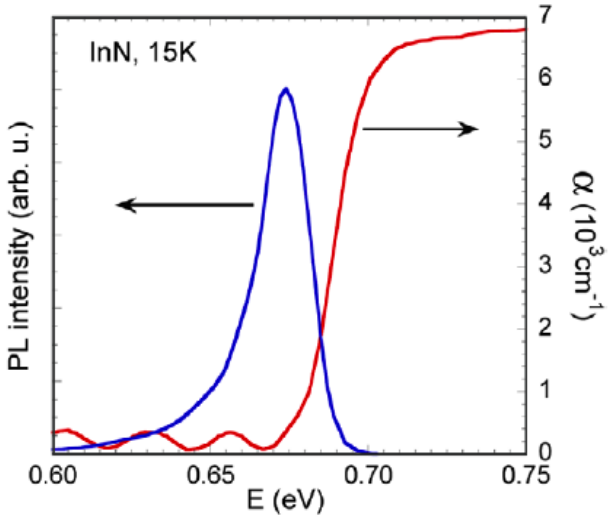

Figure 2.8. Photoluminescence and absorption measured on a state-of-the-art InN films grown by MBE[2].

Turning to optical properties of InGaN films, despite the large density defect and the still not excellent quality, absorption and PL have been measured over the whole In concentration range. Figure 2.9 shows on the left a plot with some absorption and PL spectra taken on samples with In concentration *x* ranging between $0.37<x<1$ and on the right a summary of experimental data where PL peak energy and absorption edge energy versus In content are plotted. The trend is underlined by a fit to the standard formula for band gap energy variation.

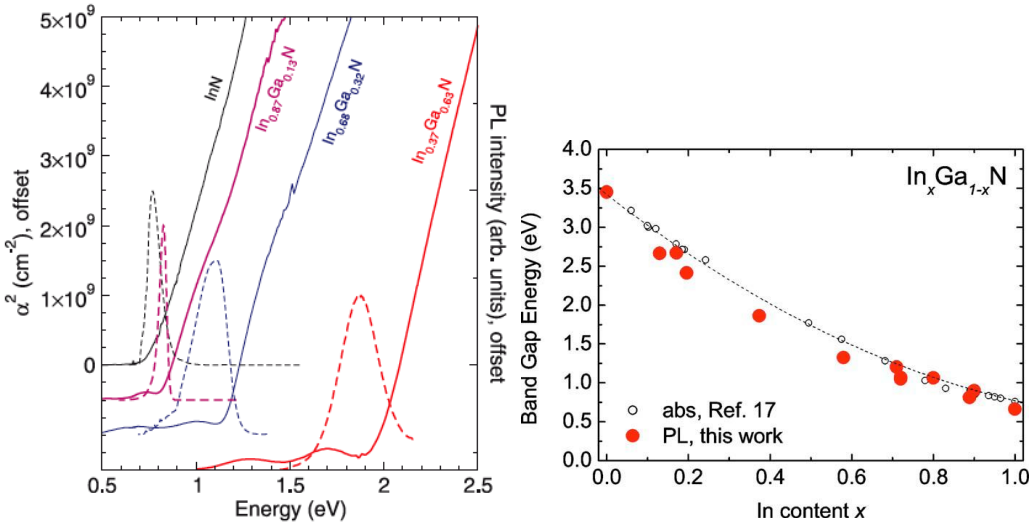

Figure 2.9. Left: absorption (solid line) and PL (dotted lines) spectra from a series of InGaN films showing the correspondence of the PL peak with the optical absorption edge at each concentration[8]*. Right: absorption edge and PL peak plotted as a function of the In content*[7]*.*

As mentioned before, the optical properties of nitrides were responsible for the initial interest on this field. However, also their transport properties deserve attention as nitrides were predicted to have small values of the effective electron mass, m^*/m_0, at the CB bottom and high mobility and drift velocities of carriers, very promising properties for photovoltaic applications, since carriers transport is fundamental for device efficiency[3]. Experimental and theoretical values for electron effective mass are plotted in Figure 2.10: measured values cover a vast range because of the different intrinsic electron concentrations of samples probed. Electrons fill the CB bottom and place the Fermi level inside the CB. When testing the transport properties for effective mass estimation, the electrons participating to the transport are limited to a portion in the vicinity of the Fermi level, therefore the obtained parameters are referred to this zone of the dispertion diagram. The blue curve in Figure 2.10 is the theoretical trend of the electron

effective mass according to the band structure calculated with the *k*·p model. The extrapolated value at non-degenerate carrier concentration is around 0.07, to be compared with 0.32 and 0.20[18] for AlN and GaN.

The extraordinary low value of InN effective mass has been predicted to give mobilities as high as 4.400 cm^2/Vs at room temperature[6], but the observation of those extraordinary electrical properties is made difficult by the low quality of samples. Large defect densities, in fact, affects transport properties more seriously than it does for optical properties. PL and absorption are quite good, while carrier lifetime is tremendously degraded by the limited crystal quality. With progress in growth, better transport properties were measured and the trend of higher mobility coming up in samples with lower background electron concentration was observed.

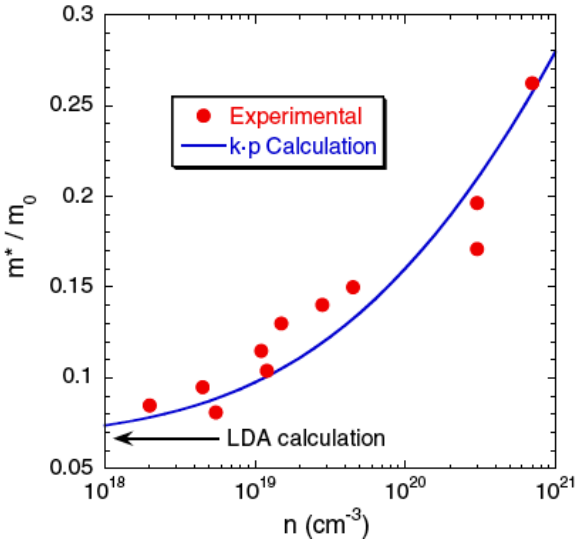

Figure 2.10. InN electron effective mass as a function of electron concentration. Experimental data are taken from [19], while the theoretical curve is based on Kane's model described in 8 and the arrow indicates the value obtained by a recent LDA calculation[20].

The best values obtained on MOCVD InN are 730 cm^2/Vs for the mobility and 5.8 10^{18} cm^{-3} for carrier concentration[21]. While MBE state-of-the-art samples[22] have mobilities exciding 2.000 cm^2/Vs and electron concentrations of about 3 10^{17} cm^{-3}.

The situation is even more critical for InGaN, because of the poor quality of the films: mobilities, carrier concentrations and lifetimes are still poor due to the high density of scattering centres. Thicker layers, needed to maximise absorption for PV applications, are more defective and therefore with worst transport properties. Research is working hard to improve those properties, but for the

moment solar cells based on InGaN are still a promising application more than actual devices[3].

2.2 Dilute nitrides[23]

In the early '90s alloying of GaAs with wide band gap nitrides started to be explored with the aim of filling the gap and cover the solar spectrum range. When samples of GaAs with small amounts of N grown by MBE became available, researchers faced the unexpected result of a reduction of the band gap upon alloying instead of an enlargement. This extraordinary observation was first reported in 1992 by Weyers[24] and subsequently by Kondow[25]. Since then, a great deal of work has been done to account for properties shown by those compounds, in particular for the technological interest they represent for telecommunication applications. In fact the giant band gap bowing upon alloying with N can bring the direct band gap of GaAs to 1.3-1.5 μm. This wavelength window is used in telecommunications because of the low dissipation at fibre-air interfaces and before the advent of dilute nitrides was covered only by the alloy system of InGaAsP grown on InP. Figure 2.11 shows the dependence of band gap energy on lattice constant for alloy systems in the telecommunication wavelength range.

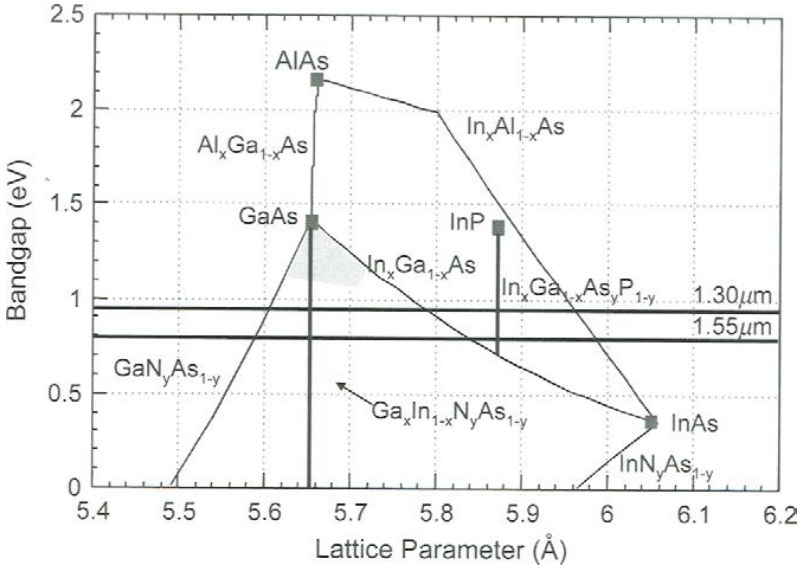

Figure 2.11. Scheme of band gap dependence on lattice constant of the alloy systems able to cover the telecommunication frequency range[23].

In Figure 2.11 it is seen how the introduction of small percentage of In can relax the mismatch between dilute GaAsN and GaAs. This actually opens the way

to GaAs integrated emitters in the telecommunication wavelength that before were a domain of InP-matched InGaAsP. The possibility of using GaAs instead of InP has all the advantages offered by its very mature technology.

Methods for the preparation of those materials were rapidly developed and characterisation started to unravel several properties that needed a physical explanation. Many theoretical models were applied to account for the non-linear variation of semiconductor properties in dilute nitrides. A clear picture emerged, based on the interplay between N-localized states, GaAs host states at the bottom of the CB and cluster states (CS) originating by the random distribution of N atoms on the lattice.

2.2.1 Growth methods

Dilute GaAsN (InGaAsN) is obtained by including small amounts of N into GaAs (InGaAs). The deposition is not easy to perform for several reasons: the binary compounds have different crystal structures, ZB for GaAs and WZ for GaN, and competing anions have different ionic radii (0.74 for As Å and 1.2 Å for N) and electronegativity. These characteristics result in a miscibility gap and in a low solubility of N in GaAs. As a consequence growth methods are forced to work in metastable conditions to incorporate the amount of N needed to tune the band gap at the desired energy. The most successful techniques for dilute nitrides deposition are once again MOCVD and MBE, with a predominance of MBE because metastable conditions are easier to maintain.

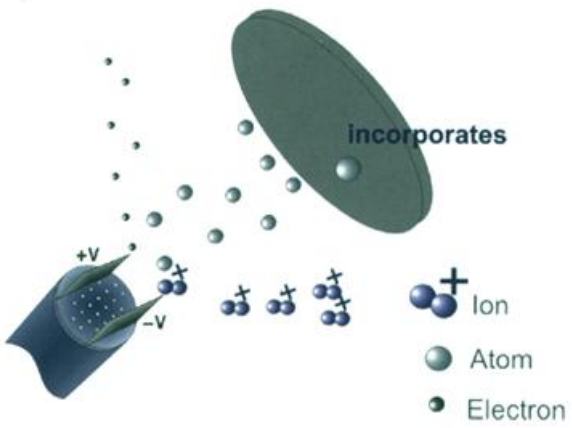

Figure 2.12. Schematic diagram of N plasma source and different species which are created (N^{2+} ion, N atom, electron. Biased plates at the output deflect N^{2+} ions and electrons such that only atomic N reaches the surface.

MBE growth of dilute nitrides is usually performed with a RF plasma N source that provides large amounts of active atomic N without the need to thermally dissociate any molecular compound. The quality of the film depends then on plasma stability and ion damage. The latter is solved by using biased plates (Figure 2.12) to deflect electrons and ions and prevent the bombardment of the sample surface by ionic species.

The critical parameters in MBE growth of dilute nitrides are temperature of the substrate and Ga-flow rate. The temperature of the substrate determines the growth dynamics: low temperatures favour a layer-by-layer growth giving smoother samples, while at higher temperature a 3D dynamic is favoured. Lower temperatures ranging between 430-470°C are therefore preferred. N incorporation, instead, depends exclusively on Ga-flow rates: at higher Ga-flow rates, the growth proceeds rapidly and the incorporation of N is unfavoured because of the limited amount of active N provided by the source. A lower Ga-flux on the other hand gives time to all the active N produced to stick on the substrate and be incorporated. N incorporation has been found to improve considerably with introduction of Sb in the growth process. It helps the active atomic N delivered by the RF plasma source to stick on the surface. Improvements around 50%-60% were found.

MOCVD of dilute nitrides is less efficient than MBE, but it has greatly improved and the quality of MOCVD grown films has approached that of MBE samples. Critical parameters for crystal growth are substrate temperature and growth rate. Temperatures lower than the ones used in GaAs growth (above 650°C) are preferred because the rate of desorption of N-containing species sticked on the surface are minimised and the amount of N incorporated increases. Figure 2.13 shows the N content as a function of temperature for two different V/III ratios.

The low temperature brings about the issue of which N precursor to use: it has to have high vapour pressure at room temperature, efficient dissociation at low temperatures and high purity. Ammonia is too stable, therefore mostly used precursors are chosen from the family of hydrazine or from its methyl-substituted compounds, like mono- or di-methylhydrazine (MMHy, DMHy). Also NF_3 has been tried and seems even more efficient.

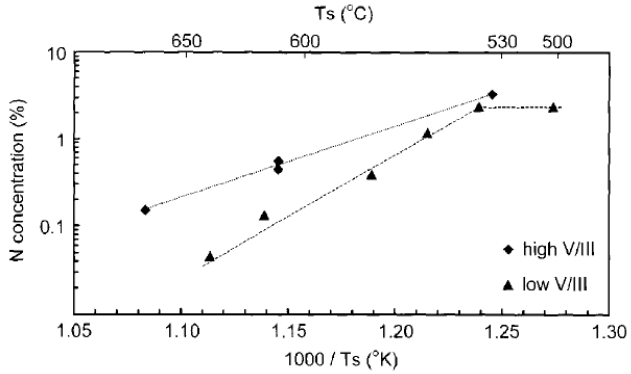

Figure 2.13. Temperature dependence of nitrogen incorporation in GaAsN grown by atmospheric pressure MOCVD using low and high V/III ratio. Ref. 23, chapter 2.

N incorporation depends mostly by the growth rate: a higher growth rate favours larger amounts of N because it is incorporated before desorption takes place. On the other hand, lower growth rate has been demonstrated to improve PL properties, because H is desorbed and passivation of N is avoided. Figure 2.14 shows the dependence of N incorporation on growth rate and the better quality of PL for samples grown at different rates.

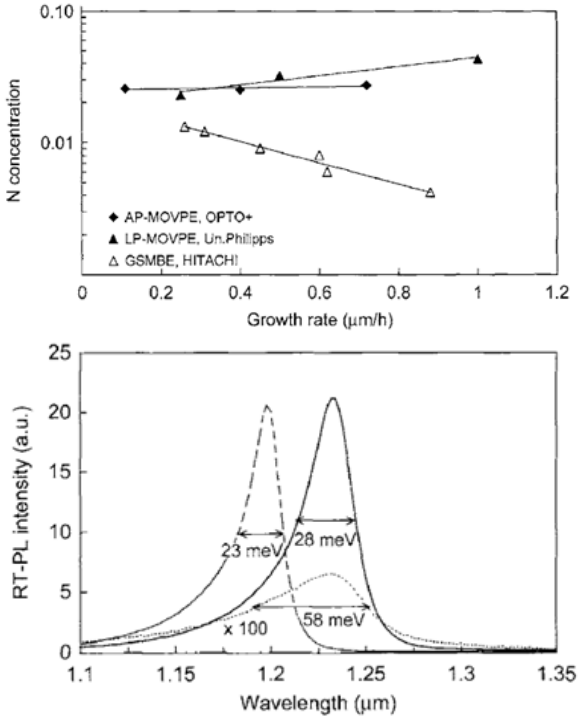

Figure 2.14. Top: dependence of N concentration in GaAsN on the growth rate for MOCVD- and MBE-grown layers. Bottom: RT-PL spectra of GaInAsN/GaAs QWs grown at 0.15 µm/h (bold line) compared with 1 µm/h (dotted line). The PL spectrum of GaInAs/GaAs QW (dashed line) is also shown as a reference[26].

2.2.2 Nitrogen effect on band structure

Theoretical models for alloy semiconductors usually explain the properties shown by the materials within the Virtual Crystal Approximation (VCA), that calculates alloys properties from a crystal potential V(x) expressed by a linear interpolation of those of the binary constituents.

Dilute GaAsN and lattice-matched InGaAsN deviate strongly from the predictions of the VCA, showing a giant band gap lowering of GaAs (1.4 eV) instead of the expected increase towards the larger value of GaN band gap. The failure of the VCA is connected to the large difference between atomic radii and electronegativity of As and N. In such cases, even though the substitutional atom is isovalent, it introduces a strong perturbation on the host system, giving rise to unexpected effects. Figure 2.15 shows the dependence of GaAsN band gap energy on N concentration compared with the linear dependence predicted by the VCA theory.

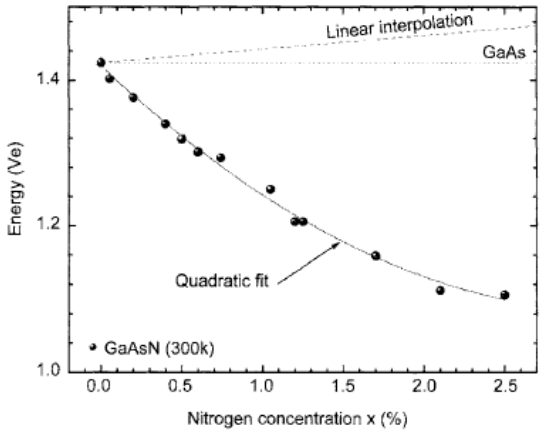

Figure 2.15. Bandgap of GaAsN as a function of Nitrogen concentration. Ref. 23, chapret 6.

To explain the behaviour of dilute nitrides, many theoretical models have been proposed. The test of their validity is the ability of describing the giant band gap bowing together with other experimentally observed characteristics. The most relevant are the pressure dependence of electronic levels and the variation of the electron effective mass upon alloying with N.

Photo reflectance measurements taken on samples with different N concentrations are shown in Figure 2.16. The GaAs spectrum shows two structures in the second derivative spectrum, the one labelled E_0 due to the transition from the VBM to the CBM, while the other, labelled $E_0+\Delta_0$ is the

transition from the spin-orbit split-off VB to the CBM. With the incorporation of N, the same two features are present and labelled E_- and $E_-+\Delta_0$. But together with them, a new feature labelled E_+, appears at higher energies and it is obviously related to energy levels introduced by N. The concentration dependence of those energy levels is seen from the PR data: E_- and $E_-+\Delta_0$ decrease upon N incorporation while E_+ increase in energy.

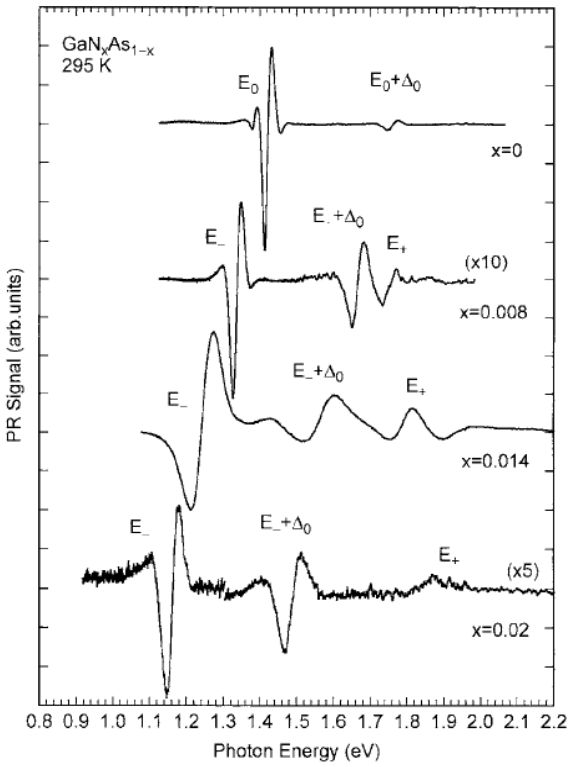

Figure 2.16. Photo Reflectance spectra of MOCVD-grown GaAsN samples with different N concentrations. Ref. 23, chapter 10.

The first model to successfully describe this trend was the band anti-crossing (BAC) model[27]. According to the BAC, N introduces a resonant level slightly above the CB edge of the host GaAs matrix. As the N concentration is increased, this resonant states start to form a band and interact with the CBM wave-function of GaAs. The effect of this interaction is shown in Figure 2.17: the two bands hybridize and result in two non-parabolic bands that repel each others, giving rise to a reduction of the band gap. Despite its simplicity, the BAC model accounts very well for the observed variation of E_- and E_+ and also for the increase of electron effective mass at very low N concentration, x<0.05%.

To explain experimental evidences like the electron effective mass dependence on N concentration, it is necessary to go beyond the simple BAC model. It gives very good results for energy level dependence on N concentraton, but it completly neglects the effect of random distribution of N atoms in the lattice. Integrating the BAC model with randomness effects gives better results and includes the observed dependence of effective mass.

The principle is that a small amount of N atoms distributed on a lattice, will create a statistical enseamble where isolated N, N-N pairs, N-N second-nearest neighbours and other configurations will be present with a certain probability. The electron state introduced by isolated N into the CB is highly localized, therefore these states will interact slightly with each other, leaving the very dilute nitride well described by the BAC model and any other isolated impurity model. With increased N content, a higher probability of finding structures like N-N pairs and other cluster configurations arises. Consideration of the energy levels introduced by those structure is then fundamental.

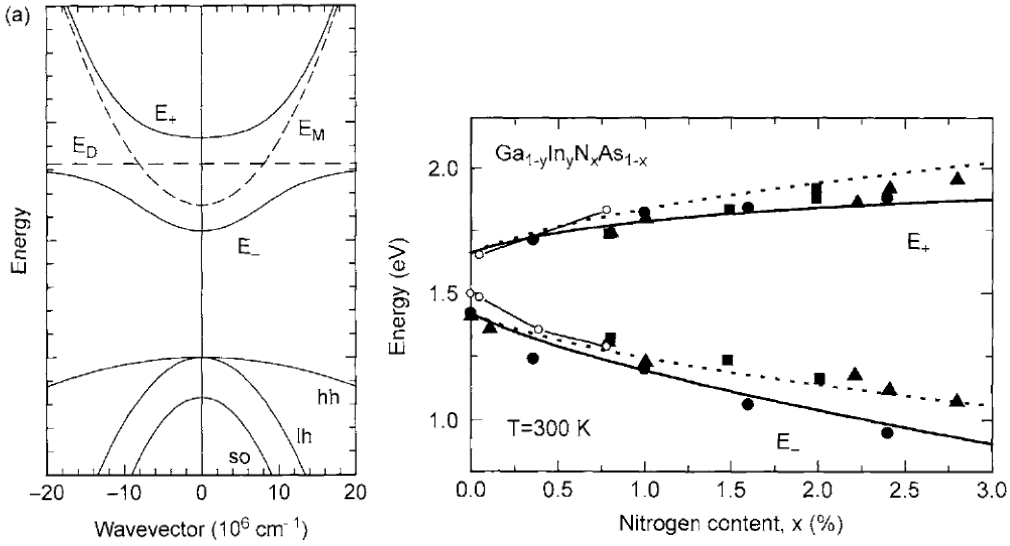

Figure 2.17. Left: sketch of BAC model for dilute GaAsN and InGaAsN. Dashed lines show the GaAs CB and the resonant state introduced by N above the CBM. Solid lines are the two split bands resulting by their interaction. Right: Experimental dependence of E_- and E_+ transitions on N composition and BAC model prediction for InGaAsN (In about 3 times N) (solid lines) and GaAsN (dotted lines). Ref. 23, chapter 10.

To account for randomness the most efficient approach is the super-cell model: large GaAs cells are built and then a small amount of As atoms are randomly chosen and substituted by N atoms. Simulating many randon

arrangement and comparing them with the supercell without N allows to associate energy levels to specific atomic configurations.

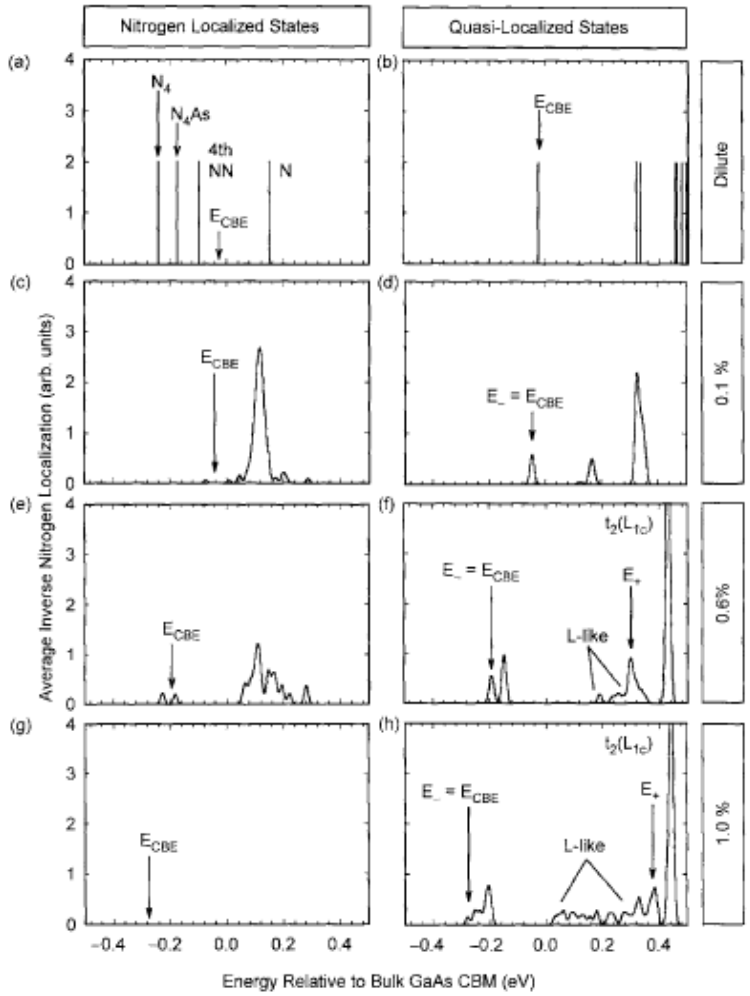

Figure 2.18. Calculated spectral dependence of average nitrogen localisation for (left) nitrogen localised CS and (right) quasi-localised perturbed host states of GaAsN for selected N compositions. The vertical arrows show the position of the alloy CBM. Ref. 23, chapter 12.

Comparison between the evolution of CBM with increased N content and energy location of N cluster states is shown in Figure 2.18: in the dilute limit the effect is a bowing of the band gap induced by simple interaction of the CBM with isolated N states. With increasing N the CBM shifts towards lower energies and starts to hybridize with CS. Going on with the alloying brings all the CS inside the CB and a pseudo-alloy regime is then restored. For N concentrations that bring the CBM in correspondence of CS energy levels, the spatial distribution of the

wave-function of the CB edge assumes a more localized nature due to hybridisation with CS. This increased localised character causes an increase of the effective mass, that can be estimated by the lost of Γ character of the CBM wave-function.

[1] S. Nakamura, T. Mukai and M. Senoh, *Appl. Phys. Lett.* ***64***, 1687 (1994).

[2] J. Wu, W. Walukiewicz, *J. Appl. Phys.* ***94***, 4457 (2003).

[3] A. G. Bhuiyan, K. Sugita, A. Hashimoto, A. Yamamoto, *IEEE J. of Photovoltaic* ***2***, 276 (2012).

[4] H. Morkoc, *Handbook of Nitride Semiconductors and Devices, Vol.1*, Wiley-VCH (2008), Weinheim.

[5] O. Ambacher, J. Majewski, C. Miskys, A. Link, M. Hermann, M. Eickhoff, M. Stutzmann, F. Bernardini, V. Fiorentini, V. Tilak, B. Schaff, L. F. Eastman, *J. Phys. Cond. Matt.* ***14***, 3399 (2002).

[6] A. G. Bhuiyan, A. Hashimoto, A. Yamamoto, *J. Appl. Phys.* ***94***, 2779 (2003).

[7] J. Wu, *J. Appl. Phys.* ***106***, 011101 (2009).

[8] W. Walukiewicz, J. W. Ager III, K. M. Yu, Z. Liliental-Weber, J. Wu, S. X. Li, R. E. Jones, J. D. Denlinger, *J. of Phys. D Appl. Phys.* ***39***, R83 (2006).

[9] K. Sasamoto, T. Hotta, K. Sugita, A. G. Bhuiyan, A. Hashimoto, A. Yamamoto, K. Kinoshita, Y. Kohji, *J. Cryst. Growth* ***318***, 492 (2011).

[10] E. Iliopoulos, A. Georgakilas, E. Dimakis, A. Adikimenakis, K. Tsagaraki, M. Androulidaki, N. T. Pelekanos, *Phys. Stat. Sol. A* ***203***, 102 (2006).

[11] T. Xu, A. Y. Nikiforov, R. France, C. Thomidis, A. Williams, T. D. Moustakas, *Phys. Status Solidi A* ***204***, 2098 (2007).

[12] H. Amano, M. Kito, K. Hiramatsu, I. Akasaki, *Japanease J. Appl. Phys.* ***28***, L2112 (1989).

[13] S. Nakamura, T. Mukai, M. Senoh, *Japanease J. Appl. Phys.* ***30***, L1998 (1991).

[14] R. E. Jones, K. M. Yu, S. X. Li, W. Walukiewicz, J. W. Ager, E. E. Haller, H. Lu, W. J. Schaff, *Phys. Rev. Lett.* ***96***, 125505 (2006).

[15] J. I. Pankove, E. A. Miller, J. E. Berkeyheiser, *J. Lumin.* ***4***, 63 (1971).

[16] T. Matsuoka, H. Tanaka, A. Katsui, *Int. Symp. On GaAs and Rel. Comp.* (Karuizawa, 1989), (*Ins. Phys. Conf. Series* ***106***, p. 141).

[17] K. S. A. Butcher, T. L. Tansley, *Superlat. Microstr.* ***38***, 1 (2005).

[18] I. Vurgaftman, J. R. Meyer, *J. Appl. Phys.* ***94***, 3675 (2003).

[19] J. Wu, W. Walukiewicz, W. Shan, K. M. Yu, J. W. Ager III, E. E. Haller, H. Lu, W. J. Schaff, *Phys. Rev. B* ***66***, 201403 (2002).

[20] P. Carrier, W. Su-Huai, *J. Appl. Phys.* ***97***, 033707 (2005).

[21] A. Yamamoto, T. Tanaka, K. Koide, A. Hashimoto, *Phys. Status Solidi A* ***194***, 510 (2002).

[22] H. Lu, W. J. Schaff, L. F. Eastman, J. Wu, W. Walukiewicz, D. C. Look, R. J. Molnar, *Mater. Res. Soc. Symp. Proc.* ***743***, L4.10.1 (2002).

[23] M. Henini, *Dilute Nitride Semiconductors*, Elsevier (2005).

[24] M. Weyers, M. Sato, H. Ando, *Japan. J. Appl. Phys. Part 2* ***31***, 853 (1992).

[25] M. Kondow, K. Uomi, A. Niwa, T. Kitatani, S. Watahiki, Y. Yazawa, *Japan. J. Appl. Phys.* ***35***, 1273 (1996).

[26] F. Alexandre, E. Gouardes, O. Gauthier-Lafaye, N. Bouadma, A. Vuong, B. Thedrez, *J. Mater. Sci. Mater. El.* ***13***, 633 (2002).

[27] W. Shan, W. Walukiewicz, J. W. Ager III, E. E. Haller, J. F. Geisz, D. J. Friedman, J. M. Olson, S. R. Kurtz, *Phys. Rev. Lett.* ***82***, 1221 (1999).

Chapter 3

A XANES study: H irradiation effects on InGaN

H is the most abundant element in nature and it is present in all growth techniques used in semiconductor technology; even in MBE, that is usually thought H-free, it desorbs from the stainless steel walls of the chamber and is present as a residual gas. When H is incorporated in a semiconductor material, it can severely affect its electrical characteristics with a variety of different behaviours. It can bind to donor or acceptor impurities and form a stable state with them, counteracting their role of providing free carriers and therefore passivating intentional doping. The reason why Mg impurity where unable to induce *p*-doping in GaN was exactly because of H-passivation that can be eliminated by a post-growth annealing[1]. But H can also behave as a source of carriers or as a deep impurity level, for example H^+ is stable when placed in a region of large electron charge density, like in the middle of a anion-cation bond. It this case H loses its electron and acts as a donor. On the contrary, when placed in a region poor of electronic charge density, it can capture a free electron and reach the electronic configuration of He, behaving like an electron trap. An overview on the role of H in semiconductors can be found in ref. [2].

In this chapter we present the interesting case of InGaN irradiated with a low-energy H beam to force H incorporation and at the same time limiting the irradiation induced structural damage. As discussed below, a systematic photoluminescence (PL) investigation on a series of InGaN samples covering the whole concentration range had shown that the optical properties are strongly modified by H incorporation. Specifically H causes a blue-shift of the PL peak that increases for increasing In content and H dose.

The results of this PL investigation are summarised in Figure 3.1. The left graph displays PL spectra taken on samples treated with the same dose of H (red dotted-line) superimposed on PL spectra recorded before H irradiation (black line). Spectra corresponding to samples with increasing In content are stacked from the top to the bottom and the growing blue-shift from zero for ~0.5 In content to ~0.3 for 0.82 In content is clearly visible. The inset on the bottom-right corner summarizes the SIMS results on deuterated samples and shows that the amount of D (for H the same result holds) incorporated in the material at equal irradiation dose increases with increasing In content. The graphs on the right display the dependence of the PL peak shift, ΔE_H, on the H-dose supplied to the material for four different samples and confirms the dependence of the effect on the amount of H incorporated.

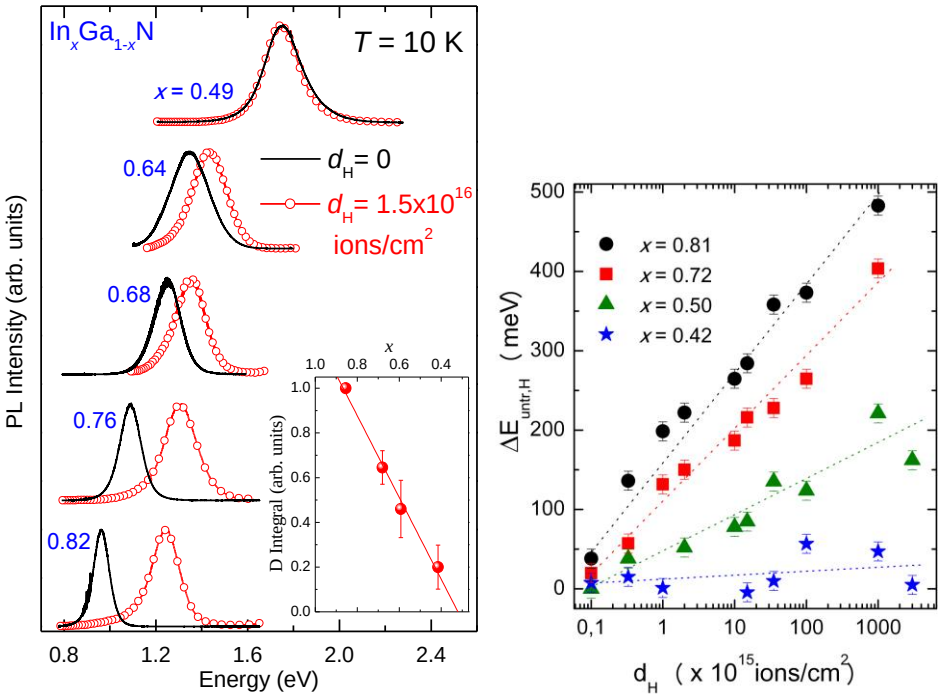

Figure 3.1. PL results on as grown and H irradiated InGaN films[3]. Left graph: PL spectra on as grown samples (black line) are superimposed on those taken on H-irradiated samples (red dotted-line) to show the blue-shift of the PL peak. The shift is larger for larger In content and vanishes for x=0.5. The inset on the bottom-right corner shows SIMS results on the total Deuterium content in a series of deuterated samples. The incorporation of Deuterium decreases with decreasing In concentration. Right graph: dependence of the blue-shift on H dose for four different samples; the blue-shift increases with increasing H dose in each of the four samples analysed.

The most probable cause for the peak shift is the filling of the CB operated by excess electrons introduced in the material through the formation of some kind of H-defect. As explained before, the arrangement of H atoms in the material is crucial for its electrical behaviour, therefore to understand why H induces such an effect, the micro-structural arrangement of H atoms in the material must be explored. But PL and in general optical characterisation is unable to furnish this kind of information, while x-ray techniques can selectively excite an atomic species and probe its local surroundings.

In this case EXAFS measurements at the In K-edge and XANES measurements at the N K-edge were used. In this chapter we present the detailed analysis of the N K-edge XANES spectra and explain how these measurements provide an insight into the micro-structural modifications induced by H incorporation in InGaN.

XANES spectra were acquired at three different polarisation geometries on a series of as-grown and H-irradiated samples covering the range of In concentration between 0.3 and 0.9. The analysis was divided in two parts: the first is a detailed study on the as-grown material performed using atom-specific *ab initio* simulations that help correlating the spectral features observed with the micro-structure of the alloy; in the second part the structural modifications induced by H complexes are investigated with the same atom-specific approach to determine which atomic arrangement can account for the observed spectral modifications. The micro-structures of both the as grown material and the H-defects were simulated by 96-atoms supercells obtained by DFT calculations, while *ab initio* simulations of XANES spectra were performed with the real space full multiple scattering code FEFF8.4.

3.1 Experimental data

3.1.1 Sample preparation and data acquisition

XANES spectra at the N K-edge were measured on a series of four $In_xGa_{1-x}N$ samples with In concentrations between $0.3<x<0.9$. Films were grown by plasma-assisted molecular beam epitaxy (PAMBE) on GaN/AlN/Sapphire(0001) substrates[4]; their thicknesses were large enough to avoid contributions in the XANES spectra from N atoms of the buffer layers and the substrate. SIMS measurements indicate a thickness between 300-500 nm for each sample. After deposition, the In content of each epilayer was determined by high resolution x-

ray diffraction (HRXRD), resulting in $x = 0.87, 0.61, 0.47, 0.36$. With the samples maintained at 300°C, the complete series was irradiated with a low energy H-beam (100 eV) provided by a Kaufman source and the H dose used was around $d_H = 1.2 \times 10^{-16}$ ions/cm^2. Optical measurements confirmed that H irradiation induces a blue-shift of the PL peak also on these thicker samples. A summary of the samples characteristics is given in the table below

	Sample	In content	H dose
1	733	0.87	1×10^{-16} ions/cm^2
2	419	0.61	1.2×10^{-16} ions/cm^2
3	402	0.47	1.2×10^{-16} ions/cm^2
4	423	0.36	1.2×10^{-16} ions/cm^2

Table 3.1. List of samples measured and their characteristics.

XANES measurements at the N K-edge were performed on the ALOISA beamline[5] at the ELETTRA synchrotron radiation facility, Trieste (Italy). Data were recorded in the fluorescence yield detection mode to guarantee the highest possible bulk sensitivity and the detector used was a windowless hyper-pure Ge diode placed at 90° from the incident beam direction to minimise the elastic scattering contribution. The fluorescence recorded was the N K_α emission and the incident photon energy calibration was performed with high accuracy by recording in parallel with each spectrum the signal from a N_2-filled ionization chamber and aligning the spectrum with the sharp transition to π^* molecular orbitals[5,6]. Each sample was measured in three different geometries, were the angle θ between the incident beam and the normal to the sample surface was 5°, 55° (magic angle) and 85°. For θ = 5°, normal incidence, the electric field $\vec{E}$ of the incident photon beam is almost perpendicular to the wurtzite $\hat{c}$ axis, while at θ = 85°, grazing incidence, it lies nearly parallel to $\hat{c}$. When θ = 55°, the magic angle for the wurtzite structure, the spectrum is independent from the mutual orientation of $\vec{E}$ and $\hat{c}$ since the anisotropy term in the absorption cross section vanishes (see 1.1.4).

3.1.2 Data treatment

The recorded experimental data suffer from dead-time and self-absorption distortions and correction for both these effects has to be carried out before performing quantitative analysis. Dead-time distortions are linked to the use of a counting detector, this correction was applied first and was performed by numeric

inversion of formula (1.55). The dead-time for our set-up was estimated in the following way: the fluorescence at a specific incident energy was recorded as a function of the distance between the detector and the sample surface and the curve obtained was fitted with formula (1.55), exploiting the inverse dependence of photons impinging on the Ge diode on the square of the sample-diode distance. Once the dead-time is known, numerical inversion of recorded spectra can be carried out easily with a recursive procedure[7]. Figure 3.2 shows a spectrum before and after dead-time correction.

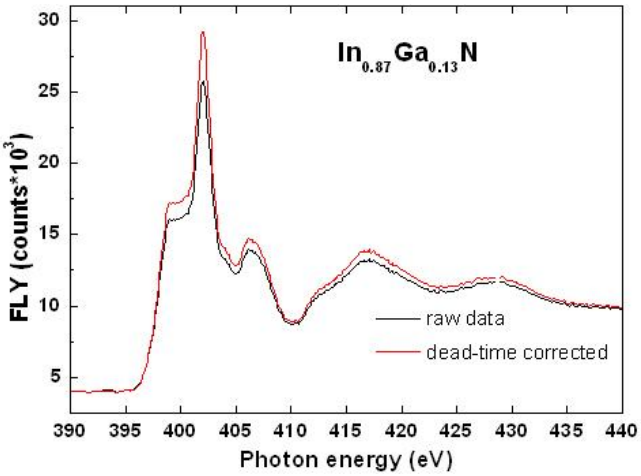

Figure 3.2. Dead-Time correction of normal-incidence FLY on InGaN with 87% In concentration. Significant distortions occur for photon counts exceeding 15×10^3.

Self-absorption effects are present because samples measured are thick and rich of N. As explained in 1.1.4, one can minimize this effect by recording spectra at normal incidence, but in this work the linear dichroism was exploited as a tool to selectively probe the electron density distribution along specific lattice directions and the use of different acquisition geometries was inevitable. To correct spectra for unwanted self-absorption modulations, we performed a post-acquisition correction following the procedure presented in ref. [8] on dead-time corrected spectra. Figure 3.3 shows the result of this procedure on the sample with 87% In content. Uncorrected (black line) and self-absorption corrected spectra (red line) are normalized and superimposed. Spectra are shown for all the three different acquisition geometries, indicated with a sketch on the right side of the graph: self-absorption smears spectral oscillations and affects spectra more seriously going towards grazing incidence, as expected according to the derivation presented in Appendix 1 of the first chapter.

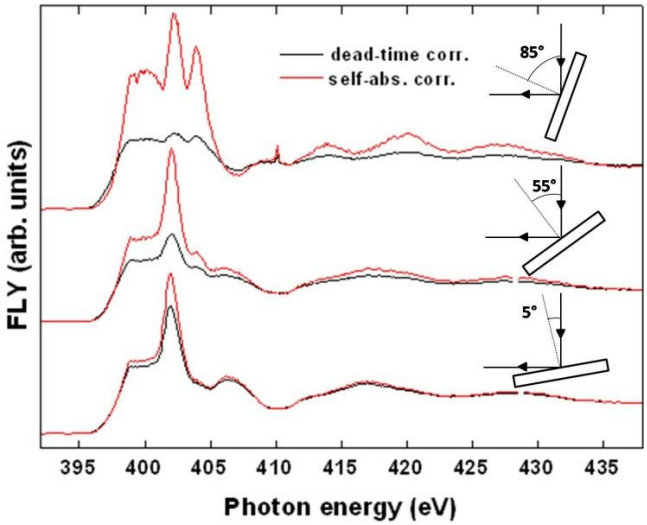

Figure 3.3. Data before (black line) and after (red line) self-absorption corrections. A sketch of the geometry of the acquisition for each spectrum is given. Spectra taken at increasing θ are more affected by self-absorption effect.

After dead-time and self-absorption corrections, the spectra were normalized far from the absorption edge, i.e. at 440 eV.

3.1.3 Experimental results and discussion

The results will be divided into two parts: first spectra taken on as grown samples will be presented, focusing on the spectral variation due to increasing Ga concentration and on the dichroic modulation of peak intensities. Then the effect of H irradiation on the whole series will be exposed.

Figure 3.4 displays all the data relative to as grown samples. On the left graph, spectra are divided into three panels, one for each acquisition geometry used. In each panel the four spectra are stacked and ordered from the top to the bottom according to decreasing In concentration. The spectral line shape at a given polarization is the same for all samples, indicating a good alloy quality and the absence of a marked phase separation. With increasing Ga content a mild blue-shift of spectral features is clearly seen.

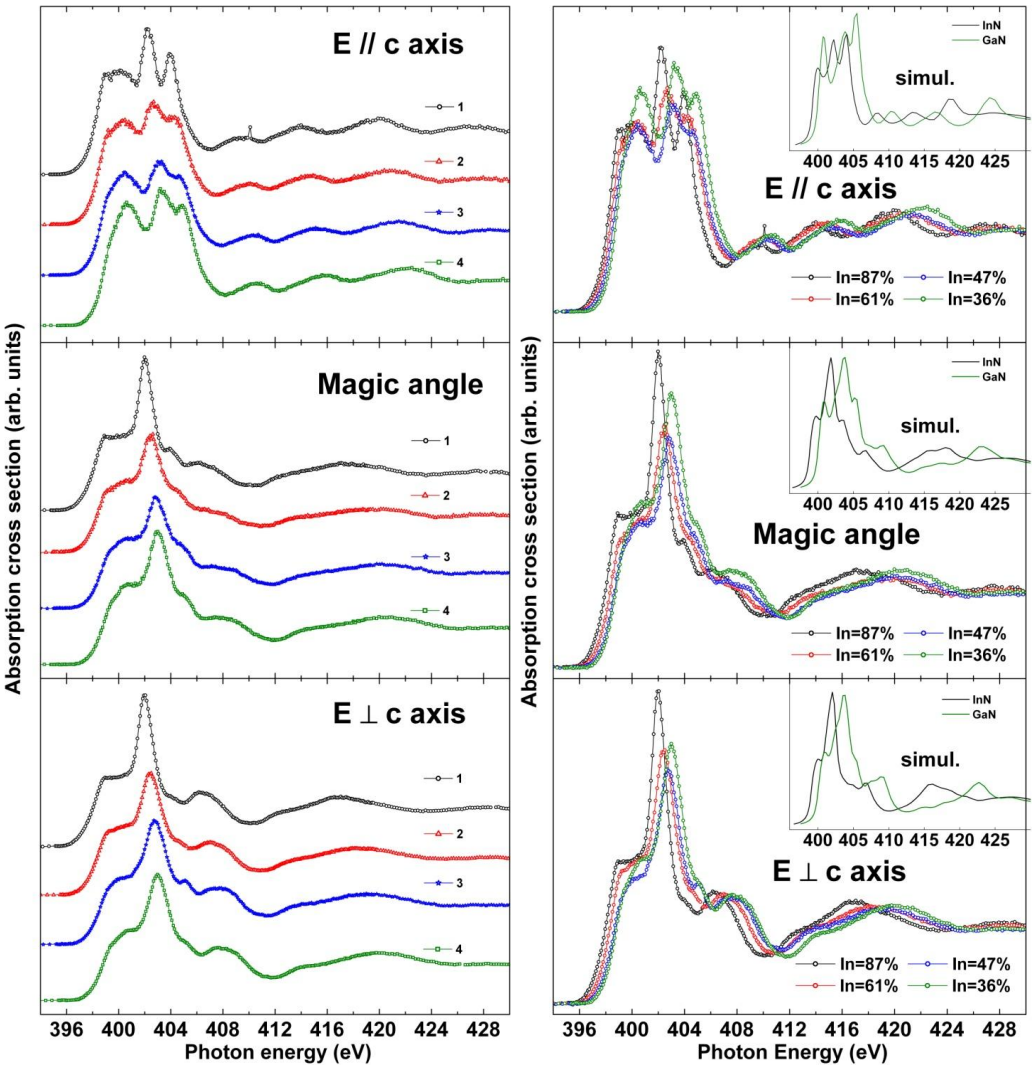

Figure 3.4. Experimental spectra on as grown samples recorded at grazing incidence (top panels), at the magic angle (middle panels), where the effects of anisotropy are cancelled out, and at normal incidence (bottom panels). Spectra are stacked in the left-graph, while they are superimposed on the right-graph to better show the shift of spectral features to higher energies with increasing In content. On the top-right corner are also shown simulated spectra of pure InN and GaN at the same polarization conditions of experimental data.

In the right graph, where the four spectra of each panel are plotted on a common y-scale, the evolution of relative peak intensity with concentration can be better appreciated together with the gradual shift of all spectral features towards lower energies with increasing Ga content. This shift is in agreement with the behavior of pure InN and GaN, that is shown in the insets on the top-right angle of each graph with simulated spectra at each polarization configuration.

To correlate spectral features in the first 10 eV with specific electronic transitions, linear dichroism can be exploited. When the electric field of the exciting photon lies parallel to a direction of maximum electron charge density, the transition to the electron state relative to that specific charge density is favored and if a specific peak in the spectrum is correlated to that transition, it will gain intensity for acquisition geometries approaching this condition[9]. The occurrence of linear dichroism in our spectra derives from the anisotropy of the wurtzite crystal structure and the high degree of linear polarization of the synchrotron photon beam. A description of the wurtzite structure has been given in 2.1.1, where it was specified that the anisotropy differentiates in particular the $\hat{c}$ axis from the basal plane perpendicular to it and we recall that the epilayers we measured were grown with the $\hat{c}$-axis perpendicular to the surface. A sketch of the relative orientation of the atomic micro-structure of InGaN, the surface of the sample and the incident beam direction is given in the top-left panel of Figure 3.5, that is made by four panels, one for each sample measured, where spectra at the three polarization geometries are plotted on the same scale. In this way the evolution of peak intensities can be followed along the InGaN series and it is clearly the same for all the samples, confirming the correctness of the data treatment and at the same time the quality of grown materials. From the sketch in the top-left panel, the angle formed by incident photons and the $\hat{c}$-axis of the wurtzite structure (that is along the normal to the sample surface) can be correlated with the direction of the electric field $\vec{E}$ (which is not drawn, but is perpendicular to the beam direction and lies in the page). It can then be seen that for large θ $\vec{E}$ is perpendicular to $\hat{c}$ and spectra acquired in this geometry probe the electron charge density lying on the basal plane, while for small θ the measurements probe mainly the charge density along the $\hat{c}$-axis. We recall that N in the wurtzite structure is bound to four cations arranged in a tetrahedral environment and that to make these bonds N *s* and *p* orbitals hybridize in the so called sp^3 configuration giving rise to four new orbitals oriented along the tetrahedral bond directions. From the superposition of these new orbitals with the In and Ga ones, interatomic bonds are formed. The unoccupied density of states localized on the N atom thus has mainly *s* and *p* character and with the excitation of the *1s* N core-electrons we are probing the N *p*-projected density of states. It is then quite intuitive that, taking a reference system centered on the N atom with the z-axis along $\hat{c}$, the main contribution to the basal orbitals will be that of p_x and p_y N orbitals while for the single bond along z it will be that of the p_z N orbital.

We can therefore assign peaks A and B in Figure 3.5 to transitions to p_z orbitals, since their intensity increases at grazing incidence (blue dotted curve), while peaks B and D have main contributions from p_x and p_y orbitals because they gain intensity switching at normal incidence (black dotted curve).

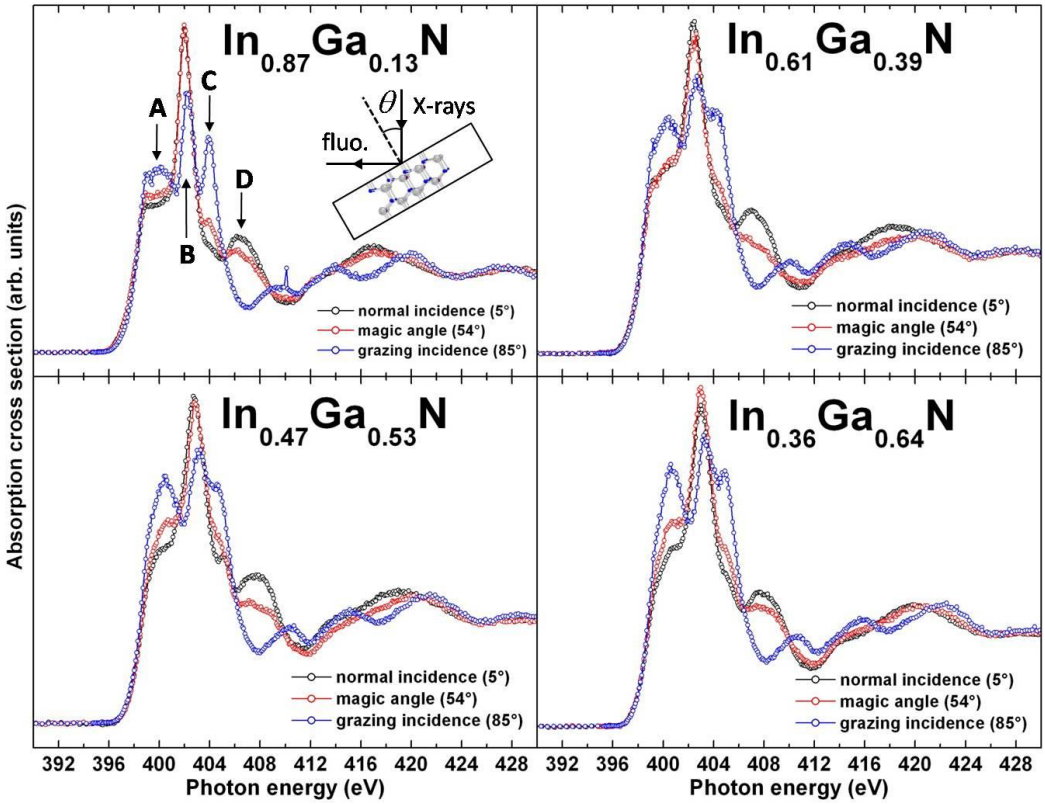

Figure 3.5. Summary of the dichroism shown by all four sample measured. In each panel the spectra acquired in the three different polarizations relative to a sample are plotted on the same y-scale. The evolution of peaks intensity with polarization is the same in all samples: peaks A and B are higher at grazing incidence while peaks B and D increase going towards normal incidence. The magic angle is the condition at which a mean on all the polarization orientations is made.

The peak assignment just illustrated is confirmed by taking advantage of group theory[10] and in particular of the point-group symmetry of the wurtzite structure, C_{6v}. The symmetry of the crystal, in fact, imposes constrains to the mixing of atomic orbitals during band or molecular orbital formation. Not every combination is allowed, but only those that fulfill certain symmetry constrains. Inspection of the character table of the point group symmetry to which the crystal belongs tells which combinations of atomic orbitals are allowed and which are

forbidden. Another useful information that can be extracted from character tables is which electronic transitions are allowed, since the scalar product between initial and final states mediated by the transition operator can be zero for mere symmetry reasons. Therefore allowed transitions can be inferred by the character tables avoiding long calculations. The character table of the C_{6v} point group is shown in Table 3.2. The first column lists the names of the irreducible representations included in the point group; each of them represents a specific response to the symmetry operations belonging to the point group. The response to symmetry operations (*n*-fold rotation, reflection, inversion) is summarized in the columns, one for each group of operations allowed. For example, an element (could be an atomic orbital, a displacement along a specific direction, a vector) that is transformed into itself under all the operations belongs to the A_1 irreducible representation (all the columns filled with 1) also known as the total symmetric irreducible representation.

C_{6v}	E	$2C_6$	$2C_3$	C_2	$3\sigma_v$	$3\sigma_d$		
A_1	1	1	1	1	1	1	z	x^2+y^2, z^2
A_2	1	1	1	1	−1	−1	R_z	
B_1	1	−1	1	−1	1	−1		
B_2	1	−1	1	−1	−1	1		
E_1	2	1	−1	−2	0	0	$(x, y)(R_x, R_y)$	(xz, yz)
E_2	2	−1	−1	2	0	0		(x^2-y^2, xy)

Table 3.2. The character table of the C_{6v} point-group symmetry. First column lists the name of the irreducible representations (IRs) allowed in that symmetry. The columns in the table indicate the symmetry operations of the point-group and the +1/-1, +2/-2 are an indication of how an element belonging to that IR transforms under the column-specific operation. Last two columns list some functions to show which IR they belong to.

Only orbitals belonging to the same irreducible representation can mix, therefore classifying each atomic orbital according to the symmetry of its wave-function will automatically give the allowed combinations. This classification is made in the third and fourth columns, where the functional forms of most of the atomic-wave functions are reported in the row of the irreducible representation they belong to. Therefore atomic orbitals whose wave-functions are linear in x and/or in y can mix with atomic orbitals whose wave-functions have a xz and/or yz spatial dependence. The last two columns of the character table can be used also to establish the allowed electronic transitions. The condition to fulfill is that the symmetry product of the irreducible representation of the initial state, final

state and the transition operator must contain the total symmetric irreducible representation[10]. If the initial state is the ground state, that always belongs to A_1, the rule is simplified the transition is allowed if the transition operator and the final state belong to the same irreducible representation.

In our specific case, taking the origin of the point-group at the N site, the N p_z and *s* atomic orbitals (functional forms proportional to z and $x^2+y^2+z^2$) belong to the A_1 irreducible representation and thus mix together and form a bonding and anti-bonding orbitals, a_1 and a_1^*, while p_x and p_y (functional forms proportional to x and y) give rise to e_1 and e_1^*. The dipole operator is a vector whose z component belongs to A_1, while the x and y components to E_1. In conclusion dipole-allowed transitions from the N *1s* level are those to A_1 and E_1 symmetry states. Moreover, the z component of the dipole operator (incident electric field along *z*) induces transitions to a_1 states and the x and y components (electric field lies on the basal plane) to e_1 states, confirming that peaks enhanced at grazing incidence correspond to transitions to final states made by N *s* and p_z atomic orbitals while those enhanced at normal incidence are to final states made of N p_x and p_y orbitals.

We present now the effect induced by H irradiation on the InGaN series. Figure 3.7 is a summary of all the data acquired; spectra are divided into four panels, each of which contains the measurements on the same material, before and after H irradiation. Spectra in each panel are organized into three groups stacked along the y-axis according to the polarization geometry used. Black spectra refers to as-grown samples while the red spectra are from H-irradiated samples.

Spectra taken at the magic angle are practically unaltered by H incorporation and that is found in all samples analyzed. Two factors concur in this case: the equal weight given to all the possible polarization orientation, that smears variation along specific directions by averaging over all configurations, and the thicker surface layer probed in this geometry. This last factor is important as H can have a non-uniform concentration depth-profile and part of the layer probed at the magic angle can be less affected by H incorporation. Figure 3.6 reports a graph with the penetration depth as a function of the incidence angle for the samples measured. At normal and grazing incidence the layer probed is thinner, about 20 nm while at 54° it is around 60-90 nm depending on the composition of the epilayer. Spectra taken in those configurations shows stronger H effects and as a

general trend the variation of the line shape is more pronounced for higher In content.

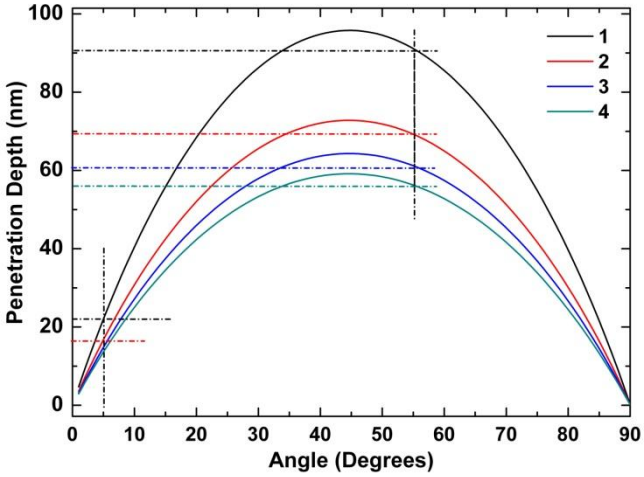

Figure 3.6. Penetration depth of x-rays of 400 eV energy as a function of the incidence angle in the samples analysed.

The In-concentration dependence can be seen by inspection of spectra taken at normal-incidence; also those acquired at grazing incidence show the same trend, even if the sample with 0.36 In content at first seems to be more affected by H-irradiation than that with 0.47 In content. The spectra on the 0.36 In sample, in fact, presents a remarkable lowering of peaks in the first 10 eV after irradiation, but since the height of the near-edge structures with respect to the rest of the spectrum dependents strongly on the self-absorption correction procedure, what should be trusted is the variation induced by H on the spectral line shape more than the variation of the intensity of the structures.

Observing the first 10 eV, apart from a general smearing of features found in all samples, it is clear that H incorporation lowers and smears the first peak, leaving the second and third unaltered in shape. This effect is In-content dependent as the film with 0.87 of In shows the major variation while the sample with 0.36 shows only a general smearing of structures.

We can conclude that H irradiation induced effects are In-content dependent, confirming the results obtained by PL measurements. From the structural point of view, our XANES measurements suggest that the H atoms arrangement modifies the material in such a way that the electron charge density along the $\hat{c}$ axis is more affected, as indicated by the lowering (at grazing and normal incidence) of peak A.

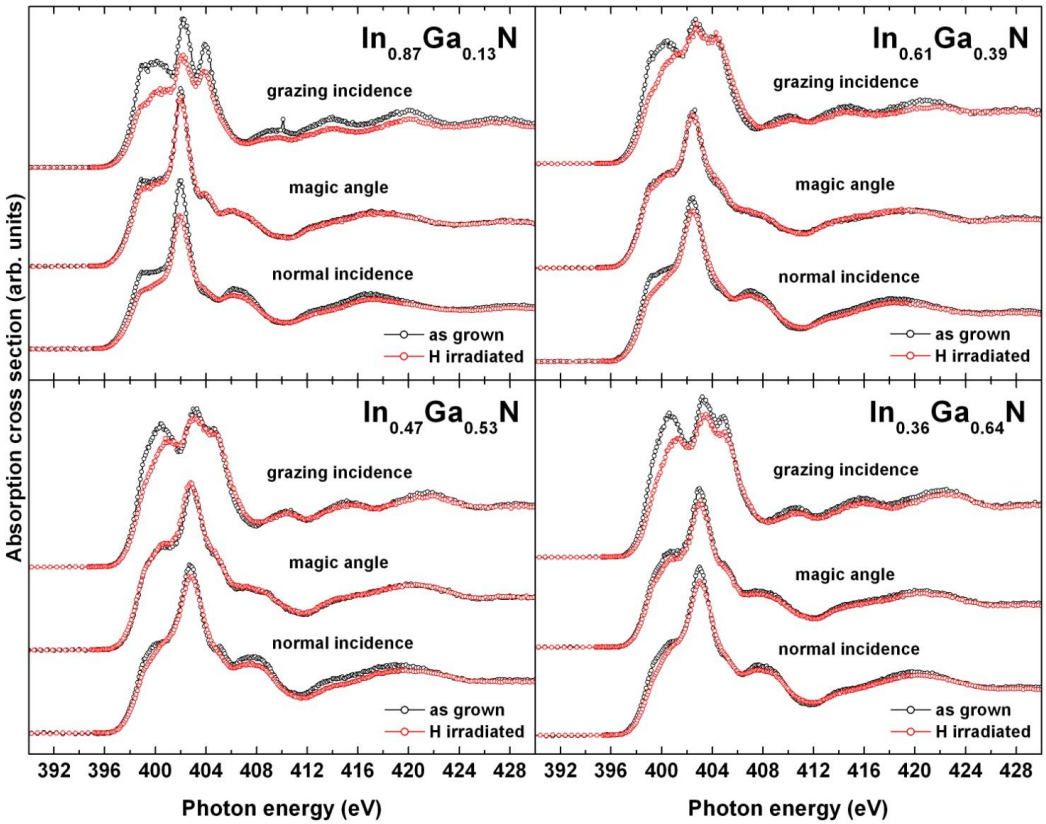

Figure 3.7. Summary of XANES spectra on as grown (black dotted curves) and H-irradiated (red dotted curves) InGaN. Data relative to a specific In concentration are collected in panels, while spectra acquired at different polarizations are differentiated by stacking spectra into three groups along the y-axis. H-irradiation main effect is to reduce the intensity of the first peak at grazing incidence. Also spectra at normal incidence are slightly affected by a smearing of first and third peaks. At magic angle differences are absent. The effect of H is stronger for higher In content; this is seen looking at normal and grazing incidence and considering the line shape variations more than the intensity modulation.

3.2 Data analysis with *ab initio* simulations

In the previous section XANES data at the N K-edge has been discussed from a qualitative point of view, giving some important indications about the effects induced by H incorporation. But for a more quantitative analysis a theoretical support to our experimental results is needed. DFT calculations and *ab initio* simulations performed with the RSMS code FEFF8.4[11] developed by Rehr and coworkers provide a way to get more quantitative information. In particular the aim of the analysis is to determine which arrangement of H atoms is responsible for the observed effects. The procedure followed to answer this

question can be summarized as follows: the as-grown alloy is modelled by a cluster of atoms whose equilibrium positions are obtained by minimizing the valence force field with a DFT code. Then several plausible H-atom arrangements are considered and included into the cluster. The new equilibrium positions of atoms are found with the same minimization procedure and the structure modelling the H-defect is thus obtained. To determine which H cluster is compatible with spectral changes observed in experimental XANES, *ab initio* simulations on the cluster for the alloy and on each H-complex cluster are performed. In this way an evaluation of how H-induced structural changes affect the spectral line shape can be drawn.

The analysis based on *ab initio* simulations will be divided in two parts: the first is about the simulation of the as grown material and only in the second part the various H-defects considered will be described and discussed.

3.2.1 As grown material analysis by simulations of $In_{0.8}Ga_{0.2}N$[12]

The analysis method presented is very time consuming, as will be cleared in the following, therefore we focused only on the case of the In-rich material, the one that based on experimental results is more affected by H incorporation.

The main input for a FEFF8.4 simulation are the geometrical coordinates of atoms in the material. In this work, following a method adopted previously[13,14], the coordinates were provided by density functional theory (DFT) calculations performed in the local density approximation with Hubbard correction (LDA + *U*), as implemented with the plane basis sets in Quantum-ESPRESSO[15]. A 96-atom supercell was generated to simulate the as grown material by a $2 \times 3 \times 2$ replica of the eight-atom orthorhombic unit cell. Density cutoffs used for the unit cell were 30 Ry and 180 Ry respectively with a $2 \times 2 \times 2$ *k*-point mesh including the Γ-point. The electronic channels represented by ultrasoft pseudopotentials were 2*s* and 2*p* for N, 3*d*, 4*s* and 4*p* for Ga, 4*d*, 5*s* and 5*p* for In. The Hubbard *U* correction was applied to the *d* states of In and Ga and to the 2*p* states of N. The *U* values were found parametrically for In, Ga and N in order to reproduce the experimental values of the GaN and InN band gaps and of the position of the Ga and In *d* shells in the density of states.

The 96-atom supercell is a prototype for $In_{0.8}Ga_{0.2}N$ by occupying 20% of cation lattice positions with randomly distributed Ga atoms. A random arrangement of Ga atoms was assumed because the presence of phase separation had been excluded based firstly on the good dichroism observed on the series

measured and secondly by evaluating how spectra should appear if they were merely a weighted linear combination of the end binaries InN and GaN. This second point is illustrated in Figure 3.8.

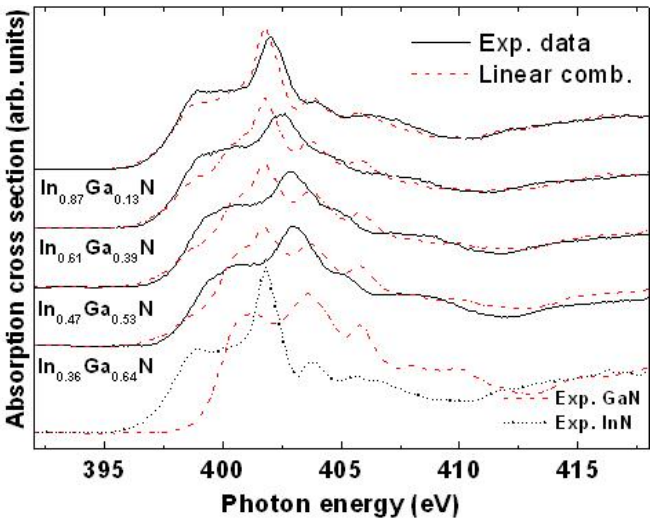

Figure 3.8. Experimental GaN and InN N K-edge XANES acquired at the magic angle were used to obtain linear combinations weighted by the relative concentrations of samples measured. The resultant spectrum is compared to the experimental spectrum. From the bad comparison we can exclude the presence of large phase separation.

Among all the possible ordering arrangements of Ga atoms in the cation sublattice, phase separation and randomness are not the only possibility. Another hypothesis is anti-clustering, where all first nearest neighbors of a N atom are of a cation species and all the second nearest neighbors of the other one. We chose the random arrangement since anti-clustering induces variations in the lattice parameter that was not observed in XRD measurements. Obviously the random hypothesis doesn't have a unique choice, therefore a subset of all the possible configurations was generated, their formation energies were checked and found very similar, spread in a range of only 8 meV/atom. One of the calculated random structures was chosen to simulate experimental XANES and the degree of randomness was checked by calculating the Cowley order parameter[16] for In – In atomic correlations in the second coordination shell, that taking an In atom as the central one is given by

$$\alpha_{In-In} = 1 - \frac{N_{In-In}}{12x}$$

in which N_{In-In} is the average In – In second shell coordination number and x is the In concentration. For a completely random cation arrangement $\alpha_{In-In} = 0$, in

the case of phase separation $\alpha_{In-In} = 1 - \frac{1}{x}$, while for anti – clustering $\alpha_{In-In} = 1$ for $x < 0.5$ and $\alpha_{In-In} = \frac{1}{x} - 1$ for $x > 0.5$. In our random structure $\alpha_{In-In} = 0.024$, to be compared with 0 for a random distribution, -0.25 for phase separation and 0.25 for anti clustering; we can thus state that the distribution of cations in the simulated cluster is quite close to the value expected for a random arrangement. In the chosen 96-atom supercell, the random distribution of 10 Ga atoms gives rise to 3 possible nearest neighbors configurations for a N atom: 4 In, 3 In and 1 Ga, and 2 In and 2 Ga, arrangements that were found respectively for 18, 20 and 10 N atoms in our supercell. Before starting the *ab initio* simulation procedure, the 96-atom supercell was further replicated to have each of the 48 N surrounded by at least 300 atoms to perform RSMS simulations.

We want to point out that in the DFT calculated supercell for the as-grown material, the specificity of atom species were taken into account and not cancelled out in favor of a continuous smooth transition between the two end compounds, that is the approach found in virtual crystal approximation (VCA). In VCA the same random cluster would have been simulated by a perfect non-distorted structure with lattice parameters obtained by a concentration-weighted linear combination of the lattice constants of the binary compounds. The DFT approach ends up with a strong locally strained structure, where the difference in inter-atomic distances of N – Ga and N – In (see 2.1.1) of the end binaries, that is around 0.2 Å, affects severely atomic equilibrium positions. Our XANES simulations will show that this is a fundamental point for a good reproduction of experimental line shapes. A picture of the same random arrangement in $In_{0.8}Ga_{0.2}N$ as given by DFT calculations and VCA approximation is given in Figure 3.9.

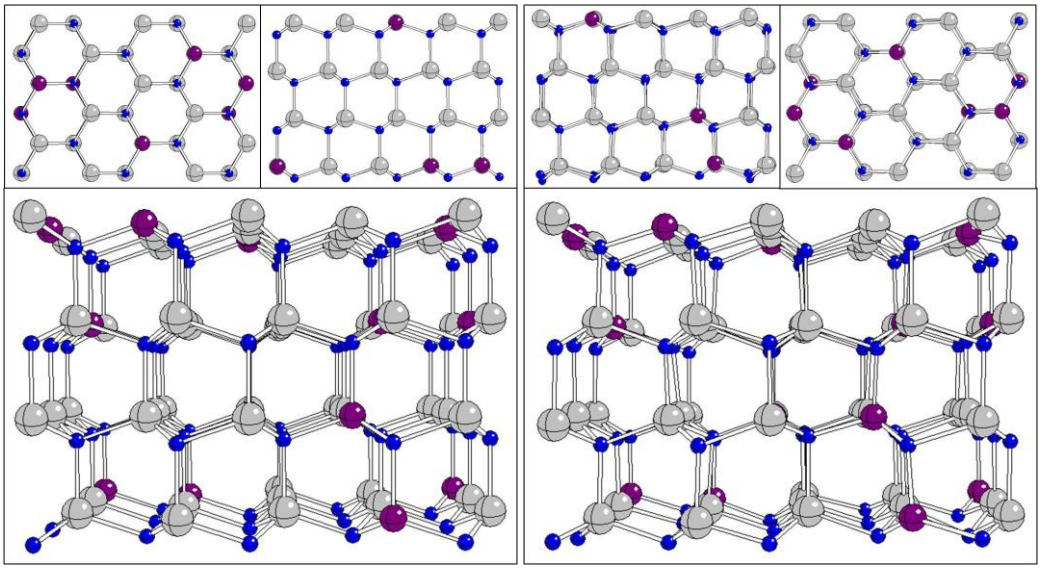

Figure 3.9. $In_{0.8}Ga_{0.2}N$ random structure as calculated by DFT (right side) and VCA (left-side). Top-left panels: crystal structure top-view with the $\hat{c}$ axis perpendicular to the page and no perspective. Top-right panels: side-view of the crystal structure with no perspective, the $\hat{c}$ axis lies on the page along the atomic-planes stacking direction. Central panels: the same view given in the top-right panels but with perspective.

XANES simulations of N K-edge were performed on both the DFT and the VCA cluster with the FEFF8.4[11] code. The scattering potential is calculated in the muffin tin approximation, but a self-consistent field routine has been implemented to partly account for non-spherical charge density effects and a self-consistent radius of 7.2 Å (including almost 90 atoms) around the absorbing atom was used for all simulations. The code calculates the absorption coefficient using the Green's function formalism for full multiple scattering within a sphere centered on the absorber, that in our case was set to 10.2 Å to include almost 300 scatterers. A core-hole on the central atom is included and appropriately screened from valence electrons as a result of self-consistent potential calculation. The polarization vector can be specified in doing simulations with FEFF8.4 and we used this option to simulate normal and grazing incidence geometries, while no polarization was used to simulate data for the magic angle geometry. With those settings we performed simulations centered on each of the N atoms in the cluster in all the three polarization of interest, for a total of 144 simulations. This huge work points out to some interesting results about the influence of local structural distortions on spectral features; in fact plotting simulations centered on N atoms characterized by different nearest neighbor environment, like we have done in Figure 3.10, it clearly appears that when the electric field lies parallel to the $\hat{c}$ axis,

spectral line shape changes a lot for some absorbers. Figure 3.10 displays simulations centered on five different N atoms selected to represent all the possible nearest neighbors configurations found in the cluster (4 In, 1 Ga along the $\hat{c}$ axis, 1 Ga in the basal plane, 1 Ga along the $\hat{c}$ axis and 1 Ga on the basal plane, 2 Ga in the basal plane). The spectra are labeled with the position the N atom has in the list of atoms given by DFT calculations. N 53 and 52 in the simulations performed in *z*-polarization has the second and third peaks much higher than the rest of the spectra and a more attentive analysis shows that the cause is the presence of a Ga atom along the $\hat{c}$ axis.

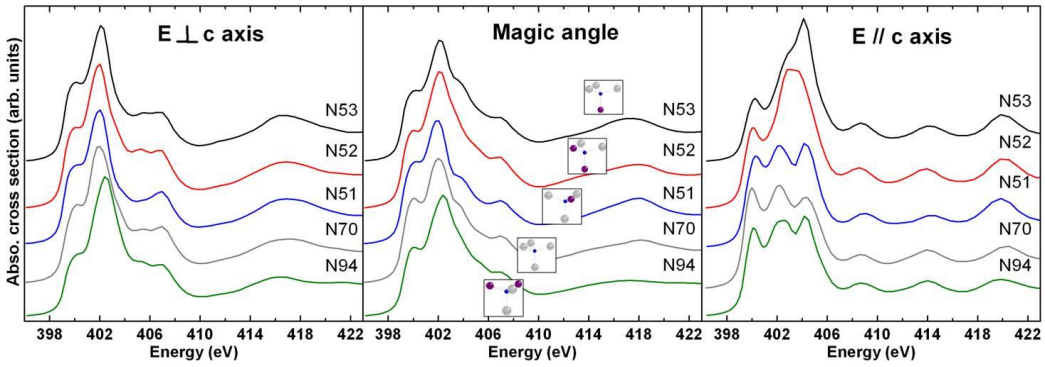

Figure 3.10. In each panel five simulations relative to five different absorbers are plotted, each panel collects the simulations performed in a specific polarization configuration: right panel, x-y polarization; middle panel, no polarization; left-panel, z polarization. Absorbers were chosen to represent all the possible nearest neighbours configurations found in the supercell, as is shown in the sketches in the middle panel. While in the right and middle panel no considerable modifications is detected for different local environments, for z polarization the intensities of second and third peaks are severely affected.

No such strong line shape variations are detected for different environment when the polarization vector is set on the basal plane or at the magic angle. Only when the electric field lies along the *z*-axis the second and third peak gain intensity for N atoms which are bound to a Ga atom placed along the $\hat{c}$-axis. This is a direct consequence of the local distortion induced by the shorter N – Ga inter-atomic distances; we performed test simulations at the same polarization condition on the equivalent N atoms of the VCA cluster, where only the chemistry of the local environment counts as no local distortions are present and N – In, N – Ga bonds are of the same length. As is clearly seen in Figure 3.11, VCA absorbers show two kinds of line shapes, one characteristic of N atoms with a Ga on the $\hat{c}$ axis and the another one for all other nearest neighbors possible configurations. In the first kind the second peak is the highest, while in the second kind the third

prevails, like in simulations obtained with FEFF for a perfect InN crystal (see inset in Figure 3.4).

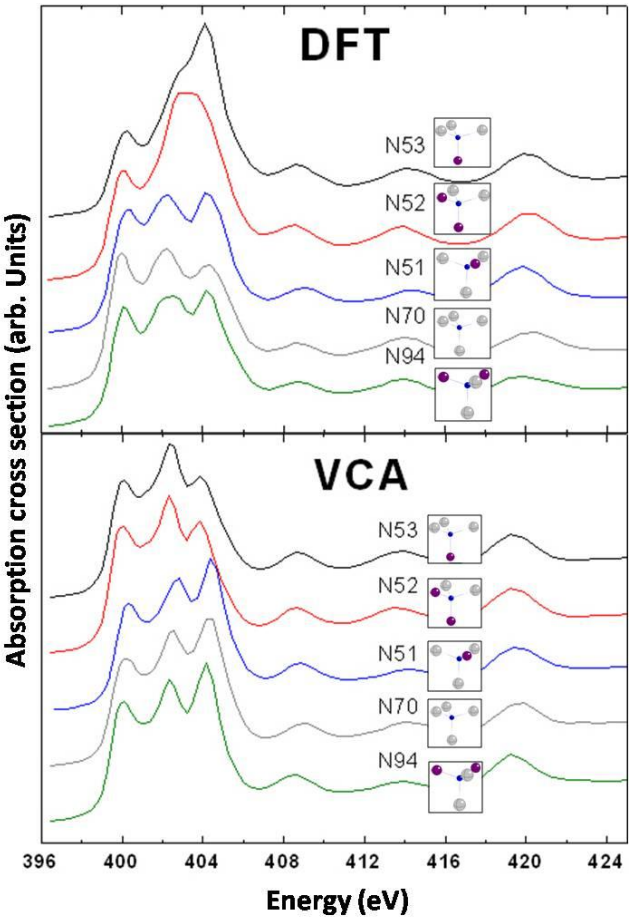

Figure 3.11. The five N atoms discussed in Figure 3.10 has been simulated starting from a supercell generated with the VCA approximation and having the same randon Ga distribution of the DFT supercell. The VCA N absorbers are displayed in the bottom-panel, to be compared with the simulations on the DFT supercell reported in the top-panel. Sketches of the local environment of the N absorber are placed on the corresponding spectrum.

We recall that from our experimental data at grazing incidence, the increase of Ga content in the material has fundamentally three effects: it shifts all the features to higher energies, it increases the intensity of the first peak and it fills the valley between the second and third peak (see Figure 3.4 or even Figure 3.5, where the dichroism for each sample is shown and the evolution of peak intensity at grazing incidence can be referenced to the height of features in the other polarization geometries). From our simulations on the DFT and VCA clusters, since increasing the Ga content means an increased weight of spectra with a Ga on

the $\hat{c}$-axis in the average spectrum, it can be inferred that increasing the Ga content will bring to the filling of the valley between the second and third peak only if disorder is taken into account (DFT cluster), while in an unstrained structure the consequence would be the enhancement of the third peak.

With increasing of Ga content other configurations, like that with 3 Ga and 1 In nearest neighbours, should be considered and may bring about the other spectral modifications just listed, but based only on our study, we can firmly state that local structural modifications are fundamental to account for the spectral line shape and that the random cluster chosen is a good approximation to the real material as it reproduces fairly good our experimental spectra on $In_{0.87}Ga_{0.13}N$ in all the polarizations used. This is shown in Figure 3.12, where experimental spectra taken in the three acquisition geometries are superimposed and compared with the spectra obtained by averaging the 48 N-centred simulations for each polarization condition plotted on the same y-scale.

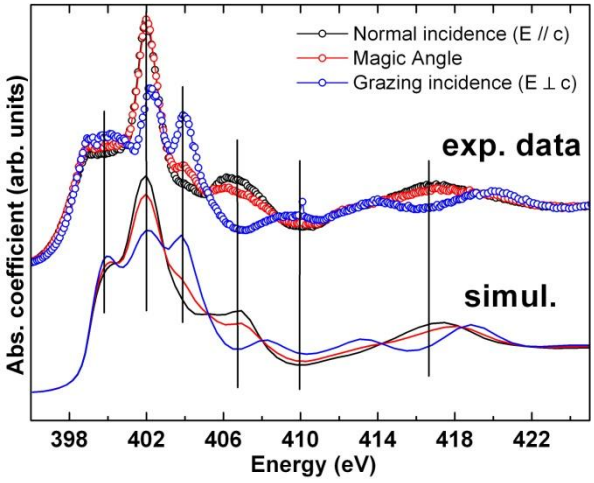

Figure 3.12. Dotted curves: experimental spectra at the three polarization geometries acquired on $In_{0.87}Ga_{0.13}N$. Straight lines: average of the 48 simulations centered on the N atoms composing the cluster for the three polarization geometries. Colour code is for the polarization. The evolution of peaks intensities is very well reproduced by our simulations and also the peaks positions.

Straight lines are given as a guide to the eye to show the good agreement of spectral features between experiment and simulations. The general trend of dichroism is well reproduced and to compare directly data and simulation at a given polarization, Figure 3.13 is also shown.

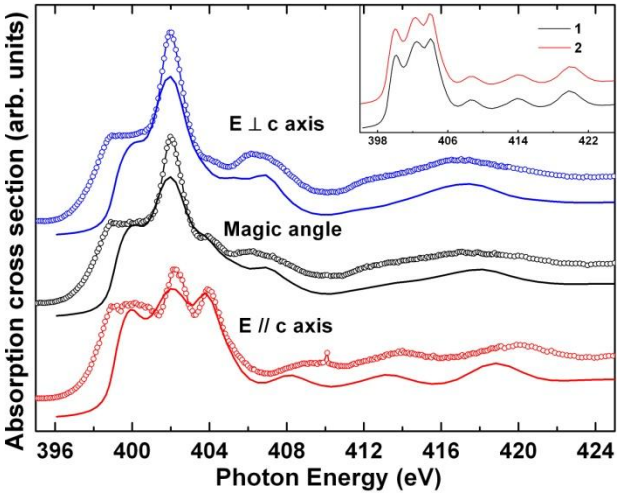

Figure 3.13. Experimental spectra of $In_{0.87}Ga_{0.13}N$ (dotted curves) are superimposed on averaged simulations performed on the DFT supercell (straight lines) for all the three polarization geometries. The inset shows the z-polarized averaged simulations performed on the chosen supercell (black line, label 1) and on a supercell with a different random arrangement of Ga atoms (red line, label 2). The result is independent on the specific random arrangement.

We also checked that this result is independent on the particular random arrangement chosen for the Ga atoms; we did that by considering another 96-atoms supercell generated with Quantum-ESPRESSO; the chosen cluster was calculated and 48 simulations with the polarization vector along the $\hat{c}$ axis were performed. The result is displayed on the top-right panel of Figure 3.13, where the black line is the chosen structure and the red line is the test structure.

In conclusion, the detailed analysis of the $In_{0.8}Ga_{0.2}N$ supercell based on RSMS *ab initio* simulations has demonstrated that a random arrangement of Ga atoms is appropriate for a good description of experimental data. Moreover, we found that the line shape of simulations with polarization set along the $\hat{c}$-axis is remarkably affected by the local strain induced by the different N – Ga and N – In distances. We also found that the trend shown by experimental data for increasing Ga content is in agreement with the spectral variations observed in simulations based on the DFT cluster and induced by local strain. On the contrary, an alloy modeled on the VCA approximation isn't able to provide such good results.

3.2.2 H complexes[3]

Once the supercell reproducing the as grown material has been well characterized and demonstrated to be suitable for spectral simulations, we focused

on the structural distortions introduced by H atoms and how these distortions influence the spectral line shape.

H is a high-diffusing element thanks to its small radius and when incorporated into a material it can occupy several sites in the crystal. It was already mentioned at the beginning of this chapter that the position H assumes in the material is correlated with the roles it plays in modifying its electrical properties. Without going into the details, we only mention that the formation energy and the stabilisation level of an H-defect depend on the arrangement of H atoms. In particular the stabilisation level determines the electrical activity of the defect depending on the Fermi level of the material[2,17]. Therefore the study of the structure of the H defects is fundamental for a full understanding of the physics of H in semiconductors.

We already presented experimental results on H-irradiated samples measured with XANES at the N K-edge and now we briefly overview the EXAFS results obtained at the In K-edge and measured on the beamline SAMBA, at the SOLEIL synchrotron, Saint Aubin. The XANES and EXAFS measurements were planned to determine by a crossed analysis the H-complex formed after H-irradiation and causing the shift of the PL peak.

The evidence at the In K-edge is that H irradiation induces a lowering of the second shell peak in the Fourier transforms (FT) of spectra for samples with In concentration exceeding 40%. This means that In second nearest neighbours distances are scattered by the H-defect formation. The effect is maximised for larger In concentration, therefore also in the EXAFS case the analysis was substantially based on data taken on the sample with the highest In content, the $In_{0.82}Ga_{0.18}N$. The FT of the as grown and H-irradiated samples are shown in Figure 3.14.

The different arrangements H atoms can take in the specific case of $In_{0.8}Ga_{0.2}N$ were analysed by introducing H atoms into the $In_{0.8}Ga_{0.2}N$ supercell obtained with DFT-LDA calculations and described previously. Since the energetically favoured single-H positions are the bond-center configuration, where the H atom is placed in the middle of a N – In bond, and the anti-bonding configuration, where the H is bound to N in the opposite direction with respect to the N – In bond, H atoms were placed in these positions. Many combinations were tried, changing the number of H atoms or their configuration. Once H atoms have been included, the new equilibrium positions of the whole cluster

were obtained by leaving the atoms free to relax with the usual minimization procedure.

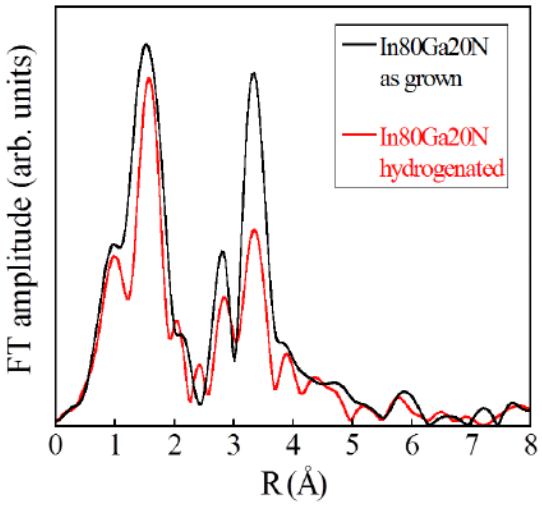

Figure 3.14. Furier Transforms (FT) of EXAFS spectra at the In K-edge on as grown (black line) and H-irradiated (red line) $In_{0.8}Ga_{0.2}N$. H causes a lowering of the second shell peak; this means structural distortion has the main consequence of spreading the second nearest neighbours distances of In atoms.

Among all the possible arrangements H atoms can take, in this work three groups were considered:

1. single H atoms bound to a N
2. a N vacancy decorated with a single H bound to a N in the vicinity
3. an In vacancy with 3 or 4 H atoms bound to the nearest neighbours of the In vacancy
4. multi-H complexes decorating an In atom with each H bound to a N.

In all these cases the H is bound to a N atom and this because H is attracted by N due to its high electronegativity. Single H defects have been considered as they have the lowest formation energy based on DFT calculations; the Nitrogen vacancy, on the other hand, has the lowest formation energy among intrinsic defects and it is surely present in large concentrations. The In vacancy as well has to be considered especially due to the difficulty in growing this material with high In content that makes this defect easy to find. As an In vacancy leaves behind many dangling bonds and as the H binds easily with N, in this case many H atoms were added. The last group of defect, that of multi-H complexes, has been analysed because with a large H concentration, like in our case, H atoms can cooperate to reduce local strain by clustering and having a single defect made by many H atoms

can be energetically less expensive than having the same number of H atoms dispersed in the material.

These defective supercells were used for the analysis of both EXAFS and XANES spectra, but since EXAFS simulations were faster, each defect was first filtered according to its ability to fitting the EXAFS results. For some defects the second shell peak was enhanced in the simulation performed on the defective supercell as compared to that of the original supercell: these supercells were thus immediately discarded. In vacancies and multi-H complexes with many H atoms placed in bond-centered position belong to this class of rejected defects. Those defects that, on the contrary, gave simulations reproducing the decrease in the second shell, were used to fit the experimental data by doing a linear combination of the defective simulation with the non defective. From the weights used for a good fit, the concentration of the defect was estimated and the structures giving the most promising results, that is good fits with low defect concentration, were submitted to the long XANES *ab initio* analysis with a method analogous to that described before.

Before reporting the results obtained by simulating the various structures, it can be useful to look at how H atoms are actually arranged in the material and how their presence induces local strain, in particular for those structures that have been analysed also with XANES simulations. All the pictures shown in the following are made by three panels, on the top of the figure two smaller panels show the material as seen from the top (*x* and *y* axis lying on the page and the *z* axis coming outward) and from one side (the *z*-axis lies on the page and the stacking of N and In/Ga layer is visible) with no perspective, so that the distortions induced by H are more clear. The main panel is the front view with perspective in addition.

SINGLE H: two cases have been considered: the H_{bc} (bond-centred configuration) with a H placed in the middle of a N – In bond and H_{ab} (anti-bonding configuration) with the H bound to the N but outward the N – In bond direction. The two structures are shown in Figure 3.15, with the H atom in red, N atoms in blue, Ga in violet and In in grey. When the H is in bond-centred configuration, the In participating to the bond is strongly displaced, while when the H is placed in anti-bonding configuration, the In remains almost in its original position and the N – In bond is stretched. In both cases the structure is distorted by the presence of the H, also if in Figure 3.15 the H_{bc} seems more affected.

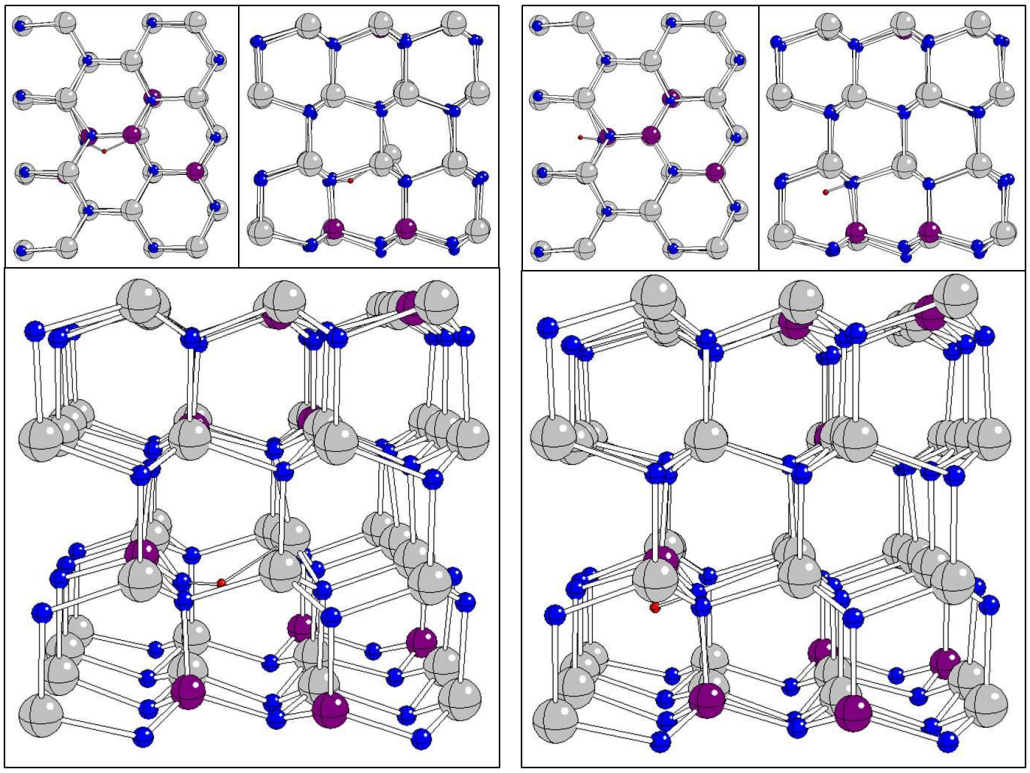

Figure 3.15. Left: H_{bc} in $In_{0.8}Ga_{0.2}N$ supercell. Right: H_{ab} in $In_{0.8}Ga_{0.2}N$ supercell.

N VACANCY WITH SINGLE H: the second group of defective structures considered was the group with a Nitrogen vacancy and a single H atom. The options for the H position were in bond-centered configuration in a N – In bond near the vacancy (referred to as V_N+H_{bc}), in anti-bounding configuration respect to the same N – In bond (referred to as V_N+H_{ab}), and finally also the case of the so called multi-centre bond was considered, where the H atom occupies the lattice position of the N vacancy. This last defect has been claimed to be a double donor in InN and therefore a candidate as the cause for the intrinsic *n*-doping[18]. These structures are pictured in Figure 3.16 and Figure 3.17. The vacant N atom is the same in all three cases and can be spotted by looking the multi-bond centre case, where the H substitutes for N. The same N – In bond is involved when the H is in bond-centre or anti-bonding configuration, so that those cases are like the single H cases with a Nitrogen vacancy added in the vicinity. The structures relax in a different way as the In, that can be considered as the centre of the defect, has less constrains and it is more free to move. The less distorted structure is the one with the H in multi-centre configuration, since it compensates the absence of the N and doesn't stretch or compress any bond.

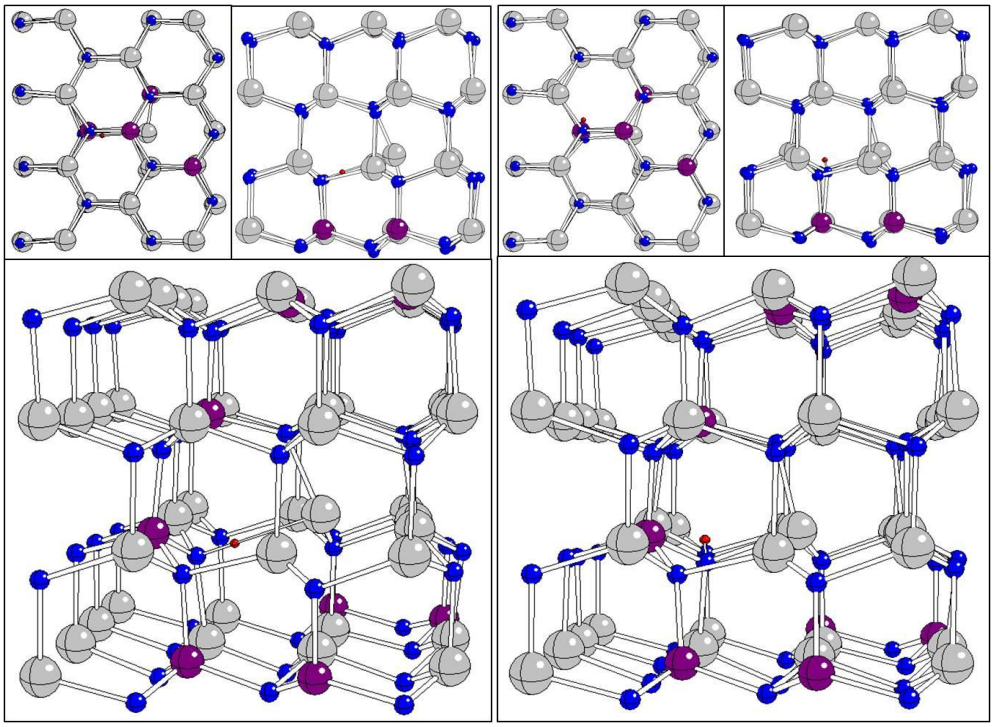

Figure 3.16. Left: V_N+H_{bc} in $In_{0.8}Ga_{0.2}N$ supercell. Right: V_N+H_{ab} in $In_{0.8}Ga_{0.2}N$ supercell.

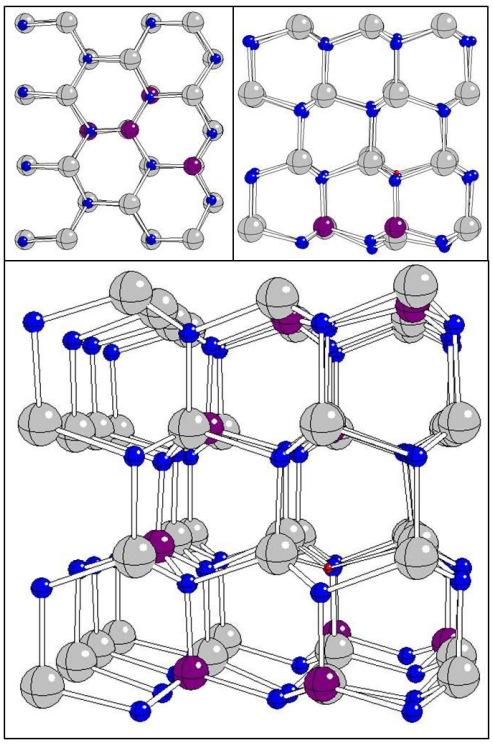

Figure 3.17. V_N+H_{mcb} (multi-center bond) in $In_{0.8}Ga_{0.2}N$ supercell.

MULTI H: the last group of defects is that of multi-H complexes with 3 or even 4 H atoms all around the same In. These geometries were analysed because performing DFT calculations it turned out that their formation energy is not far from that of 4 single H defects in the same supercell. This means that when a high H concentration is expected, the H clustering can be favoured over the formation of an equal number of single H defects. This happens because after the incorporation of a single H atom, the local distortion induced can favour the accommodation of other H atoms in the surroundings of the same In. For example if a H_{ab} is present, the N – In bond is stretched and the In atom is slightly pulled down. That configuration favours the incorporation of a H_{BC} (capital letters indicate a H placed along a $\hat{c}$-axis bond) in the middle of the $\hat{c}$-axis N – In bond. In our case the dose of H incorporated by the material is large and clustering should be considered as an option.

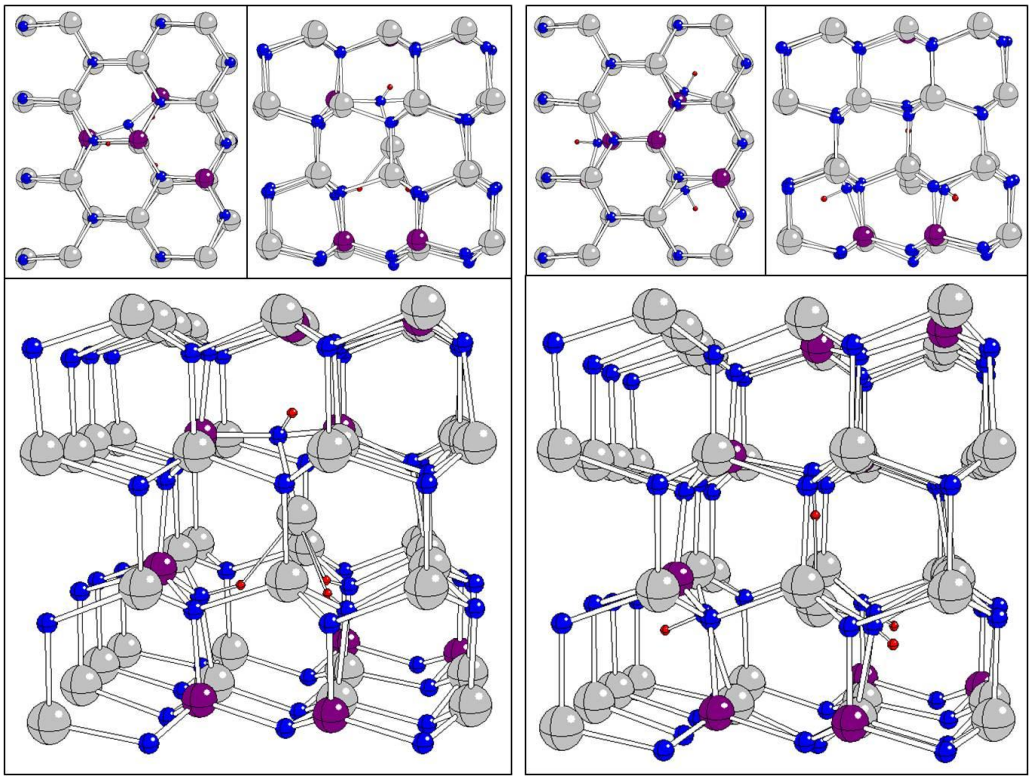

Figure 3.18. Left: $3H_{bc}$+H_{AB} in $In_{0.8}Ga_{0.2}N$ supercell. Right: $3H_{ab}$+H_{BC} in $In_{0.8}Ga_{0.2}N$ supercell.

Two multi-H complexes are shown in Figure 3.18; both are made by 4 H bound to the 4 N nearest neighbours of the central In atom. The structure on the left has the three H linked to the N on the basal plane in bond-centred

configuration, while the last H is placed in anti-bonding configuration along the $\hat{c}$ axis. The result is that the central In (labelled In45) is pulled up by the stretching of the *z*-bond and also by the 3 H in the basal plane. On the right the situation is reversed and 3 H linked to three basal-N are in anti-bonding and the H along the $\hat{c}$ axis is in bond-centred configuration. This time the In is pushed down since the N on the basal plane are pulled apart.

To determine how structural distortions induced by a specific H defect modulate the N K-edge XANES spectrum, in analogy with the work done for the as grown material, we performed several *ab initio* simulations for each defect considered, setting as absorber a different N atom at every simulation. The parameters used for the simulations were the same described previously, with the difference that only the case with the polarization vector lying on the $\hat{c}$ axis was considered, since it is the configuration where the effects of the H atoms are maximized and to reduce computational time. To track N atoms through the various structures analysed, the same numerical label was given to corresponding Nitrogen atoms based on how they are listed in the cluster without H. In this way the influence of the defect on a specific absorber can be easily seen by comparing the simulation performed on the original structure, before H was introduced, with the one centered on the same N but with the defect.

This atom-by-atom comparison is a sort of map of the $\hat{c}$-projected H-induced local strain and as expected it shows that N atoms bound to H or very near to the defect are more affected, but it also shows that modulations are present also for absorbers far from the center of the defect. Moreover, even in structures where the H defect seems to induce a negligible strain, like in the multi-center bond, we still find absorbers whose simulated spectra are seriously affected. This is shown in the following, where the effect of strain on the N atoms placed around the defect are given for most of the structures considered. This comparison is made easier by the fact that all the defects are placed around the same In atom (In45) and therefore we are speaking of the same 4 Nitrogen for all the structures. To make clear which N atom is the center of the simulations presented, we placed the graphs with the simulations before (black line) and after (red line) H was introduced on the picture of the structure and black arrows to indicate the N atom they are referred to.

The first picture, Figure 3.19, shows the single H cases, H_{bc} on the left and H_{ab} on the right.

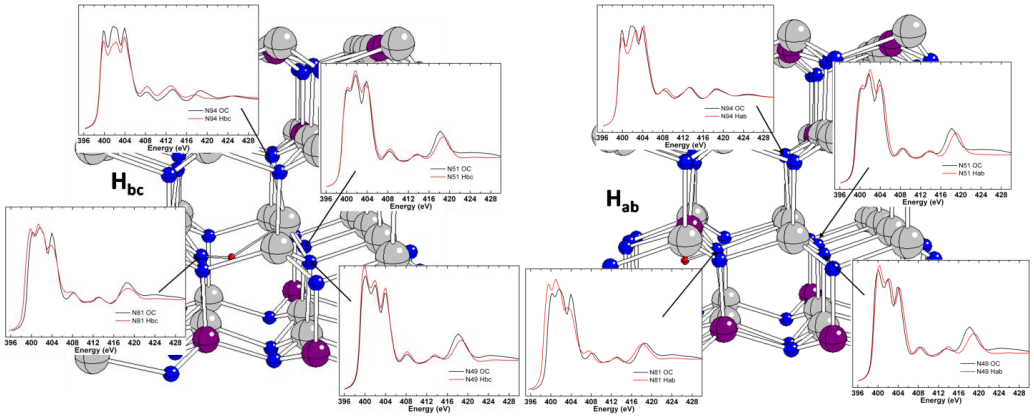

Figure 3.19. Simulations on the 4 N around the center of the defect before and after the introduction of the H atom are displayed in the various graphs. The arrows indicate the reference N. Left: H_{bc} in $In_{0.8}Ga_{0.2}N$ supercell. Right: $3H_{ab}+H_{BC}$ in $In_{0.8}Ga_{0.2}N$ supercell.

Clearly this defect doesn't have a large range as its nearest neighbours don't appear much affected. To evaluate the global effect of H on the structure, we averaged the simulations relative to the 4 N nearest neighbours of In45 together with the third shell of N around In45, for a total of 16 atoms. The result for the single H cases is shown in Figure 3.20

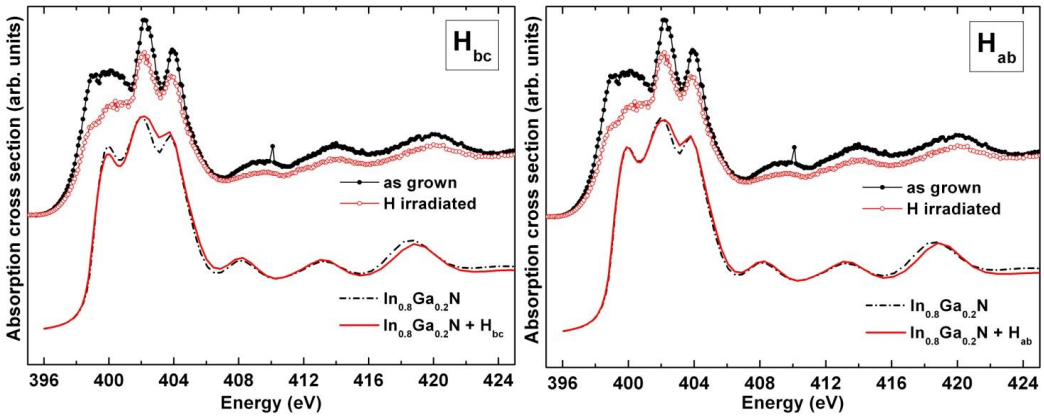

Figure 3.20. Left: experimental data on $In_{0.87}Ga_{0.13}N$ as grown (black full-dotted curve) and and H-irradiated (red empty-dotted curve) are superimposed on the top of the graph. On the bottom the average simulation on pure $In_{0.8}Ga_{0.2}N$ (black dashed-dotted line) is compared with the average simulation on $In_{0.8}Ga_{0.2}N$ with single H in bond-center configuration. Right: the same experimental data are shown on the top part of the graph, in the bottom part the average simulation on pure $In_{0.8}Ga_{0.2}N$ is superimposed to the average simulation on $In_{0.8}Ga_{0.2}N$ with a single H in anti-bonding configuration.

where the comparison is made with the experimental data on the effect of H on the sample with 87% of In content. The dash-dotted black line is the average of the simulations performed on the DFT structure without any H atom. The N entering the average are the same used in the average for the H_{bc} and H_{ab} clusters, therefore the first and third N shells around In45. In this way the average simulated spectrum of the H-cluster is a spectral evaluation of the structural distortion induced by that specific defect. The comparison with the average simulated spectrum on the defect-free cluster shows that none of the two is in agreement with experimental results.

The defects with a N vacancy are shown in the following: first the vacancy alone (V_N) in Figure 3.21, then V_N with a H in bond-center or anti-bonding configuration bound to one of the nearest neighbours in Figure 3.22 and finally the multi-center H that is placed in the V_N lattice position in Figure 3.23. The vacant N is always the same and is one of the nearest neighbours of In45, therefore only three graphs are present in these pictures.

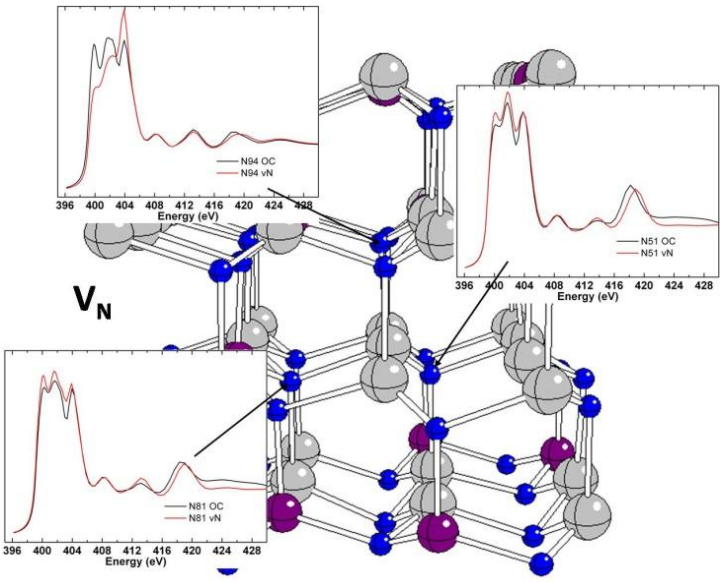

Figure 3.21. Simulations on the 3 N around the center of the defect (In45) before and after the introduction of a N vacancy are displayed in the various graphs. The arrows indicate the reference N.

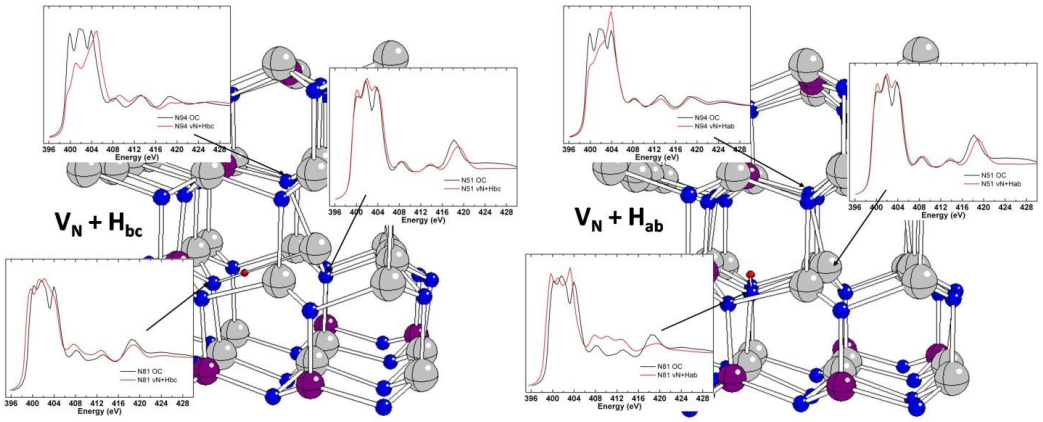

Figure 3.22. Simulations on the 3 N around the center of the defect (In45) before and after the introduction of a N vacancy and a H atom are displayed in the various graphs. The arrows indicate the reference N. Left: V_N+H_{bc} in $In_{0.8}Ga_{0.2}N$ supercell. Right: V_N+H_{ab} in $In_{0.8}Ga_{0.2}N$ supercell.

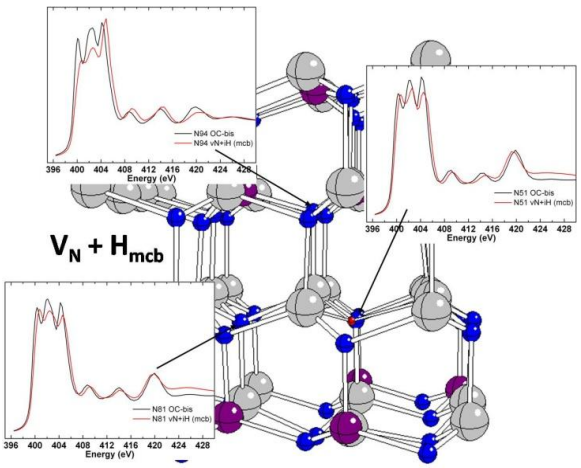

Figure 3.23. Simulations on the 3 N around the center of the defect (In45) before and after the introduction of a N vacancy and a H atom in multi-center position are displayed in the various graphs. The arrows indicate the reference N.

The results obtained by averaging the first and third shell around In45 for V_N + H_{bc} and V_N + H_{ab} are shown in Figure 3.24, that for V_N + H_{mcb} and the V_N alone in Figure 3.25. This time the defects determine a more serious variation of the line shape; but as can be seen by comparing V_N + H_{ab} with V_N the major effect is due to the only Nitrogen vacancy.

V_N + H_{bc} gives better results, but still the second and third peaks are too high. The multi-center bond has a different line shape also for the average simulation of the cluster without H. This is because the DFT calculation for the last case required a thicker *k* mesh and also the original cluster had to be

recalculated in the same conditions. However, it doesn't match the experimental findings as the lowering of the first peak is the less pronounced.

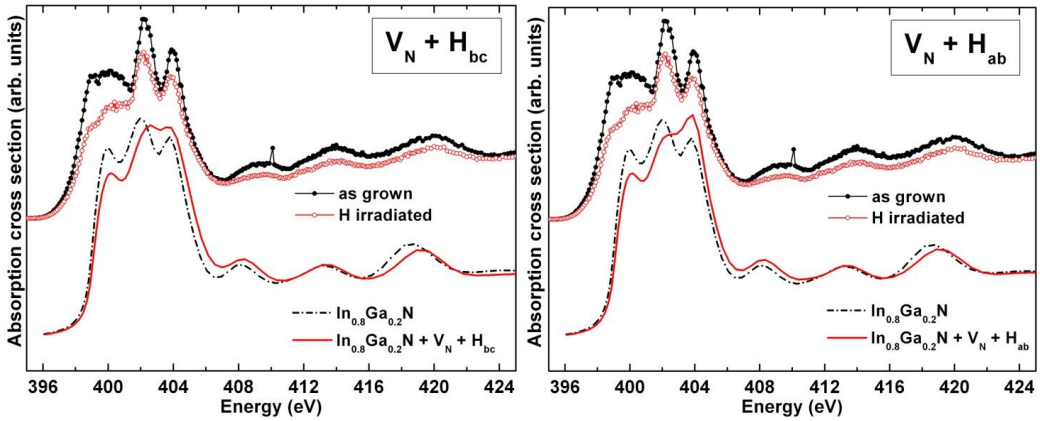

Figure 3.24. Left: experimental data on $In_{0.87}Ga_{0.13}N$ as grown (black full-dotted curve) and and H-irradiated (red empty-dotted curve) are superimposed on the top of the graph. On the bottom the average simulation on pure $In_{0.8}Ga_{0.2}N$ (black dashed-dotted line) is compared with the average simulation on $In_{0.8}Ga_{0.2}N$ with a N vacancy and a single H in bond-center configuration. Right: the same experimental data are shown on the top part of the graph, in the bottom part the average simulation on pure $In_{0.8}Ga_{0.2}N$ is superimposed to the average simulation on $In_{0.8}Ga_{0.2}N$ with a N vacancy and a single H in anti-bonding configuration.

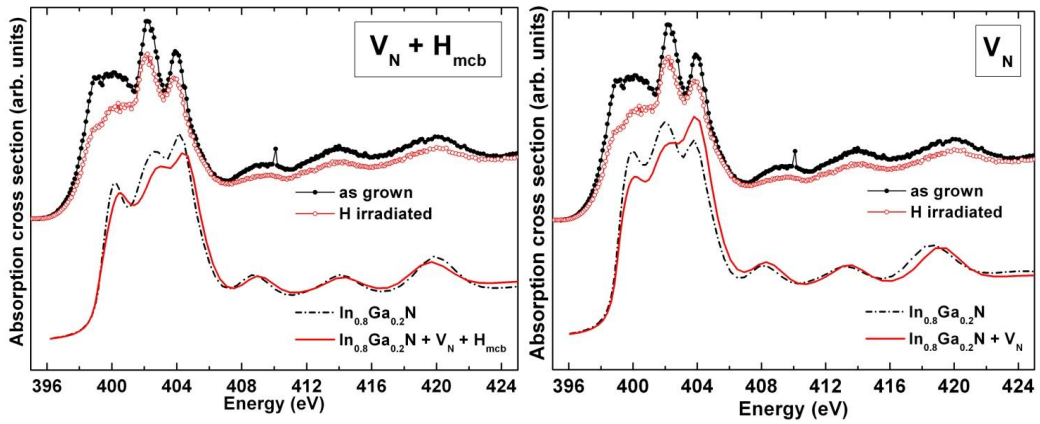

Figure 3.25. Left: experimental data on $In_{0.87}Ga_{0.13}N$ as grown (black full-dotted curve) and and H-irradiated (red empty-dotted curve) are superimposed on the top of the graph. On the bottom the average simulation on pure $In_{0.8}Ga_{0.2}N$ (black dashed-dotted line) is compared with the average simulation on $In_{0.8}Ga_{0.2}N$ with a N vacancy and a single H in multi-center configuration. Right: the same experimental data are shown on the top part of the graph, in the bottom part the average simulation on pure $In_{0.8}Ga_{0.2}N$ is superimposed to the average simulation on $In_{0.8}Ga_{0.2}N$ with a N vacancy alone.

The last group of defects is that of multi-H complexes. Here no atom is missing, but 3 or 4 H atoms are bound to the nearest neighbours of In45. We present the results of the defects with $3H_{ab}$ and with $3H_{ab}$+H_{BC} where capital letters indicate that the reference bond for the H in question is along the $\hat{c}$ axis.

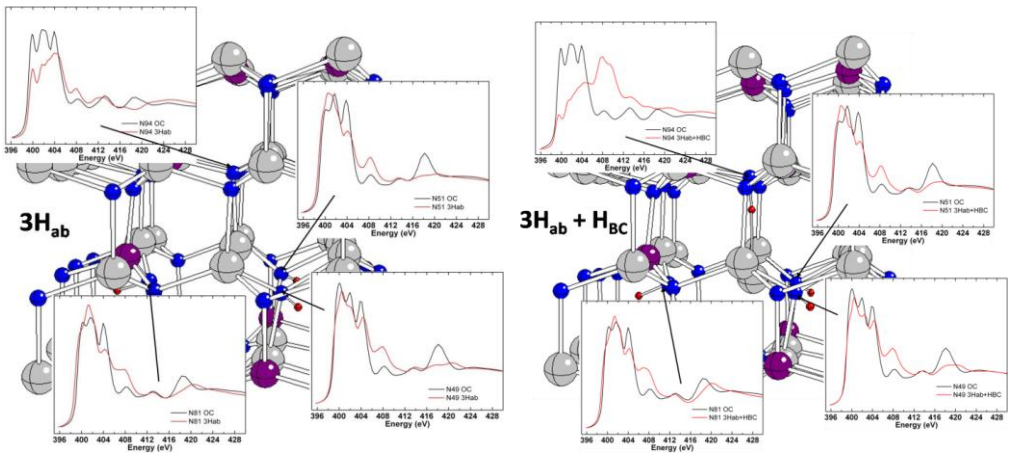

Figure 3.26. Simulations on the 4 N around the center of the defect (In45) before and after the introduction of H atoms are displayed in the various graphs. The arrows indicate the reference N. Left: $3H_{ab}$ in $In_{0.8}Ga_{0.2}N$ supercell. Right: $3H_{ab}$+H_{BC} in $In_{0.8}Ga_{0.2}N$ supercell.

In Figure 3.26 the single simulations on In45 nearest neighbours are displayed, on the left for $3H_{ab}$ and on the right for $3H_{ab}$+H_{BC}. Those defects severely modify the line shape of simulations, especially the one referred to the N lying on the $\hat{c}$ axis that are strongly affected by the large displacement of In45.

At first it seems these simulations are going too far from the experimental findings, but this is true for single simulations, while our experimental data reflect the average of N atoms near and far from the defects. Doing the average as for the other structures considered, the strong distortions seen on single simulations are smoothened and still an appreciable deviation from the simulation on the original supercell is seen. The result is displayed in Figure 3.27; the 3 H atoms in anti-bonding configuration induce a huge distortion in the structure and this has a strong influence on the line shape of the average. The variation is not in good agreement with the data, even if it is the first defect with a variation comparable in amplitude with the experimental finding. The addition of a H atom in bond-center position along the $\hat{c}$ axis mitigate the distortion and the result on the averaged simulated spectrum is in good agreement with the experiment, with only an excessive lowering of the third peak intensity.

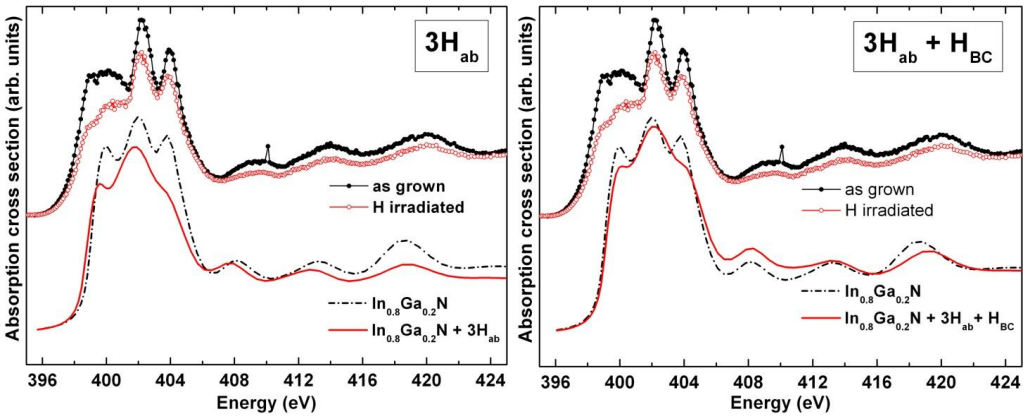

Figure 3.27. Left: experimental data on $In_{0.87}Ga_{0.13}N$ as grown (black full-dotted curve) and and H-irradiated (red empty-dotted curve) are superimposed on the top of the graph. On the bottom the average simulation on pure $In_{0.8}Ga_{0.2}N$ (black dashed-dotted line) is compared with the average simulation on $In_{0.8}Ga_{0.2}N$ with three H in anti-bonding configuration bound to three N in the basal plane. Right: the same experimental data are shown on the top part of the graph, in the bottom part the average simulation on pure $In_{0.8}Ga_{0.2}N$ is superimposed to the average simulation on $In_{0.8}Ga_{0.2}N$ with three H in anti-bonding configuration bound to three N on the basal plane and a single H in bond-center configuration bound to a N along the c axis.

If we now cross our results with those obtained by EXAFS simulations, agreement is found for the $3H_{ab}+H_{BC}$ defect. For what concerns the EXAFS analysis on the structures just presented, the highest defect concentration is that of single H defects, with 6% of total N atoms with a defect for H_{ab} and 10% for H_{bc}. The N vacancy requires a lower concentration of defect for a good fit, estimated to be almost 4.4%. The lowest concentrations are those needed to fit the data with the $3H_{ab}$ (3.8%) and $3H_{ab}+H_{BC}$ (2.4%) defects.

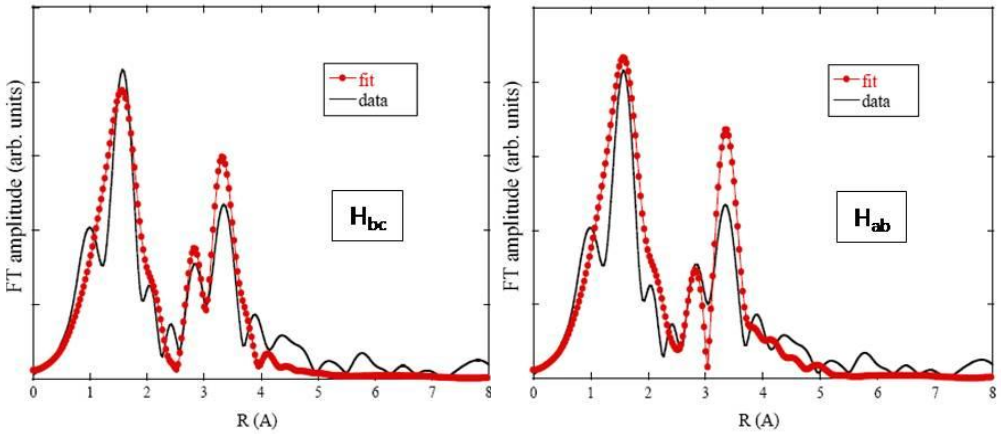

Figure 3.28. Left: FT amplitudes of H-irradiated $In_{0.82}Ga_{0.18}N$ (black line) with superimposed the fit obtained with $In_{0.8}Ga_{0.2}N + H_{bc}$ cluster. Right: the same data repeated with the fit obtained by the cluster $In_{0.8}Ga_{0.2}N + H_{ab}$.

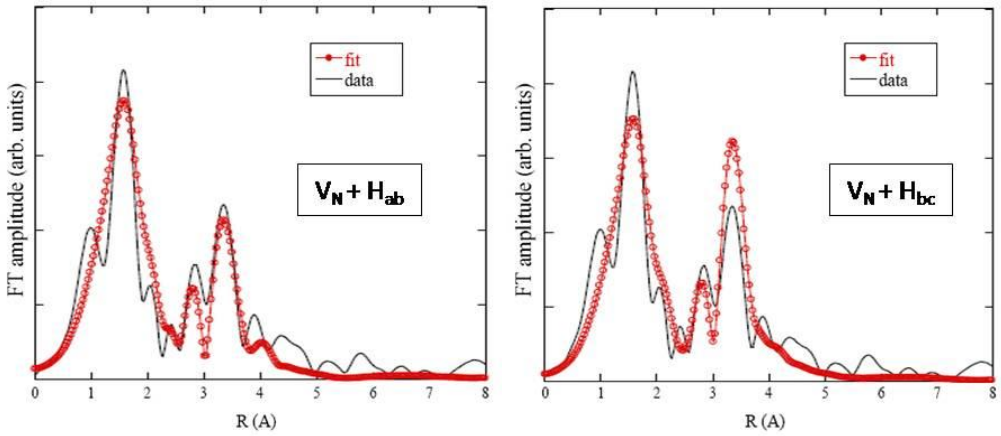

Figure 3.29. Left: FT amplitudes of H-irradiated $In_{0.82}Ga_{0.18}N$ (black line) with superimposed the fit obtained with $In_{0.8}Ga_{0.2}N$ + V_N + H_{ab} cluster. Right: the same data repeated with the fit obtained by the cluster $In_{0.8}Ga_{0.2}N$ + V_N + H_{bc}.

EXAFS data on the H-irradiated sample fitted with simulations on single-H defects and N vacancy with a single H are shown in Figure 3.28 and Figure 3.29. The fit obtained with H-complex $3H_{ab}$+H_{BC} is presented in Figure 3.30.

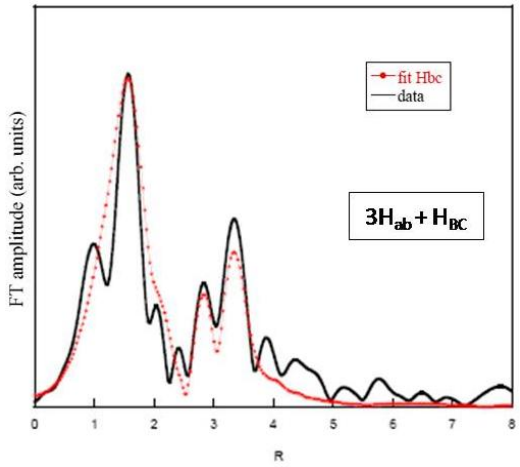

Figure 3.30. Comparison between the FT amplitude of H-irradiated $In_{0.82}Ga_{0.18}N$ (black line) and the fit obtained from the simulation on the $3H_{ab}$+H_{BC} complex (red dotted curve).

Recalling the XANES analysis results, we state that among the H-defect analysed, those relative to multi-H complexes with $3H_{ab}$ bound on the basal plane were the only ones that give a variation of the line shape comparable to that observed on experimental data. This variation wasn't in agreement with

experimental findings for $3H_{ab}$, but adding an H atom along the $\hat{c}$ axis gives much better results. To complete the analysis of that structure, we performed simulations with the other polarizations on the N atoms used in the average. A summary of XANES analysis on the $3H_{ab}$+H_{BC} complex is given in Figure 3.31, where the left graph summarizes the experimental measurements and on the right the same graph is done with the averaged simulations at the three polarizations.

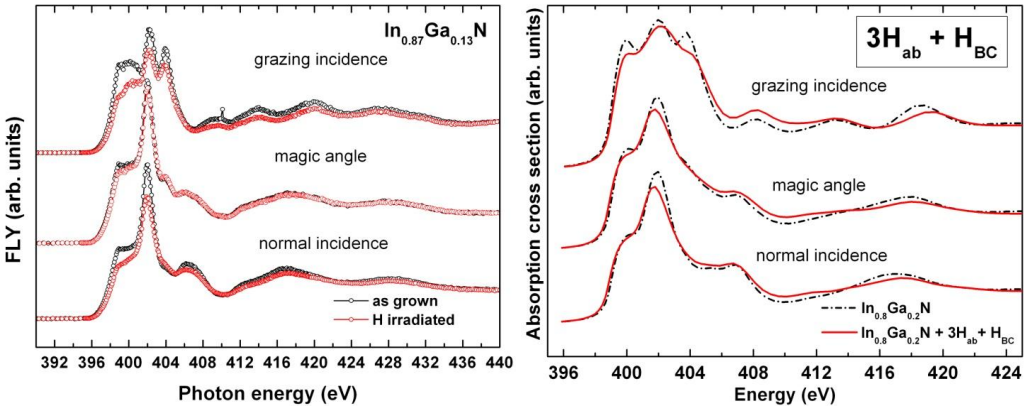

Figure 3.31. Left: summary of experimental data on $In_{0.87}Ga_{0.13}N$ as grown (black dotted curve) and after H irradiation (red dotted curve). Data acquired at all the three acquisition geometries are shown. Right: the left-graph is replicated but with average simulations instead of experimental data. Blach dashed-dotted curves are relative to the supercell without H, the red continuous lines correspond to the supercell with the $3H_{ab}$+H_{BC} complex.

The lowering of the structures at grazing incidence polarization are reproduced in the average simulation by the H-complex. Obviously the agreement is not perfect, but we recall that this result has been obtained after a detailed analysis of many plausible defects that were all discarded because variations weren't close to the experimental evidence that this multi-H complex gives the best result also for EXAFS data fitting. The results for no polarization and for normal incidence are in general good agreement with the data; the main effect of H here is a general smearing of features and a lowering of the central peak.

We can therefore conclude that from the structural analysis based on XANES N K-edge and EXAFS In K-edge on defect induced by low-energy H irradiation, we found that the multi-H complex made by 3 H atoms bound in anti-bonding configuration to 3 N with also a single H atom in bond-center configuration in the middle of the In – N bond lying on the c axis reproduces the experimental findings and is therefore the most probable H-defect present in our samples. From the point of view of energy formation, the clustering of H atoms is

highly favoured in this alloy because the strain induced by single H defects adds to the strain due to the difference in In – N, Ga – N bond distances and this local distortions can be relaxed by H-clustering.

[1] S. Nakamura, T. Mukai, M. Senoh and N. Iwasa, Jpn. J. Appl. Phys. 31, L139 (1992).

[2] C. G. Van de Walle and J. Neugebauer, *Annu. Rev. Mater. Res. 2006* ***36***, 179 (2006).

[3] M. De Luca, G. Pettinari, G. Ciatto, L. Amidani, F. Filippone, A. Polimeni, E. Fonda, F. Boscherini, A. Amore Bonapasta, D. Giubertoni, A. Knübel, V. Lebedev, M. Capizzi, *Phys. Rev. B* ***86***, 201202(R) (2012).

[4] A. Knübel, V. M. Polyakov, L. Kirste, R. Aidam, *Appl. Phys. Lett.* ***96***, 082106 (2010).

[5] L. Floreano, G. Naletto, D. Cvetko, R. Gotter, M. Malvezzi, L. Marassi, A. Morgante, A. Santaniello, A. Verdini and R. Tomasini, *Rev. Sci. Instrum.* ***70***, 3855 (1999).

[6] G. Ciatto, J.-C. Harmand, F. Glas, L. Largeau, M. Le Du, F. Boscherini, M. Malvestuto, L. Floreano, P. Glatzel and R. A. Mori, *Phys. Rev. B* ***75***, 245212 (2007).

[7] G. Ciatto, F. d'Acapito, F. Boscherini and Settimio Mobilio, *J. Synchrotron Rad.* ***11***, 278 (2004).

[8] R. Carboni, S. Giovannini, G. Antonioli and F. Boscherini, *Physica Scripta* ***T115***, 986 (2005).

[9] M. Katsikini, E. C. Paloura, T. D. Moustakas, *J. Appl. Phys.* ***83***, 1437 (1998).

[10] M. Tinkham, *Group Theory and Quantum Mechanics*, (McGraw-Hill, New York 1964).

[11] A. L. Ankudinov, B. Ravel, J. J. Rehr, S. D. Conradson, *Phys. Rev. B* ***58***, 7565 (1998).

[12] L. Amidani, F. Filippone, A. Amore Bonapaste, G. Ciatto, V. Lebedev, A. Knübel and F. Boscherini, *Phys. Rev. B* ***86***, 155211 (2012).

[13] G. Ciatto, F. Boscherini, A. A. Bonapasta, F. Filippone, A. Polimeni and M. Capizzi, *Phys. Rev. B* ***71***, 201301 (2005).

[14] M. Berti, G. Bisognin, D. De Salvador, E. Napolitani, S. Vangelista, A. Polimeni, M. Capizzi, F. Boscherini, G. Ciatto, S. Rubini, A. Martelli and A. Franciosi, *Phys. Rev. B* ***76***, 205323 (2007).

[15] P. Giannozzi et al., *J. Phys.: Condens. Matter* ***21***, 395502 (2009).

[16] R. Cowley, *Phys. Rev.* ***77***, 669 (1950).

[17] A. Amore Bonapasta and F. Filippone, *Dilute Nitride Semiconductors*, Chapter 13, Elsevier (2005).

[18] A. Janotti and C. G. Van de Walle, *Appl. Phys. Lett.* ***92***, 32104 (2008).

Chapter 4

The local electronic structure of N in dilute nitrides

4.1 Introduction

In the second chapter we described the properties of $GaAs_{1-x}N_x$ and underlined the importance of this material for the realization of a telecommunication technology integrated on GaAs. We recall that the wavelength window suitable for telecommunications is 1.3 – 1.5 μm, corresponding to 0.95 – 0.83 eV and the GaAs band gap at room temperature is 1.42 eV. Incorporation of a small amount of Nitrogen atoms has a strong impact on the electronic structure of GaAs and induces a giant bang gap lowering that brings the GaAs band gap to match the wavelength window for telecommunication applications.

This behaviour, discovered in 1992, was surprising since N is isovalent to As and the gradual substitution of As atoms with N atoms was expected to cause a continuous variation of the properties of GaAs towards those of GaN, as normally happens when two binary compounds with isovalent cations (anions) are alloyed together. Concerning the energy band gap, that would have meant its increase rather than its decrease as was experimentally found.

This puzzling behaviour raised enormous interest and researchers started to investigate the evolution of the band structure of $GaAs_{1-y}N_y$ (and of its GaAs lattice-matched counterpart $In_xGa_{1-x}As_{1-y}N_y$) with many experimental techniques and by applying different theoretical approaches to model the interaction of N with the host crystal band structure. This careful investigation led to the discovery of other interesting properties shown by this material. One that is particularly noteworthy is the response to H incorporation at all the N concentrations. It was

found that by irradiating $GaAs_{1-y}N_y$ with a low-energy H ion beam, that forces H incorporation but limits irradiation damage, complete passivation of N can be achieved, with the consequential restoring of all GaAs properties. Once a sufficient H dose has been supplied to the material, the dilute nitride is passivated but the modification induced by H is not permanent; in fact, by applying a thermal annealing at moderate temperatures, its original characteristics are restored[1].

The great effort spent investigating the dilute nitrides field led in the '90s to the understanding of the physics behind this unexpected behaviour. The mechanism at play can be described by considering two main aspects: the strong perturbation that a N atom, even if isovalent to the As it substitutes, induces on the band structure of the host crystal and the strong interplay between N atoms complexes that are naturally formed due to inhomogeneities in the material. Kent and Zunger have published a careful review[2] where they describe in detail the behaviour at different N-concentration regimes and the theoretical models that account for those observations.

Even if the picture emerging from these studies points out the prominent role of the impurity-induced perturbation on the host lattice and a main argument under debate has been the level of localization of the electronic states, the N-localized electronic structure of dilute nitrides has never been experimentally probed. Since these measurements can be useful to test the theoretical picture proposed, in this chapter we fill this lack and present a study made by x-ray absorption and emission spectroscopy at the N K-edge on dilute nitrides samples with different N concentrations that have also been treated with a H beam. The element selectivity proper of core-level x-ray techniques is exploited to investigate directly the impurity-localised electronic structure in order to have a preferential point of view to observe the action of N on GaAs and subsequently of H on GaAsN. This study provides information complementary to those given by optical techniques that are standard characterization tools in the semiconductor field. However, before presenting our results, we overview the phenomenology of dilute nitrides and the effects of H irradiation on $GaAs_{1-y}N_y$ and $In_xGa_{1-x}As_{1-y}N_y$ as studied by photoluminescence.

Dilute nitrides are so different from common semiconductor alloys with isovalent anions because of the large difference in the atomic radius and electron affinity of N with respect to As. Usually when these differences are absent, the impurity substituting an anion introduces an energetically shallow and spatially

extended state inside the CB and the perturbation felt by the host lattice is weak. As the impurity concentration is increased, the impurity-derived states start to overlap among each other and merge immediately with the band edges of the host crystal. The result is that the impurity states and the band edges move rigidly and continuously as a function of concentration and as a consequence semiconductor properties scale linearly with the relative concentrations[3]. On the contrary, substitution of an As with a N atom, which has a smaller atomic radius and a higher electron affinity, shortens the cation – anion bonds around the impurity and induces accumulation of electronic charge on N. In terms of electron levels, this means the formation of a deep, N-localized level in the vicinity of the CB minimum of GaAs that doesn't merge with the host crystal band structure but introduces a strong perturbation potential. Upon alloying, inhomogeneities arise due to the increased number of N atoms and to their random distribution in the As sublattice. Initially, these inhomogeneities were neglected and a simple theoretical model was proposed based on the interaction of only two electronic states, the GaAs CBM state and the N-localized state. That model, first proposed by Shan et al.[4] and named band anti-crossing (BAC) model, had the great merit of accounting for the most striking properties shown by this materials, first of all the giant red-shift and also the formation of new states in the CB. This model was tested on the behaviour observed in photoreflectance (PR) measurements (see Figure 2.16), where the CBM state, labelled E_-, red shifts upon increasing N concentration while a new state, labelled E_+, was detected in the CB after the incorporation of N showing a blue shift in correspondence of N incorporation. The BAC model, considering the interaction between the N-localised state and the CBM state, predicts the formation of two new levels that are split by the mutual repulsion and also that the splitting increases with concentration, with the consequential red shift of the lower and blue shift of the higher. Excellent fit to PR data were obtained by choosing the optimal value for the interaction parameter. Later on, the importance of the random distribution of N atoms was pointed out and more accurate models were attempted to take into considerations the manifold aspects of N incorporation[2]. Some of these models found that N-pairs, whose formation is a natural consequence of the increased number of N atoms and of their random arrangement, result in new localized states in the middle of the band gap, the so called cluster states (CS). These calculations demonstrate that different configurations of two N atoms in the As sublattice, for example the one corresponding to two nearest neighbours N or that with one N in

the fourth shell surrounding the other, have different localised energy levels and most of them fall inside the gap. CS are therefore not responsible for the giant band gap bowing, the origin of which has been definitively proved to be the interaction between CB states and more N-localised states, as first stated by the BAC model. Improvements on the simple BAC model were done by considering more accurately the interaction of the host crystal band structure with the impurity-derived state. This has been done mainly with the super-cell approach, that naturally considers randomness by distributing a certain number of N atoms and allows calculations of the CBM states using the empirical pseudo-potential approach. By using large super-cells (10^3-10^6 atoms), the evolution with N concentration of the band edge states, involved in optical transitions, has been studied and their energy position and their spatial localisation has been characterised[3,5,6]. What clearly comes out from these studies is that the VB is in general less influenced by N incorporation while the CB is the most affected. The general reason is that VB states are more localised on the anion sublattice and CB states on cation sublattice; since N incorporation induces strong distortions on its Ga nearest neighbours, that determines modifications on the CB more than on the VB. This was verified by Wei and Zunger[3] who studied the percentage of bowing parameter originated from volume change, charge transfer and atomic displacement and found the distortions of the Ga sublattice to be the prominent contribution. They also characterised the level of localisation of VBM and CBM states finding that the first maintains its As-character with a major contribution from longer As – Ga bonds in the vicinity of N while the second becomes strongly N-localised. Also Wang et al.[6] studied the CBM and VBM spatial localisation from a general point of view, looking at modifications induced by cation or anion substitution, in the first case when the replaced and substituting atoms have similar characteristics and in the second when they don't. They also found a strong N-localisation of the CBM state. Matilla et al.[5] focused on the alloy regime and underlined that at those concentrations N induces mixing of GaAs band states that results in a CBM state mainly of Γ and L character, without contribution from the N level like is found in the dilute regime. Even in that case analysis of the iso-surfaces of the square modulus of CBM wave function shows a strong N localisation.

Photoluminescence measurements show the formation of a single N-localized state in the ultra-dilute ($x < 0.01\%$) (observed only under external pressure) and the appearance of several cluster states inside the band gap of GaAs

in the dilute regime (x < 0.1%). In Figure 4.1 on the left CS are seen as sharp peaks between 1.40 – 1.48 eV. As the N concentration is increased, the red shift of the band gap pushes down the CBM that incorporates one by one the CS peaks, so that in the alloy regime there is only the PL peak corresponding to the main exciton transition and it red shifts with increasing N content.

However, the original properties of the band structure of GaAs can be recovered, in fact when H is incorporated into the material, N-induced effects are turned off at all the concentration regimes. This mechanism has been explored in detail with photoluminescence spectra on $GaAs_{1-x}N_x$ and $Ga_{1-y}In_yAs_{1-x}N_x$ films and QWs[1], where we recall that In incorporation serves only to obtain lattice match with GaAs but doesn't affect much the phenomenology described before.

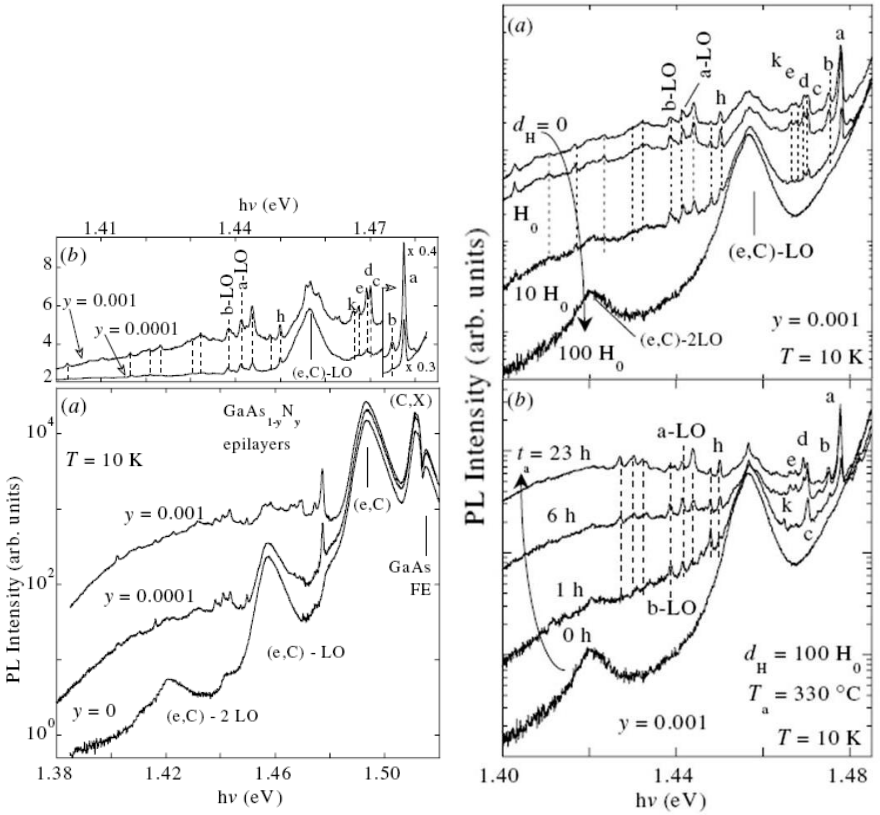

Figure 4.1. Left plot: (a) PL spectra at 10 K taken on three $GaAs_{1-y}N_y$ epilayers in the dilute limit. Peaks appearing after N incorporation corresponds to CS energy levels, while the spectrum on GaAs shows the GaAs free exciton (FE), the carbon bound exciton (C,X) and C-related free to bound transitions (e,C). (b) Magnified PL spectra on y=0.0001 and y=0.001 samples presented in (a). Right plot: (a) PL spectra at 10 K taken on the sample with y=0.001 after H irradiation with different d_H doses (H_0 is equal to $5x10^{15}$ ion/cm^2). For d_H=100 H_0 the PL spectrum of y=0 sample is restored. (b) The same sample after 100 H_0 irradiation is annealed at 330° C for several hours. PL spectra at 10 K show the recovery of the pre-irradiation spectrum and neutralization of the H-induced effects. From ref. 1.

The left-side plots of Figure 4.1 presents photoluminescence spectra on GaAs and on two dilute samples with N content equal to 0.01% and 0.1%. CS levels appear as sharp peaks at energies lower than the GaAs fundamental gap (GaAs FE stands for GaAs free exciton); the intensity of these peaks increases with increasing N concentration but remains fixed in energy, showing they are strongly N-localized (peaks whose labeled is followed by -LO represent phonon replicas). The action of H is shown on the right-side plots of Figure 4.1, that report PL spectra on a 0.1% epilayer after H irradiation with different H doses, Figure 4.1 (a), and the effect of a subsequent annealing at 330° C for several time windows, Figure 4.1 (b). H incorporation gradually lowers the CS related peaks and at $100H_0$ causes their complete disappearance, while annealing gradually restores the pre-irradiation condition until its complete recovery after 23 hours.

Samples with N concentrations in the alloy regime behave in an similar manner; under H irradiation they undergo complete passivation of N and after annealing at the right temperature they are brought back to the original condition. This behavior is independent from the presence of a small In concentration, as summarized in Figure 4.2, that shows the amount of the PL peak blue shift upon H irradiation for several H doses and several N concentrations, for both $GaAs_{1-x}N_x$ and $Ga_{1-y}In_yAs_{1-x}N_x$ films. In the alloy regime, the PL spectra are characterized by a single peak, broader than those related to CS. An example of the red shift of the PL peak upon H irradiation and the restoring of the pre-irradiation state with thermal annealing is shown in Figure 4.3 that corresponds to a QW of $Ga_{0.59}In_{0.41}As_{0.978}N_{0.022}$. All spectra are normalized and the short-dashed line is the reference of the N-free $Ga_{0.59}In_{0.41}As$ sample; the lower panel refers to the H-irradiation process and the top panel to the annealing process. The complete reversibility is clearly visible and also indicated by dashed lines with arrows that guide along the irradiation-annealing cycle.

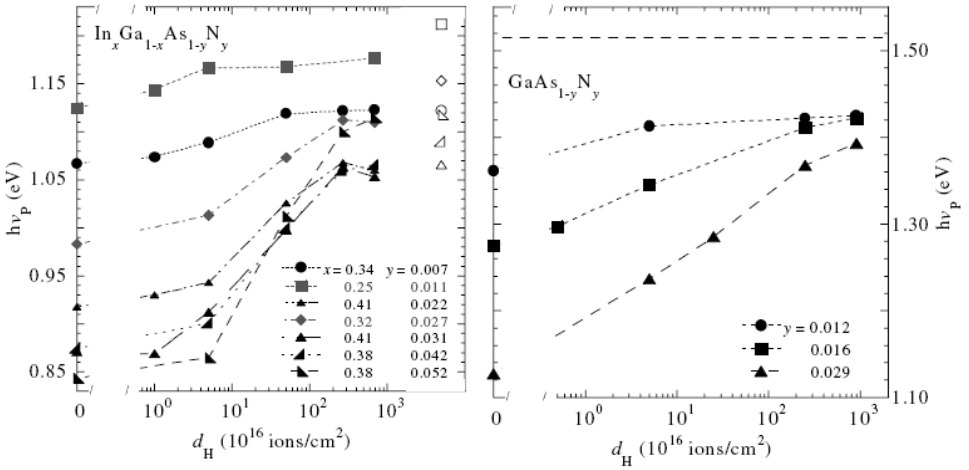

Figure 4.2. PL peak energy, $h\nu_p$, as a function of hydrogen dose for $In_xGa_{1-x}As_{1-y}N_y$ (left panel) and $GaAs_{1-y}N_y$ (right panel) QWs. The value of $h\nu_p$ of the reference N-free QW is shown by open symbols, having the same shape of the corresponding N-containing subset of samples (full symbols). The dashed line on the right panel indicates the saturation value expected for $GaAs_{1-y}N_y$ QWs. From ref. 1.

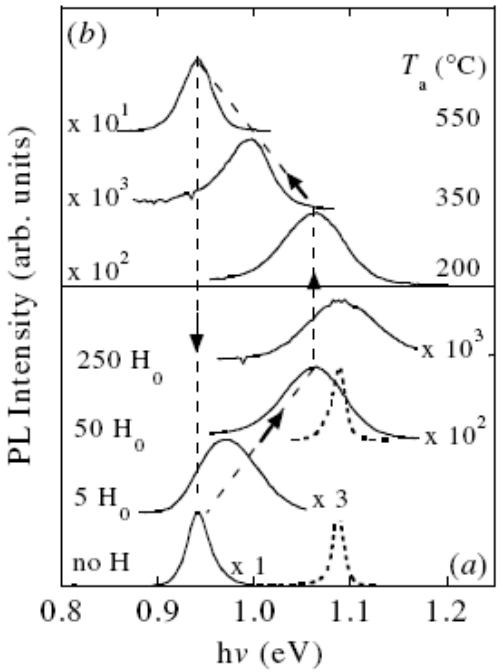

Figure 4.3. (a) Normalised PL spectra at 10 K of the $In_{0.41}Ga_{0.59}As_{0.978}N_{0.22}$ QW for increasing H dose from the bottom to the top (H_0=10^{16} ions/cm^2). Short dashed lines refer to the N-free reference sample. (b) Normalised PL spectra taken on the same sample with d_H=$50H_0$ for increasing annealing temperature (1 h duration). The cycle shows the passivation effect of H that recovers the conditions of the N-free sample and the neutralization of H effects by thermal annealing. From ref. 1.

A first hint to unravel which is exactly the role of H and how it is accomplished is given by plotting the ratio of the blue shift induced by H irradiation (B_H) and the red shift induced by the amount of N present in the sample (R_N) as a function of the ratio between the H dose supplied, d_H, and the N content y. The result is in Figure 4.4: all the samples considered fall on a common curve (dashed line) even if the N content varies by almost one order of magnitude. This is a clear indication that the same physical mechanism is responsible for the H-induced blue shift of the band gap, regardless of the N content, and that H is interacting with single N atoms, not with N clusters. In the latter case, in fact, the common curve would have been a function of d_H/y^n rather than d_H/y since the probability of having cluster states is not a linear function of the concentration, while obviously it is for the presence of single N atoms[7].

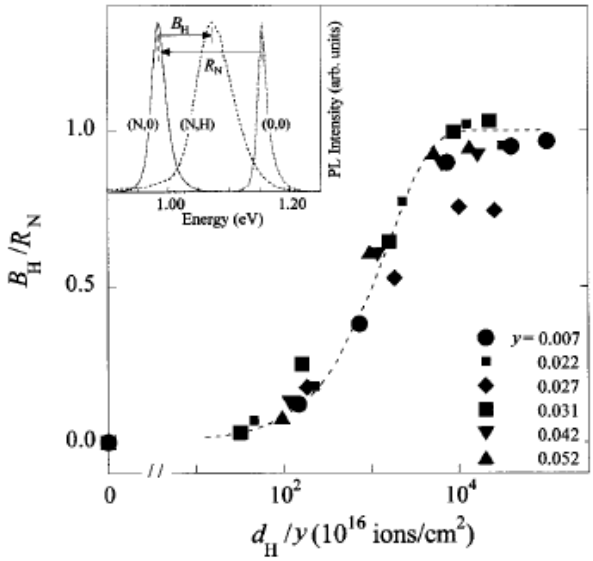

Figure 4.4. Dependence on the ratio d_H/y of the percentage of band gap recover, B_H/R_N, in $In_xGa_{1-x}As_{1-y}N_y$ QWs. The dashed line is a guide to the eye. B_H and R_N are defined in the inset of the figure for a typical QW structure (x=0.32, y=0.27, L=6.0 nm). The band gap recovery scales with y, indicating the H interact with single N atoms and not primarly with N clusters. From Ref. 7.

This has been confirmed by X-ray absorption measurements at the N K-edge on $GaAs_{1-x}N_x$ samples[8]. These measurements show that the cause of N passivation is the formation of single N – 2H atoms complexes of C_{2v} symmetry. This conclusion was the result of a careful analysis of many possible H-atom arrangements, including a 2H-atom linear complex that was previously thought to be the cause for N passivation. H-complexes were placed in a super-cell of GaAs

where a single N atom had been included and atomic positions were made relax till equilibrium was reached. These calculations were made in the framework of density functional theory (DFT) calculated in the local density approximation (LDA). Equilibrium geometries were then used as input for *ab initio* simulations of the x-ray absorption coefficient as implemented in the FEFF8.2 code. The strong modifications induced by H on the N K-edge spectra were well reproduced only by the C_{2v}-symmetry H cluster, demonstrating that this complex is the main actor in the N passivation mechanism.

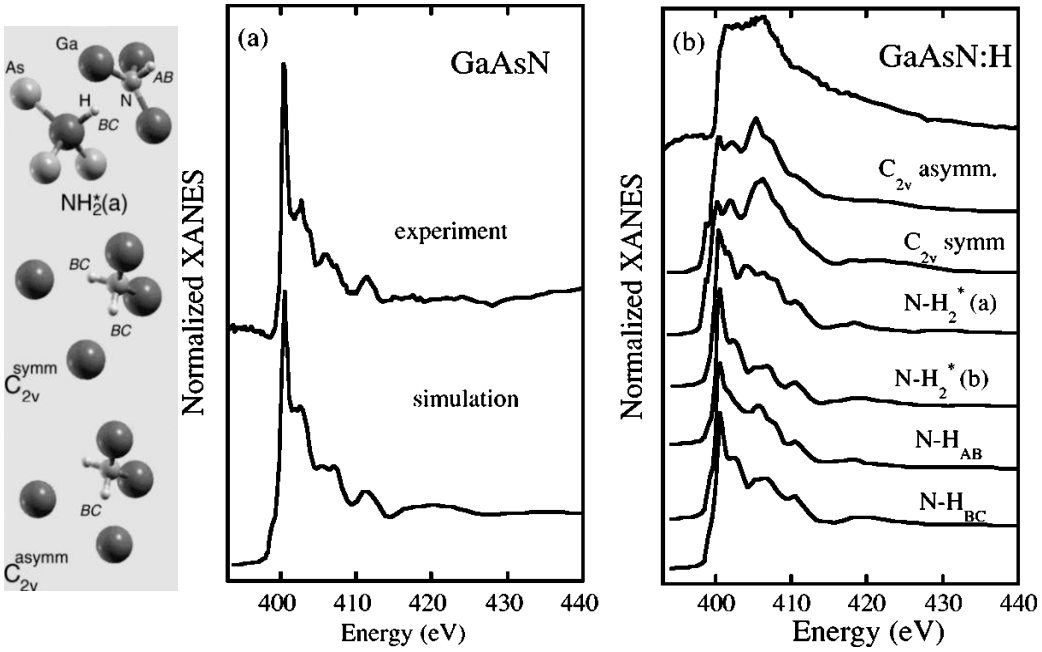

Figure 4.5. Experimental and simulated spectra on GaAsN and H-irradiated GaAsN are shown in (a) and (b) respectively. In (a) simulation of GaAsN reproduce fairly well all the spectral features of the exeperimental spectrum, demonstrating the goodness of the combined use of DFT-LDA calculation and ab initio XANES simulations. (b) presents various simulated spectra obtained by different H-atoms arrangements. The most relevant are N-H_2^*, 2H – C_{2v} symmetric and 2H – C_{2v} asymmetric that are also sketched in the image on the right. The in-line complex is N-H_2^* clearly unable to account for spectra variations, while both the 2H – C_{2v} complexes are in good agreement with the experimental data. Careful inspection reveals that 2H – C_{2v} asymmetric accounts better for experimental data. From ref. 8.

A summary is given in Figure 4.5 that reports in (a) simulated and experimental spectrum of GaAsN and in (b) the experimental spectrum of H-irradiated GaAsN compared with many simulated spectra obtained by different H atoms configurations. From (a) the soundness of the analysis method can be checked, since experiment and simulation are in fairly good agreement and all

spectral features are reproduced. Inspection of (b) clearly indicates that the in-line complex labeled $N - H_2^*$ previously believed to be responsible for H-induced effect is on the contrary unable to account for spectral variations. On the contrary, H-complexes with C_{2v} symmetry are in good agreement with experimental findings and in particular the asymmetric complex (N – H bonds displaced from the broken N – Ga bonds) has the best match with measured spectra.

As shown by this XANES study of the effects induced by H incorporation in GaAsN, when the modifications observed are correlated to a specific atomic species, like in this case where the process is due to the interaction of N atoms with H, the impurity-localised point of view is fundamental for the understanding of the physical mechanism at play. This approach can thus be used for a systematic study of the modifications caused by N on GaAs and then by H on GaAsN.

4.2 X-ray emission spectroscopy on dilute nitrides

Exploiting the element selectivity, the local sensitivity and the selection rules proper of core-level spectroscopies, we mapped the electronic structure of the VB and the CB localised on N impurities in samples of dilute nitrides. This was performed by combining XANES measurements at the N K-edge with valence-to-core XES spectra at the same edge; in this way the *p*-projected conduction and valence states localised on N impurities are probed and provide a complementary perspective to that offered by optical characterisations to look at the electronic structure modifications induced by the impurity. Before going further, it is important to note that XES and XANES involve the creation of a core-hole that can affect the electronic structure probed and as a consequence the spectral line shapes can be different from the ground state DOS. According to the final state rule, the DOS probed is that of the final state involved in the transition, therefore XANES measures the density of unoccupied states in the presence of a core-hole, while XES measures the density of occupied states in the presence of a valence hole. A valence hole has a negligible influence on the overall electronic structure, therefore XES line shape is with good approximation equal to the VB ground state DOS. On the contrary, in XANES measurements the core-hole potential can't be neglected and the CB DOS measured differs from that of the ground state.

We traced also the effect of H incorporation by measuring the same samples after they had been treated with a low-energy H beam. The results on as-grown samples can be compared with the picture outlined before and based on theoretical modelling and optical characterisation, while spectra on H-irradiated

samples can be used to confirm the results obtained by the XANES study by Ciatto et al.[8] that ruled out the H – N complex involved in N passivation. The outcome is a deeper understanding of the micro-structural physics at play in the huge band gap reduction induced by N atoms and in the H-passivation mechanism.

In the XES experiment we measured samples of dilute nitrides in the alloy regime: a GaAsN sample with 1.22% N content and an InGaAsN one with 3.43% N content and 3.70% of In content. The epilayers thicknesses were 230 nm and 150 nm respectively; both samples were grown on GaAs(001) substrates by MBE equipped with a N radio-frequency plasma source. Post-growth thermal annealing at 700° C was used to improve crystal quality and then HRXRD was performed to measure the thickness and the N content, while the In content in the quaternary epilayer was estimated with Rutherford Backscattering Spectrometry (RBS). To study the passivation effect of H, pieces of both samples were irradiated with a low-energy (100 eV) H beam provided by a Kaufman source at a H-dose around $5x10^{18}$ ions/cm^2, sufficient to obtain complete N-passivation.

On these samples and on a GaN reference, we measured valence-to-core N K-edge x-ray emission spectra, that means we excited N *1s* core-electrons to states in the continuum with monochromatised synchrotron radiation and we recorded photons emitted by valence band electrons filling the core-hole in the N *1s* state. The experiment was performed on the BACH[9] beam line at the ELETTRA synchrotron in Trieste, Italy. It has a high brilliance undulator-generated photon-beam that is a fundamental requirement to obtain good spectra on samples with N-content as low as 1.22%. Samples were measured at grazing incidence, 30° angle between the sample surface and the beam direction, to have a larger illuminated area and thus an increased signal from N atoms. Emitted photons were recorded on a CCD camera placed just after a variable line-spacing grating that disperses the impinging photons according to their energy. The CCD camera and the dispersive grating were placed on the horizontal plane at 60° angle from the beam direction, so that the experiment was performed at grazing incidence and normal emission. The line-spacing of the grating was optimized to detect photons emitted by valence band electrons filling the core-hole created by the beam, that are just below the Fermi level, around 390 eV.

The energy scale of the CCD camera was carefully calibrated around the energy region of interest in two steps: first XPS measurements of the Au $4f_{5/2}$ and $4f_{7/2}$ peaks were taken for some incident beam energies around 400 eV and the

photon beam was calibrated. Then, the x-ray beam was focused on the carbon tape used to stick samples on the sample-holder and emission spectra were taken with the beam energy set at the same values used in the previous step, so to use the elastic scattering peaks whose real energy is known to calibrate the CCD camera. The energy scale of the CCD camera was calibrated by interpolating the energy points given by the elastic peaks with a second order polynomial function.

After acquisition, data were background subtracted and smoothed with a three-point averaging. The normalisation was performed taking as a reference the Ga $L_{\beta 1}$ fluorescence line, whose third order diffracted peak was detected at 374.85 eV, and setting it to 1. Ga *2p* electrons were excited because of the presence of residual intensity from the third harmonic. We believe this normalisation criterion to be the best for a reliable comparison of spectra corresponding to samples with different N content.

4.2.1 As grown samples

Non-resonant XES spectra are proportional to the VB DOS as described in Chapter 1; XES spectra of the reference GaN and of the ternary and quaternary as-grown epilayers are plotted on the same calibrated energy scale in Figure 4.6.

The shape of the spectra of the three samples is similar and is characterised by two spectral features, the highest one at almost 393 eV and the lowest around 388 eV for GaN and 390 for dilute nitrides. The width of the emission spectrum is almost the same and is around 9 eV, while the relative height of the two spectral features in GaN is different from that in dilute nitrides. In the first case the ratio between the lower and the higher peak heights is around 28% while in both dilute nitrides it is almost 38%. Also the peaks energy of the two peaks is different going from GaN to the quaternary and ternary alloys, vertical dotted-lines of the same colour of their reference spectrum have been drawn to mark the peaks and underline the energy shifts. The common shape suggests a common atomic-orbital origin, that can be inferred from the literature on GaN XES measurements and also on projected density of states (DOS) calculations. In fact non-resonant valence-to-core XES spectra are strongly correlated to the momentum-selected partial DOS localised on the absorber. The sensitivity to the absorber environment derives from the spatial localisation of the core-hole that is the actual probe, the projection on valence states with a specified momentum (symmetry) character is because of the dipole matrix element that brings about the momentum selection rules and finally the similarity with the DOS is because of

the final state rule[10], according to which the wave functions of states involved in the transition are stationary states of the final state Hamiltonian, that in the emission process has a valence hole and a filled core-hole.

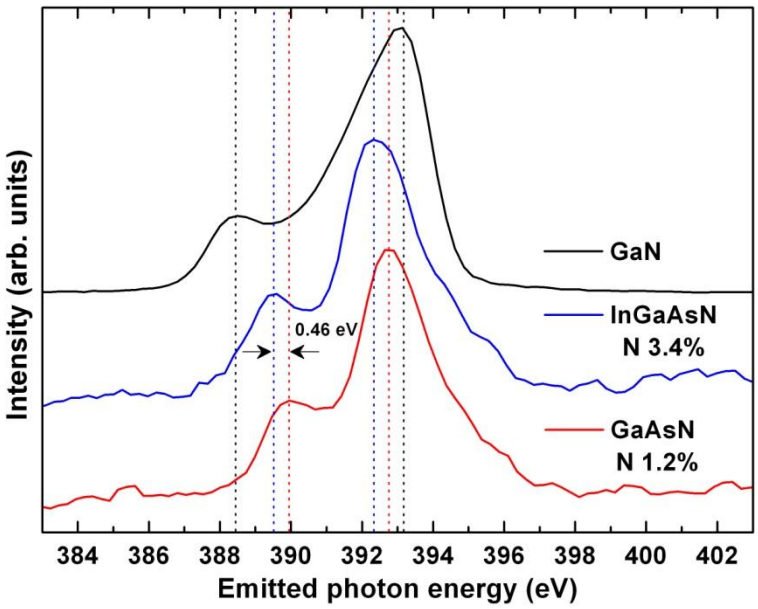

Figure 4.6. XES spectra of GaN, $In_{0.037}Ga_{0.963}As_{0.966}N_{0.034}$ and $GaAs_{0.988}N_{0.012}$. Vertical dotted-lines are placed to in correspondence of the two peaks in the spectra for each sample. The colour of the line recalls the reference spectrum. Dilute nitride spectra are distinguished only by a rigid shift that places the one with the lowest N content at slightly higher energy. On the other hand, if compared with the GaN reference spectrum, dilute nitrides show a common lineshape, but with the two structures closer in energy and the high-energy edge less steeper then it is in GaN.

This means that our N K-edge XES spectra probe the *p*-projected valence DOS localised on N atoms. In GaN both the valence and conduction band are mainly of *p*-character, because N has partially filled *2p* orbitals that participate to the bonds with surrounding Ga atoms. Calculations based on different methods find almost the same results for DOS calculations: the VB of GaN close to the Fermi energy is mainly made of N *2p* states and has the shape shown by our XES spectra. Analysis of the Ga contribution to the VB in this energy range shows some contributions from Ga *4s* states to the low energy structure and from Ga *4p* states to the higher energy one[11,12,13,14,15]. We correlate peaks in the XES spectra of dilute nitrides to the same atomic orbitals and our assignment is confirmed also by projected DOS calculated by FEFF8.4 on GaN and on GaAsN as shown in Figure 4.7: the XES simulated line shape clearly resembles the N *p*-projected DOS, but

plotting also the Ga *s*- and *p*-projected DOS it can be seen that in correspondence of the lower energy feature there is a peak in the Ga *s*-projected DOS while under the larger structure at higher energy the Ga *p*-projected DOS is significant. This energy correspondence means hybridisation of those levels.

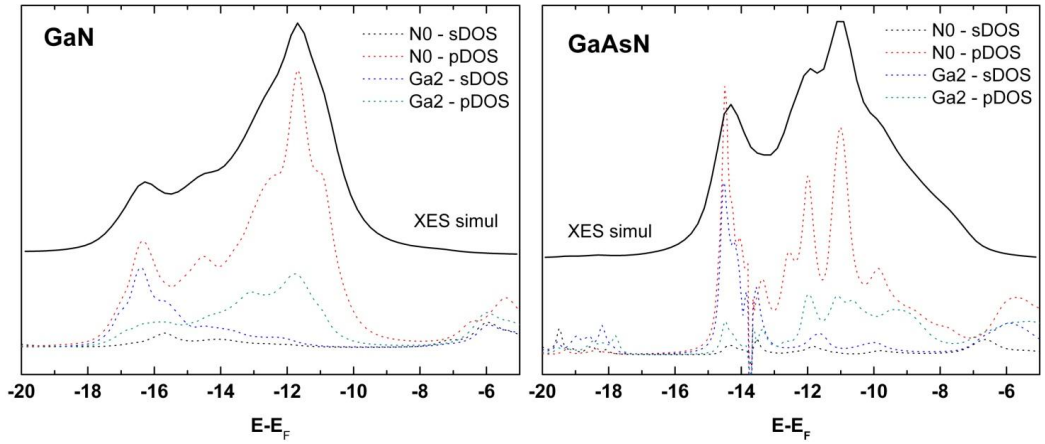

Figure 4.7. XES simulations on GaN and GaAsN with projected DOS of N s and p and Ga s and p states.

The atomic origin of XES structures is therefore the same in GaN and in dilute nitrides, but this is as far as we can go with the similarities between the spectra, in fact the comparison shows also important differences as mentioned before: the vertical lines in Figure 4.6 show that the splitting of GaN peaks is larger than that in dilute nitrides. Samples of dilute GaAsN with different N concentrations has the same splitting of XES peaks, but the energies of the peaks in the sample with more N (3%) are rigidly red shifted of 0.46 eV. The difference in the splitting of peaks is because the low-energy structure in GaN is at lower energy and at the same time the high energy side of the GaN spectra is very steep, so that the peak is just above the rising edge. On the contrary, the main feature in dilute nitrides has a much less steep increase and the peak is displaced at the center of the structure more than across the edge. Moreover we already mentioned the difference in relative peak height. More interesting is the comparison between the two dilute nitride samples, which show almost identical spectral line shapes with only a rigid energy shift that places the sample with more N at lower energy. This similarity is important as it indicates that the electronic structure characterises the single impurity and is not much affected by the formation of cluster states among N atoms, that increases with increasing N content. We

disregard the presence of In atoms in the quaternary sample because it has been proved that at such low concentration it doesn't affect the emission and absorption spectra of N and our data can be regarded as taken on samples with different N concentrations[11].

As was mentioned in the introduction, the samples were studied by XANES at the N K-edge within a study aimed at the detection of the H-complex responsible for H-induced N passivation. Measurements in that case were performed on the ALOISA beam line at the ELETTRA synchrotron, where the incident photon energy is accurately calibrated using as reference the absorption spectrum of molecular N_2, acquired in parallel to each spectral acquisition. Taking advantage of the reliability of both energy calibrations, we put XES and XANES spectra on the same energy scale and applied a rigid energy shift to refer the spectra at the valence band maximum energy (E_{VBM}). The result is shown in Figure 4.8.

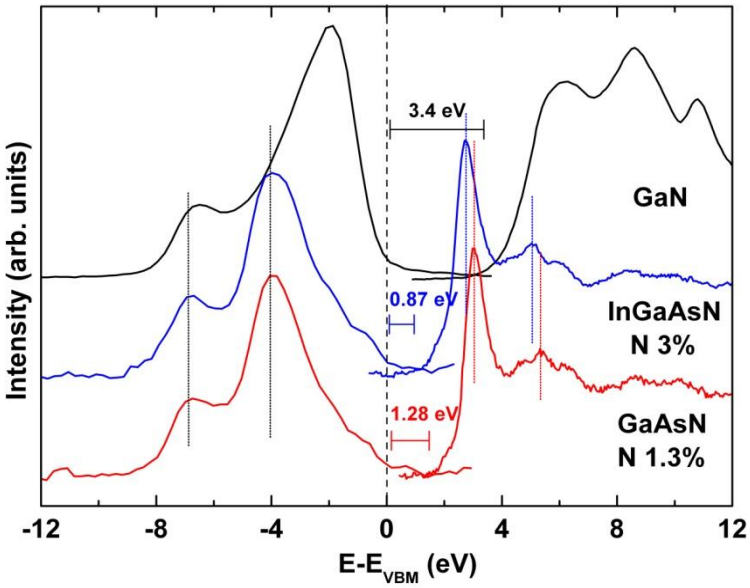

Figure 4.8. XES and XANES measurements at the N K-edge on GaN and the dilute nitrides are plotted on the same energy scale referred to the VBM. XES and XANES spectra on dilute nitrides are red-shifted of 0.46 eV and 0.71 eV respectively with increasing N concentration. This is shown by vertical lines placed on the main spectral features. A segment of 3.4 eV has been placed to suggest the comparison with the GaN energy gap obtained by optical measurements. The gap between XES and XANES is obviously related to the energy gap, but at the same time the determination of its value from x-ray measurements is not straightforward because the extrapolation of the VBM and CBM is not unambiguous.

Vertical lines are sketched to mark the main features: two for the XES peaks and two for the XANES spectrum, on the main peak close to the edge and on a

structure right after the edge. Since in XANES spectra of dilute nitrides the peaks are shifted, the colour of the vertical lines is the same as the spectrum they are referred to. The spectra of GaN has been added to the plot as a reference in the discussion of the correlation between the energy gap and the gap between the absorption and emission spectra. GaN in fact has a direct band gap of 3.4 eV, indicated by the horizontal segment, and since in this material both the VBM and the CBM have a substantial N *2p* contribution, we may think that optical transitions are between the high energy states of our XES spectrum and those at the edge of the XANES spectrum. Even if this is true, no reliable measurement of the energy gap can be extracted from our x-ray data, since the extrapolation of both VBM and CBM are highly arbitrary. In the same way the gap between XES and XANES data of dilute nitrides is strictly related to the energy gap, but any evaluation has to be made very cautiously.

With our map of the N-localised electronic structure, we can now address the question of how this N-localised point of view can be correlated with the band structure described by optical measurements and theoretical models. We start from the most striking feature of these materials, that is the large band gap reduction following N incorporation and ascribable to the downward shift off the CBM state. The CB edge has been predicted to be highly N localised at any concentration, also in the alloy regime that according to some calculations[5] is characterised by major contributions from Γ and L states. In our XANES spectra the edge is characterised by the presence of a strong resonance peak and since resonances are associated to highly localised energy levels, we attribute it to the CBM state. This assignment is in line with the red shift of the resonance peak at increasing N content. It is beyond the possibilities of these measurements to quantitatively estimate this lowering or to compare it with optical data, but we can firmly state that a red shift is present going from the 1.2% N content to the 3.4% sample. XES measurements on the other hand are not correlated to the VBM since it was predicted to be not N-localised but more As localised. Our x-ray data therefore probe states not directly involved in optical transitions.

4.2.2 H-irradiated samples

Results on H-irradiated samples shed additional light on the role of N and of course on that of H on the band structure of dilute nitrides. Figure 4.9 reports measurements performed on as grown and H-irradiated GaAsN and InGaAsN. XANES and XES spectra of irradiated samples are represented by red empty-dot

curves and are superimposed on the corresponding as grown spectrum, black empty-dot curve. The most striking effect of H irradiation is on XANES spectra, where the strong resonance characterizing the edge disappears and the edge itself is shifted to higher energy. Also the other spectral features just above the edge vanish and their place is taken by a single, smeared bump.

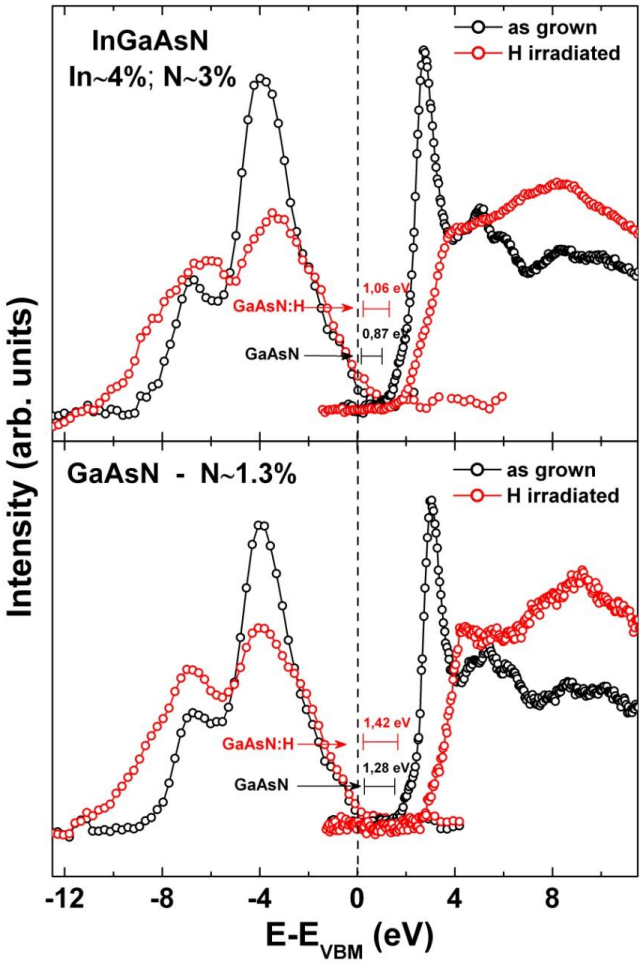

Figure 4.9. Comparison between XES and XANES spectra on as-grown (black empty-dotted curves) and H-irradiated (red empty-dotted curves) acquired on $In_{0.037}Ga_{0.963}As_{0.966}N_{0.034}$ *(upper panel) and* $GaAs_{0.988}N_{0.012}$ *(lower panel). Segments indicating the value of the band gap energy as obtained by optical characterisation before and after H-irradiation are sketched.*

On XES spectra, instead, H induces a lowering of the main peak associated with N 2p – Ga 4p orbitals and a slight increase of the lower energy peak assigned to N 2p – Ga 4s orbitals. Furthermore, the width of the emission spectrum is widened because of the appearance of new valence states on the lower-energy side

of the spectrum. These spectral variations are found in both samples and partly disclose the origin of the neutralization of N interaction with the GaAs band structure: the disappearance of the resonance peak at the XANES edge indicates clearly a loss of strong N-localisation of low energy CB states. At the same time the edge is blue-shifted and this is strictly correlated with the reopening of the gap operated by H.

On the other hand, the valence band states localised on N undergo noticeable variations: the high energy valence states loose intensity in favour of new lower energy states formed on the low-energy side of the spectrum and also of the valence states related to the lower peak whose oscillator strength is slightly increased. It can be concluded that H severely lowers the interaction of N with the CB host states leading to the reopening of the gap and also to the loss of N localisation of the CBM state. It does that by forming bonds with the N atoms as can be deduced by the remarkable variation on N valence states, but it doesn't induce any red-shift in the valence band maximum, confirming that the opening of the gap is mainly related to the CBM state shift. The bonds formed with H atoms give rise to new low energy states and strongly distort the distribution of N *p*-states in favour of lower levels.

To suggest a comparison with optical data, we draw in Figure 4.9 segments indicating the value of the band gap before (black) and after (red) H-irradiation as obtained by PL measurements on samples with analogue characteristics. The blue shift of the XANES edge is considerably larger than that observed in PL and support our statement that the CBM state involved in optical transition has lost its N-localisation after H irradiation and is therefore not seen by our x-ray data.

Even if we gave a qualitative explanation of the mechanism behind the action of H, a full explanation of our experimental findings involve the knowledge of which is the complex formed between H and N atoms. This was determined in the work by Ciatto et al.[8] based on the same XANES spectra shown here. They ruled out a H complex made by two atoms both bound to the same N in a C_{2v} symmetry. To form this complex two Ga – N bonds are broken and replaced with new H – N bonds. N is highly displaced from its previous position and relaxes towards the remaining Ga – N bonds and is followed by the two H atoms. At the end of the relaxation process, the N atom still has a tetrahedral environment, but with the N – 2H complex rotated with respect to the broken Ga – N directions, as shown in Figure 4.10.

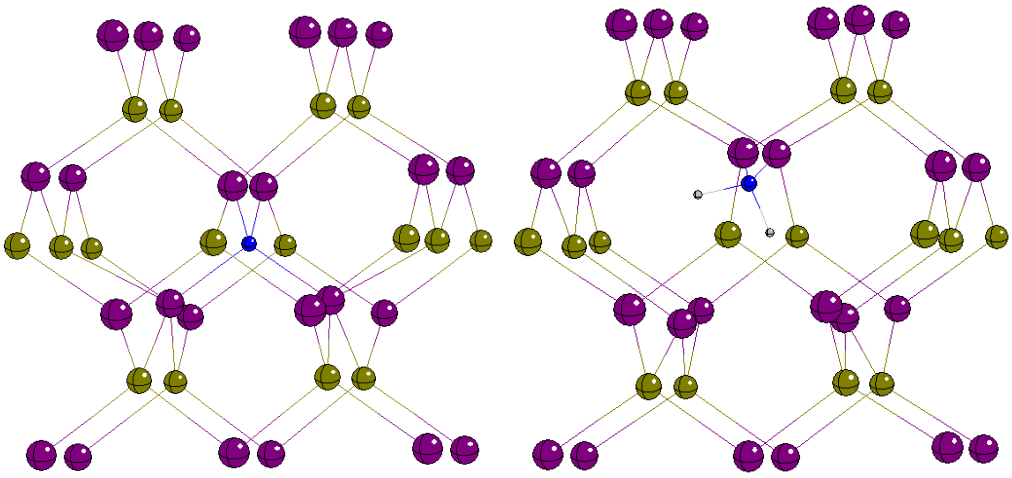

Figure 4.10. Sketches of GaAsN structure (left image) and GaAsN with the 2H – C_{2v} complex (right image) obtained by DFT calculations.

The formation of N – 2H complexes of that kind induces a strong local relaxation of the Ga sublattice from the strain introduced by N impurities and thit is probably the main cause for the reopening of the gap and the restoring of GaAs properties. In fact in the introduction we pointed out how some theoretical models predicted strong influence of cation sublattice deformation on the conduction band minimum states and on the localisation of these states on the shortest cation – anion bonds, that in this case means on Ga – N bonds. The effects induced by this complex on the XANES spectra has been discussed in depth in the paper by Ciatto et al., while the effects on x-ray emission spectra has never been addressed. We therefore performed *ab initio* XES simulations with the FEFF8.4 code on the H complex proposed by Ciatto et al. and we found that all the H-induced spectral modifications listed previously are reproduced by the simulation: the lowering of the main peak, the slight increase of the lower peak and also the widening of the overall spectrum at the low-energy side. The comparison between experimental data and simulations is shown in Figure 4.11 for the case of the ternary epilayer. The black curves identify the as-grown sample (empty-dotted line) and the simulation on GaAsN (continuous line) while red curves stands for the H-irradiated sample and simulation on the 2H – C_{2v} complex. Atomic arrangements of GaAsN and of GaAsN with the H complex were obtained by DFT calculations on a GaAs 64-atom cell with an As atom substituted by a N and with 2H atoms bound to the N in a C_{2v} symmetry. The atomic equilibrium coordinates provided by DFT calculations were used to

simulate the as-grown and the H-irradiated samples. The main parameters used for XES simulations were a SCF calculation of the atomic potentials within a radius of 7.5 Å around the absorber (86 atoms), the inclusion of FMS events within a sphere of radius 11.5 Å around the absorber (290 atoms) and the card NOHOLE to disregard the core-hole effect, since in XES the final state has a valence hole that doesn't have much influence on the electronic structure.

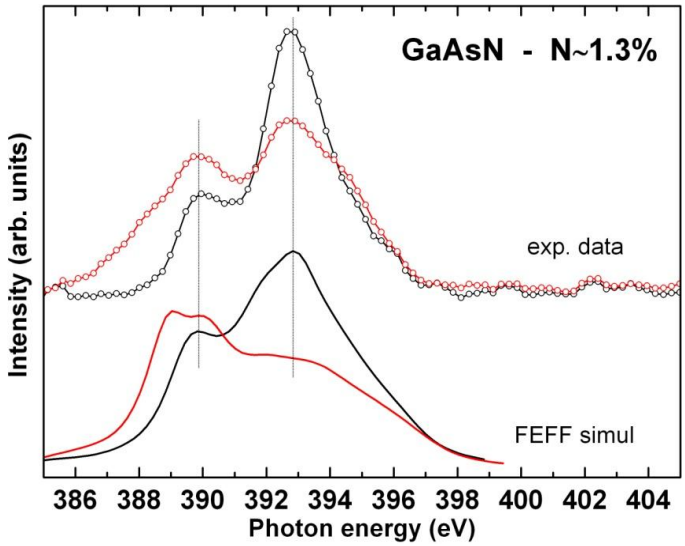

Figure 4.11. Comparison between experimental data on as-grown (black empty-dotted curve) and H-irradiated (red empty-dotted curve) GaAsN and FEFF simulations on GaAsN cluster without (black continuous line) and with the 2H – C_{2v} complex (red continuous line).

The overall effect of H is well reproduced by simulations and is in line with our spectral interpretation: the H atoms break two Ga – N bonds and strongly distort the symmetry of the structure. The Ga 4p – N 2p hybridization is lowered and at the same time the H *1s* levels hybridise with N *2p* states to form new bonds, that are at lower energy due to the strength of new H – N bonds. Contributions of *p*-symmetry by nearest neighbours are considerably lowered due to the loss of 2 Ga – N bonds, while *s*-symmetry contributions gain power and induce an increase of the low-energy side of the spectrum. The widening of the overall spectrum reflects the new weight gained by lower energy states and is confirmed by the comparison with projected DOS obtained with FEFF8.4, that shows how the low energy side is dominated by H-states. Even if the spectral modifications can be understood in the light of the N – 2H complex, the intensity of spectral features is not well reproduced by simulations. There could be many reasons behind this discrepancy, but we presently ascribe this difference to a partial N passivation in the samples

measured with XES. Agreement between data and simulations can in fact be improved by a linear combination between simulations on GaAsN and GaAsN:H that would lead to an increase of the main spectral feature. To check this hypothesis we recently measured XANES at the N K-edge on the same samples probed with XES and found that the line shape at the edge was different from that shown by fully passivated samples. A small peak, in fact, is present at the edge and the line shape is in agreement with spectra on samples at the initial stage of the annealing procedure that recovers the band structure of GaAsN.

[1] A. Polimeni, G. Baldassarri, H. von Högersthal, M. Bissiri, M. Capizzi, A. Frova, M. Fischer, M. Reinhardt and A. Forchel, *Semicond. Sci. Technol.* ***17***, 797 (2002).

[2] P. R. C. Kent and A. Zunger, *Phys. Rev. B* ***64***, 115208 (2001).

[3] S.-H. Wei and A. Zunger, *Phy. Rev. Lett.* ***76***, 664 (1999).

[4] W. Shan, W. Walukiewicz, J. W. Ager III, E. E. Haller, J. F. Geisz, D. J. Friedman, J. M. Olson and S. R. Kurtz, *Phys. Rev. Lett.* ***82***, 1221 (1999).

[5] T. Mattila, S.-H. Wei and A. Zunger, *Phys. Rev. B* ***60***, R11245 (1999).

[6] L.-W. Wang, L. Bellaiche, S.-H. Wei and A. Zunger, *Phys. Rev. Lett.* ***80***, 4725 (1998).

[7] A. Polimeni, G. Baldassarri, H. von Högersthal, M. Bissiri and M. Capizzi, *Phys. Rev. B* ***63***, 201304(R) (2001).

[8] G. Ciatto, F. Boscherini, A. Amore Bonapasta, F. Filippone, A. Polimeni and M. Capizzi, *Phys. Rev. B* ***71***, 201301(R) (2005).

[9] M. Zangrando, M. Finazzi, M. Zacchigna, D. Cocco, R. Rochow and F. Parmigiani, *Rev. Sci. Instr.* ***75***, 31 (2004).

[10] U. von Barth and G. Grossmann, *Phys. Rev. B* ***25***, 5150 (1982).

[11] V. N. Strocov, T. Schmitt, J.-E. Rubensson, P. Blaha, T. Paskova and P. O. Nilsson, *Phys. Rev. B* ***72***, 85221 (2005).

[12] W. R. L. Lambrecht, B. Segall, S. Strite, G. Martin, A. Agarwal, H. Morkoç and A. Rockett, *Phys. Rev. B* ***50***, 14155 (1994).

[13] C. B. Stagarescu, L.-C. Duda, K. E. Smith, J. H. Guo, J. Nordgren, R. Singh and T. D. Moustakas, *Phys. Rev. B* ***54***, R17335 (1996).

[14] P. Dudesek, L. Benco, C. Daul and K. Schwarz, *J. Phys.: Condens. Matter* ***10***, 7155 (1998).

[15] B. Bouhafs, F. Litimein, Z. Dridi and P. Ruterana, *Phys. Stat. Sol. B* ***236***, 61 (2003).

Chapter 5

Appearance potential spectroscopy

In chapters 3 and 4 we presented some applications of x-ray absorption and emission spectroscopies to the study of technologically advanced semiconductor materials. In particular in chapter 3 we underlined how these two techniques are complementary as they probe the unoccupied and occupied DOS of the investigated material, respectively. But despite their wonderful properties, both techniques require access to large-scale facilities, since the excitation source has to be a high brilliance and tunable x-ray beam. X-rays can be replaced by accelerated electrons that are easily produced and controlled.

In chapter 1 we introduced a core-level spectroscopy that uses accelerated electrons to probe the unoccupied DOS of materials: the soft x-ray appearance potential spectroscopy (SXAPS)[1,2,3]. SXAPS excites core-electrons with an electron beam the kinetic energy of which is close to a core level absorption edge and records the intensity of the fluorescence line as a function of the kinetic energy of incident electrons. This old technique shares with XAS some of its interesting properties: the chemical selectivity, the local sensitivity and it probes the unoccupied DOS. This technique in its standard implementation is really easy to build and doesn't require expensive instrumentation, therefore it is an excellent candidate for an in-house core-level spectroscopy apparatus. Since the recording of the first SXAPS spectra[4], a number of variants of the technique has been devised. Most experimental apparatuses developed to date have used modulation of the electron kinetic energy to improve the signal-to-noise ratio of the spectra. Recently the construction of a photon counting apparatus has been reported[5,6]; in fact, depending on their type and on the acquisition system, photon counting detectors may have energy resolution which can be exploited to improve the experimental performance. The possibility to extrapolate information about the unoccupied

DOS depends strongly on the quality of the recorded signal, but unfortunately SXAPS suffers from a low signal buried in a large bremsstrahlung background. Adding to that the still relatively sketchy interpretative framework of the SXAPS cross section, it is not surprising that lately it has been almost abandoned. However, in last decades the interpretation of XAS spectra has done big steps ahead thanks to the real space full multiple scattering theory[7]. In this approach, interpretation of data is performed on the basis of *ab initio* MS simulations of hypothetical structures, making the recording of spectra of reference compounds no longer a necessity. The interpretation of SXAPS spectra can take advantage of this approach too, but its application to SXAPS has never been discussed, nor has a comparison between XAS and SXAPS spectra been made yet.

In this chapter we present a new SXAPS apparatus that uses a windowless hyper-pure Ge diode as a photon counting detector. Such detectors have a degree of energy resolution that allows some background reduction by means of pulse height discrimination, thus improving largely the signal-to-noise ratio. We report spectra of reference compounds and interpret them on the basis of a comparison with XAS spectra and *ab initio* simulations performed in the multiple scattering approach. The good agreement shown in our results illustrates that new opportunities exist for the reference-free interpretation of SXAPS spectra.

5.1 SXAPS apparatus details

A scheme of the apparatus is reported in Figure 5.1: it is made by a commercial electron gun, the experimental chamber where the samples are hosted and a hyper pure Ge detector coupled with the electronic required for the acquisition.

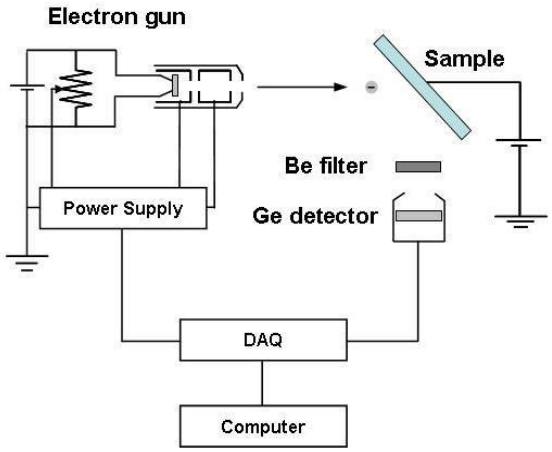

Figure 5.1. Schematic diagram of the SXAPS apparatus.

All instruments are hosted in an ultra high vacuum system maintained at a pressure around 10^{-9} mbar. The electron gun operates in the 0 – 5 KeV energy range and is equipped with the electromagnetic optics necessary for acceleration, focalization and deflection of the beam in the plane perpendicular to the direction of incidence of the electron beam. The cathode is an Yttrium high current single-welded disk designed to emit up to 1 mA, but we found that beam currents of few μA on a spot of 2 – 3 mm radius were enough for our measurements. These currents are considerably lower than those used in standard SXAPS instruments and allow longer acquisitions thanks to the reduction of beam damage. Samples are mounted on a standard sample holder with the aid of carbon tabs and silver paint to minimize charging of the surface. The manipulator on which the sample holder is mounted has four degrees of freedom and allows to move the sample in the three directions of space and to rotate it on the axis perpendicular to the plane defined by the directions of the incident beam and the detector.

The detector is a windowless hyper pure reversed biased Ge detector with an active area of almost 100 mm^2. It is mounted at 90° from the electron beam direction and the distance between the detector and the sample can be optimized thanks to a bellow and a linear slide in the range of 10 – 500 mm. Germanium

has an energy gap around 0.7 eV, thus the noise at room temperature is high and it must be operated at liquid Nitrogen temperature to reduce background currents. Because of the large bremsstrahlung radiation emitted during the interaction of electrons with the sample, a 25 μm thick Beryllium filter was placed in front of the detector to reduce the intensity of low energy radiation. The filter type and thickness can be optimized on the base of the experiment one has to perform, but during our test measurements we used only the Be filter and delayed a detailed study of filter optimization to a later test.

The electronic to elaborate the signal from the Ge diode is made by the pre-amplifier integrated on the detector, an analog pulse forming amplifier, a multi or single channel analyzer (MCA/SCA) and finally a computer that controls the whole acquisition. The signal coming from the pre-amplifier is sent to the analog pulse forming amplifier which processes the signal and gives in output a stream of Gaussian shaped peaks each one with a height proportional to the energy of the corresponding photon. The energy resolution depends on the shaping time set in the amplifier, which is the time the amplifier takes to integrate the charge released by each single photon to the detector. We set it to 0.5 μs, the lowest value, because despite the presence of the Be filter the number of photons reaching the detector was too large and a higher shaping time increases the probability of pile-up of the peaks. The train of impulses coming from the amplifier is sent to a multi channel analyzer (MCA) or to a single channel analyzer (SCA). The MCA is used in preliminary measurements to optimize the parameters to be set in the SCA, which instead is used during actual scans. The MCA separates the peaks coming from the amplifier into 1024 channels according to peaks height and gives in output the emission spectrum from the sample. Preliminary MCA spectra are acquired with the beam energy set at almost twice the value of the binding energy of the selected core-electron. This condition maximizes the intensity of emitted characteristic radiation (see Figure 1.6) that stands out from the background as a large, visible peak, of some hundreds of eV of FWHM, as is shown in Figure 5.2. From these preliminary MCA spectra, the portion of channels corresponding to the emitted characteristic fluorescence and converted into a lower and upper voltage threshold to be set in the SCA. During the acquisition the SCA neglects peaks with a height that doesn't match the selected energy-window while for each peak falling inside the chosen boundaries it gives a TTL impulse in output.

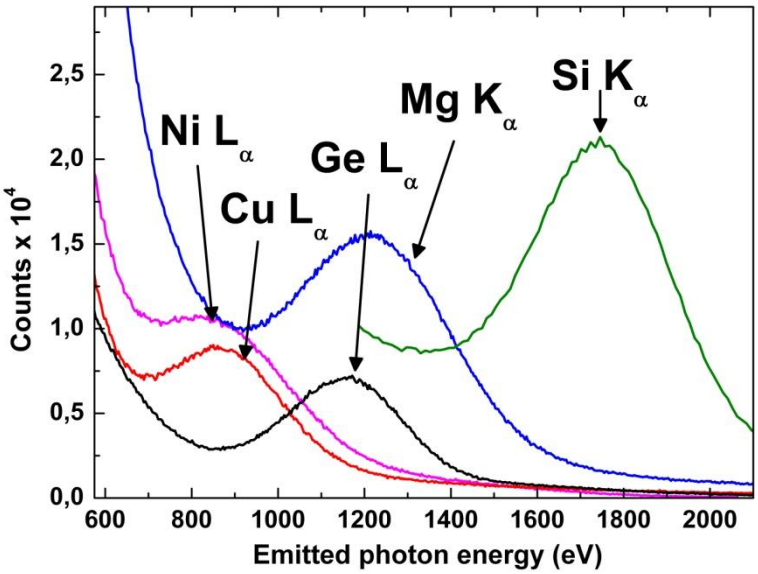

Figure 5.2. Selected MCA spectra from various elements. The kinetic energy of the impinging electron was set to almost twice the core-electron binding energy. The fluorescence peak is clearly visible on the bremsstrahlung background.

These pulses are sent to the computer that handles the whole acquisition process through a LabVIEW® code. The code was specifically developed to control the beam and record the photons emitted in the selected region of interest as a function of the electron kinetic energy.

Figure 5.2 shows some MCA spectra taken on powders of pure elements and on a Silicon wafer at an electron kinetic energy almost twice the value of the excited electron binding energy. These spectra were taken without the Be filter since it absorbs to much at these low energies. Mounting the filter inside the chamber improves considerably the signal-to-background ratio as can be seen in Figure 5.3, where selected MCA spectra taken on Si at increasing electron kinetic energies are shown. The incident beam energy starts from a value just below the ionization threshold and it is increased until twice its value. The upper panel presents spectra acquired on the Si wafer without any filter inside the chamber while spectra shown in the lower panel are taken with the Be filter placed in front of the detector. A net improvement is seen when the filter is inside the chamber: the fluorescence radiation peak is sharper and also its energy position is no more affected by the large background, thus the filter increases the energy resolution of the emission spectrum and allows a better choice of the region of channels to be integrated.

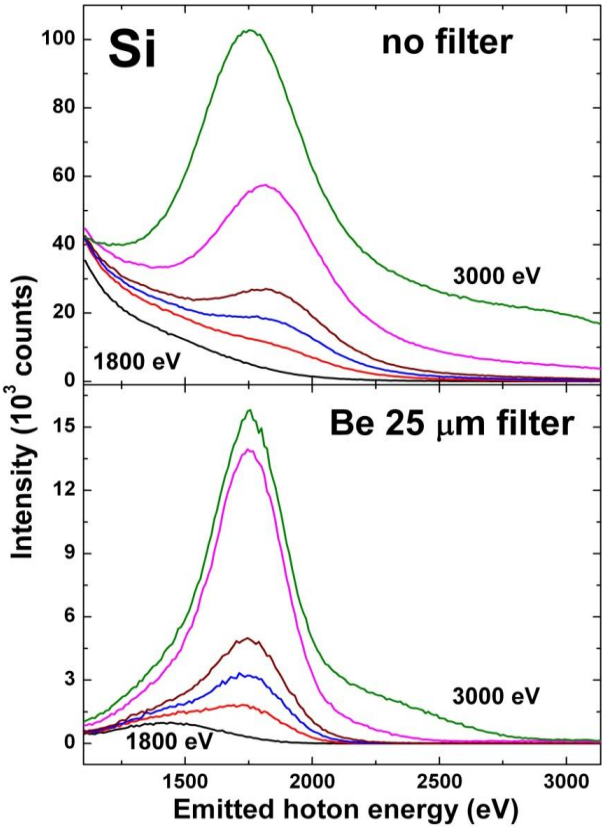

Figure 5.3. MCA spectra from a Si wafer without (upper panel) and with (bottom panel) the 25 μm Be filter inside the chamber. The spectra were recorded at the following incident energies: 1800 eV, 2000 eV, 2100 eV, 2200 eV, 2500 eV and 3000 eV; the intensity of the fluorescence peak increases with increasing incident energy and can thus be easily identified. The effect of the filter is to reduce the unwanted bremsstrahlung background with the result of a better energy resolution.

The MCA is useful to set the proper acquisition parameters but it is more practical to use the SCA to acquire SXAPS spectra as it has a faster response and once set there's no need to control it remotely while the MCA requires continuous communication with the acquisition program, increasing the acquisition time. Once all parameters are properly set and the beam has been focused on the sample, the SXAPS spectrum is acquired by scanning a range of energy around the selected absorption threshold with the incident beam and by recording the intensity of emitted photons at each energy point for a couple of minutes. It is safer to acquire spectra continuously with a small integration time per energy point and then take the average instead of counting a single energy point for a longer time. In this way effects due to sample heating, beam current drift or any other instability are equally distributed on the energy scale and a

spectrum with a satisfactory signal-to-noise ratio can be obtained by acquiring for a sufficient amount of time.

5.2 Results and discussion

We preset here preliminary results obtained with this SXAPS apparatus on a Mg polycrystalline sample and on a Si(001) wafer. In order to test the sensitivity to chemical shifts the native oxide layer on the Si wafer was not removed because we expect the resultant SXAPS spectrum to be due to both the oxide layer and the underlying Si, since the electron inelastic mean free path is similar to the native oxide layer thickness (1 – 3 nm) and at the same time lower than the escape depth of characteristic radiation photons (~10 μm). In both cases we excited electrons from the *1s* inner shell and recorded the intensity of the K_α fluorescence line.

In Chapter 1 we already gave a brief introduction to the SXAPS theory and derived the cross section. Here we recall only the final result given by the formula

$$Y_{tot}(E_0) = Y_B(E_0) + C(E)\int_{E_{core}+E_F}^{E_0-E_F} \rho(E_0-\varepsilon)\rho(E_{core}+\varepsilon)d\varepsilon$$

and the basic excitation mechanism which is sketched in Figure 5.4. Here an incident electron with E_0 kinetic energy interact with the sample and exchanges an amount of energy equal to ε with a core-electron. The result of the interaction is a final state with both electrons occupying states in the continuum, E_{f_1} and E_{f_2}. The core-hole left behind is filled by an upper core-electron, which releases the exceeding energy by emitting a characteristic fluorescence photon. For a given E_0 there are many allowed two-electrons final states, since the incident electron can lose any amount of energy starting from that required to excite the core-electron at the Fermi level, which is E_{core}+E_F, to the highest value it can release, which is E_0-E_F. The integral in the final formula is the sum on all the allowed final states. The first term in the formula accounts for the bremsstrahlung radiation and the coefficient multiplying the integral includes all the energy dependent terms, like the photon yield and the matrix element for the transition from the initial to the final state. From the formula it is clear that the line shape of the SXAPS spectrum is proportional to the self-convolution of the unoccupied DOS of the material investigated. XAS is a more direct way of probing the unoccupied DOS since the physical mechanism behind is less complex, but our preliminary measurements demonstrate that SXAPS is a good compromise to perform measurements with in-house instrumentation at a reasonable cost. We intend to demonstrate this by

comparing the recorded SXAPS spectra on the Mg polycrystalline sample and on the Si wafer with XAS spectra in the near edge region and with XAS simulations performed in the real space multiple scattering approach. Experimental XAS spectra on Mg, Si and amorphous SiO_2 were obtained with synchrotron radiation in the total electron yield mode[8] while simulations were performed with the FEFF8.4 code for Mg and with FDMNES code for crystal Silicon and SiO_2.

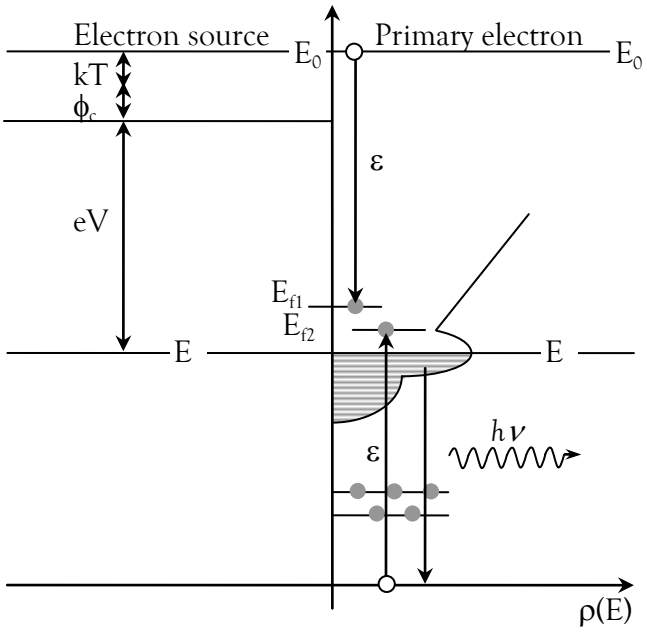

Figure 5.4. Interaction scheme of the process: incident electrons at energy E_0 are produced at the source. The incident energy is given by the applied potential plus the cathode work function plus the electron thermal energy. The primary electron looses an amount of energy ε higher than the threshold energy and excites core-electrons in an empty state E_{f2}. After the interaction the primary electron occupies an empty state E_{f1}. The core-hole left behind is filled by electrons from the occupied density of states with the emission of fluorescence photons.

The SXAPS spectra at Si and Mg K-edges are presented in the topmost plots of Figure 5.5 and in Figure 5.6: the red empty-dotted curves are the SXAPS spectra obtained with our apparatus, only a linear background has been subtracted by fitting the pre-edge region. The dotted and continuous black curves below the SXAPS spectra are the self-convoluted experimental and simulated XAS. Spectra prior to convolution are shown on the bottom plot, in Figure 5.5 for Mg and in Figure 5.6 for Si. SXAPS spectra are characterized by an almost linear, continuous increase of intensity of emitted photons at increasing electron beam energy. The kinetic energy at which the intensity starts to increase is equal to the ionization threshold. Some structures are just barely detectable in these raw spectra and

comparing the self-convoluted XAS with their original spectra it is evident how the convolution hides the wealth of information carried by the spectral line shape.

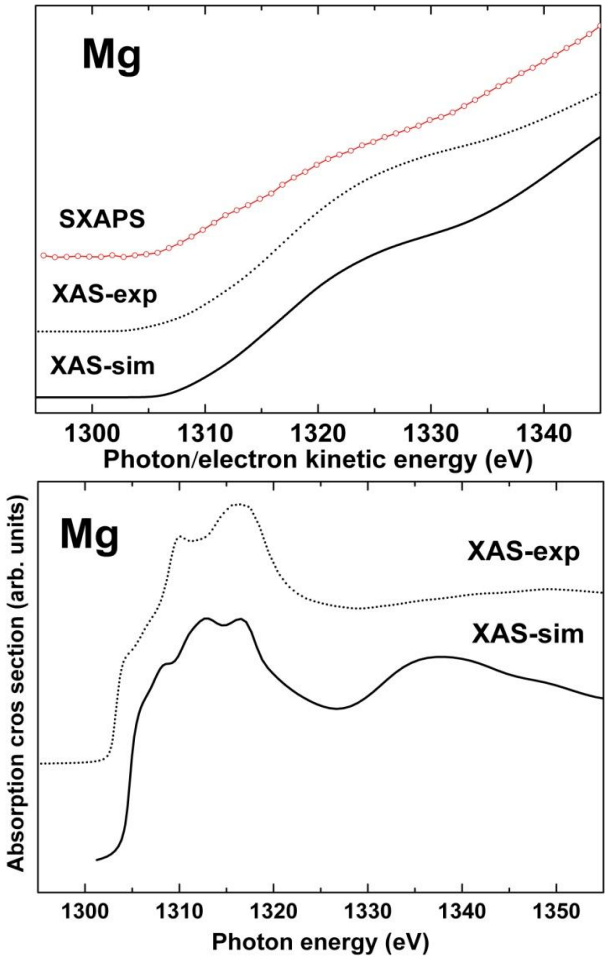

Figure 5.5. Left: Soft x-ray SXAPS spectrum from polycrystalline Mg (red dotted curve) is plotted together with the self-convolutions of the experimental XAS spectrum (black dotted line) and the simulated XAS spectrum (black continuous line). Spectra before prior to convolution are shown in the right graph. The SXAPS spectrum shows a similar trend compared to self-convoluted XAS spectra, but most of the information is lost due to smearing of features after convolution.

The presence of a double edge is however seen also in the raw SXAPS spectrum from the Si wafer. This is due, as expected, to SiO_2 and to crystal Si since a thin native oxide layer covers the wafer but the beam penetration depth is higher. Taking the experimental and simulated XAS spectra as models for the unoccupied DOS, we calculated their self-convolution with a LabVIEW® code according to the cross section formula and compared the results with our raw

SXAPS spectra by plotting the three curves on a single plot. For the Si case we superimposed the self-convolution of crystal Si (blue curves) with that of SiO_2 (black curves) properly rescaled to reproduce the relative intensities shown by experimental SXAPS.

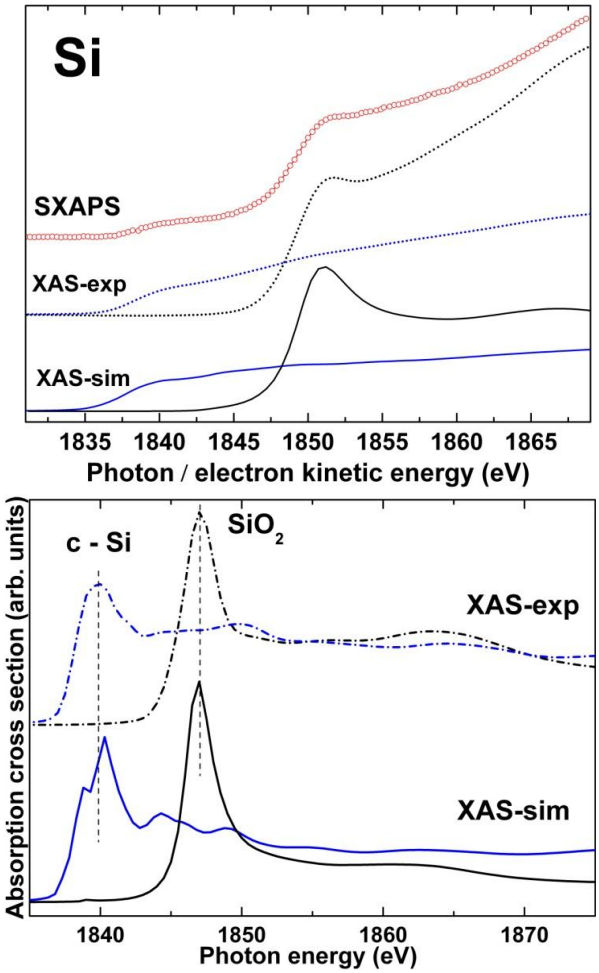

Figure 5.6. Left: soft x-ray SXAPS spectrum from the Si wafer (red dotted curve). Two edges are present in the spectrum, as was expected since the native oxide wasn't removed. For a comparison with XAS, we took experimental data from SiO_2 and crystal Si and simulated both of them. The result of simulation with FDMNES is shown in the right graph. Both experimental and simulated spectra were then self-convoluted for a comparison with the SXAPS spectrum. Self-convolution of experimental data are shown as dotted lines (blue for the c-Si and black for the SiO2), while self-convoluted simulations are plotted as continuous lines, were the colours have the same meaning.

The simulation of amorphous SiO_2 was obtained using the cristobalite structure as input for the *ab initio* code; other structures were tested but the best

match with experimental XAS on amorphous Si was found for cristobalite. Comparison of experimental XAS with simulations is shown on the right plots; the match is not perfect, but in both cases all main spectral features are reproduced by the simulation: in Mg the sudden rise of the edge, the shoulder followed by two peaks and the valley are all found in the FEFF simulation. In Si K-edge, the simulated c-Si edge is more structured then it is in experimental data, but as we will see in the following this gives no big differences in the derivative spectra. SiO_2 on the other hand is dominated by a very intense resonance standing out from an almost structureless background that is well reproduced by the simulation.

SXAPS measurements show a similar trend to that found for self-convoluted XAS spectra, but as mentioned before the fine structure shown by XAS spectra is almost totally lost while it would be desirable to restore part of it.

This is obtained by differentiating the SXAPS spectrum; in this way the small modulations present in the emitted intensity emerge from the background as shown in Figure 5.7 for Mg and in Figure 5.8 for Si. Here the differentiated SXAPS spectra are plotted in red, while derivatives of the self-convoluted XAS data are represented by black dotted lines and derivatives of XAS simulations with black continuous lines. Insets on the upper-left corners of the main graphs report the XAS data and simulations prior to self-convolution.

Differentiated SXAPS spectra are in good agreement with the derivative of XAS data and simulations. The SXAPS differentiated spectrum of metallic Mg presents two broad peaks found also in the self-convoluted XAS data and simulation. The energy position and relative intensity match those of XAS-derived spectra as underlined by vertical lines.

In the experimental SXAPS spectrum on the SiO_2/Si wafer the two features at 1837 eV and 1848.5 eV, due to Silicon absorption edge in bulk Si and in the oxide surface layer, respectively, can be clearly separated, illustrating the sensitivity of the technique to chemical shifts. As in the case of Mg, there is a good correspondence in the energy and intensity of the spectral features among the three spectra and, as can be seen, the experimental spectrum of the SiO_2/Si sample arises from a combination of the spectra of bulk Si and the oxidised layer.

We can conclude that our implementation of an SXAPS apparatus based on a windowless hyperpure Ge detector operated in photon counting mode is a useful experimental option as it allows reduction of the spectral background. Our preliminary results are in good agreement with XAS experimental spectra and the

use of multiple scattering theory as was illustrated opens new possibilities for the interpretation of SXAPS spectra and also for its application to material science.

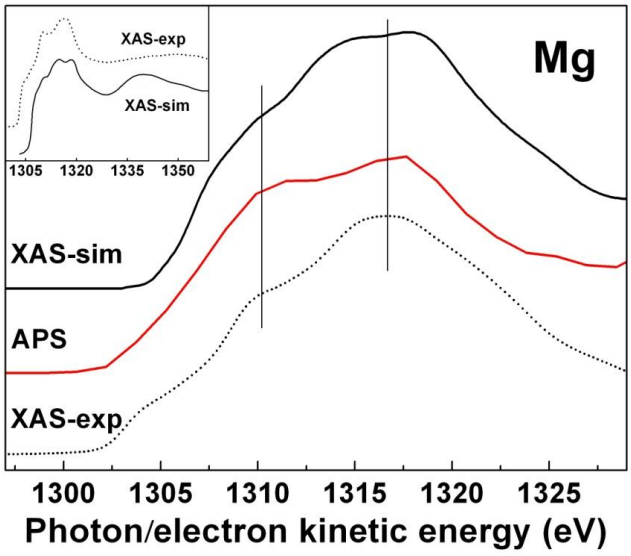

Figure 5.7. Comparison between derivatives of SXAPS spectra and self-convolutions of the experimental and simulated XAS spectra for Mg metal; the abscissa is the photon energy for XAS spectra and the electron kinetic energy for SXAPS spectra. The inset reports experimental and simulated XAS data.

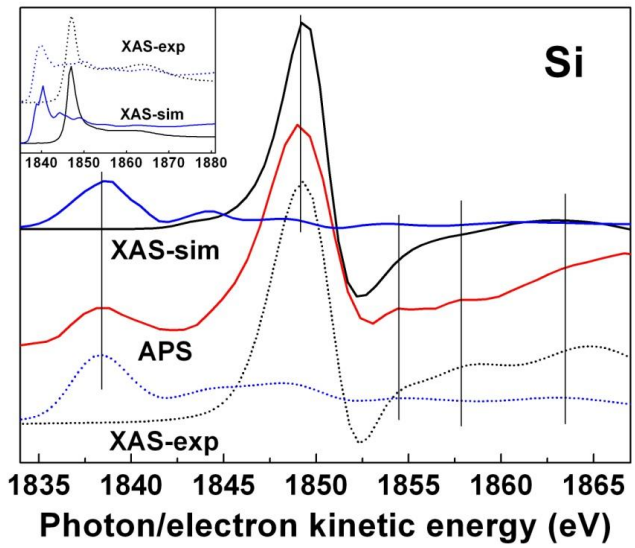

Figure 5.8. Comparison between derivatives of SXAPS spectra and self-convolutions of the experimental and simulated XAS spectra for the SiO_2/Si sample and reference samples of Si and amorphous SiO_2; the abscissa is the photon energy for XAS spectra and the electron kinetic energy for SXAPS spectra. The inset reports experimental and simulated XAS data for bulk Si and SiO_2 as described in the text.

[1] R. L. Park, J. E. Houston and D. G. Schreiner, *Rev. Sci. Intrum.* ***41***, 1810 (1970).

[2] R. L. Park and J. E. Houston, *J. Vac. Sci. Technol.* ***11***, 1 (1974).

[3] G. Ertl and Kuppers, *Low energy Electrons and Surface Chemistry* (Chemie, Weinheim, 1974), Chap. 5.

[4] G. Shinoda, T. Suzuki and S. Kato, *Phys. Rev.* ***95***, 840 (1954).

[5] Y. Fukuda, T. Kuroda and N. Sanada, *Surf. Sci* ***601***, 5320 (2007).

[6] Y. Fukuda, S. Mochizuki and N. Sanada, *J. Appl. Phys.* ***106***, 023701 (2009).

[7] J. J. Rehr and R. C. Albers, *Rev. Mod. Phys.* ***72***, 621 (2000).

[8] F. Rocca and A. M. Flank personal communication (2011). Data were recorded at the SA-32 beamline of Super-ACO storage ring with InSb(111) monochromator by measuring the drain current to ground with a picoammeter. The Mg sample was a polycrystalline powder smeared on conductive tape. The Si sample was a clean Si(001) wafer and the SiO_2 sample is the thermally grown oxide on a Si(001) wafer. Full details for the Si measurements are given in N. Daldosso *et al.*, *Phys. Rev. B* ***68***, 085327 (2003).

Conclusions

In this thesis we reported the study of two semiconductor materials, the InGaN alloy and the dilute GaAsN, in which the irradiation with H ions induces remarkable, though different, modifications of the optical and electrical properties and a novel implementation of soft x-ray appearance potential spectroscopy.

The work on a series of InGaN samples, before and after H irradiation was accomplished with XANES measurements at the K-edge of N and exploiting various polarization configurations. For the data analysis we developed an original method based on atom-specific spectral simulations performed on crystal structures obtained with DFT calculations and including polarization effects. This method led to a novel understanding of spectral feature and of their variation upon the presence of local strain in the cation sublattice. This method applied to spectra from hydrogenated samples has revealed that incorporated H atoms tend to gather and form multi-H defects, the structure of which has been identified from a coupled analysis of XANES and EXAFS measurements.

We studied dilute GaAsN with x-ray absorption and emission spectroscopies at the K-edge of N. Samples with different N concentrations have been measured before and after hydrogenation and XES and XANES spectra relative to the same sample have been coupled to form an original picture of the electronic structure localized on the N impurity. Since N atoms in GaAs and H atoms in GaAsN have a strong impact on the electronic structure of the host material, our measurements show the evolution of the electronic structure from a preferential perspective complementary to that offered by optical measurements. In addition, the analysis

of XES spectra with simulations on atomic clusters obtained with DFT calculations confirmed the geometry of the N – H defect.

Finally, we reported a novel implementation of soft x-ray appearance potential spectroscopy (SXAPS) based on a pulse-counting detector. This new set-up has been designed to have a high signal-to-noise ratio so that acquired spectra can be analyzed with a method based on *ab initio* codes. The use of SXAPS proposed in this thesis has been never presented and it enlarges the field of application of this technique, making it a valid tool in the investigation of solid state materials.

In conclusion, our work presented an original method for spectral analysis that provides a new insight into the local micro-structure of samples measured that can't be obtained with methods probing only the average properties of materials. We also exploited the chemical selectivity and local sensitivity of core-level spectroscopies to follow the effects induced by the N impurity and by H atoms on the band structure of the host material. Finally, we proposed a novel implementation of appearance potential spectroscopy that was supported by a new approach to the spectral analysis, resulting in the enlargement of the field of applications of this technique for the study of materials.

Acknowledgments

I would like to thank Prof. Federico Boscherini who introduced me into the scientific research; his advice has been precious and in these three years I learned a lot working with him.

I want also to thank Gianluca Ciatto for the collaboration, the frequent discussions and the help while I was moving my first steps in the data analysis. A special thank to Francesco Filippone, who helped me in many critical moments and has always found the time to answer my questions. I want to thank also Luca Pasquini, Aldo Amore Bonapasta, Antonio Polimeni, Marta de Luca and Mario Capizzi, Pieter Glatzel and Maddalena Pedio who hosted me as a visiting PhD student in their laboratories in Grenoble and Trieste.

Finally, I want to thank my family and all my friends that supported me in these years.